2013

Size and Rate Effects on Mechanical Behavior of Ultra High Performance Concrete

Boon Him Lim
Purdue University

Graduate School ETD Form 9
(Revised 12/07)

PURDUE UNIVERSITY
GRADUATE SCHOOL
Thesis/Dissertation Acceptance

This is to certify that the thesis/dissertation prepared

By Boon Him Lim

Entitled
Size and Rate Effects on Mechanical Behavior of Ultra High Performance Concrete

For the degree of Master of Science in Aeronautics and Astronautics

Is approved by the final examining committee:

Weinong Chen
Chair

Chin Teh Sun

Jason Weiss

To the best of my knowledge and as understood by the student in the *Research Integrity and Copyright Disclaimer (Graduate School Form 20)*, this thesis/dissertation adheres to the provisions of Purdue University's "Policy on Integrity in Research" and the use of copyrighted material.

Approved by Major Professor(s): Weinong Chen

Approved by: Weinong Chen 10/21/2013
Head of the Graduate Program Date

SIZE AND RATE EFFECTS ON MECHANICAL BEHAVIOR OF ULTRA HIGH PERFORMANCE CONCRETE

A Thesis

Submitted to the Faculty

of

Purdue University

by

Boon Him Lim

In Partial Fulfillment of the

Requirements for the Degree

of

Master of Science in Aeronautics and Astronautics

December 2013

Purdue University

West Lafayette, Indiana

ACKNOWLEDGEMENTS

I would like to thank my advisor Professor Weinong Chen for allowing me to work in the Impact Science Laboratory since I was an undergraduate student. I am really thankful for the guidance and support that Professor Chen has given me throughout these years. I would like to thank Professor Chin Teh Sun and Professor Jason Weiss for serving as my committee members. I would also like to thanks my family for being so supportive throughout my life, my best friend Zhi Jian Chong who offered me help and support, both technically and mentally whenever I needed. I would also like express gratitude to Niranjan Parab, Matthew Hudspeth, John Black, Hangjie Liao, Dr. Hwun Park, Dr. Xu Nie, Benjamin Claus, Zhu Rui Guo, Jianzhou Sun and Wataru Tsutsui for all the help and advices. Last but not least, for those who have helped me in one way or another, I greatly appreciate it. This research was supported by U.S. Army Engineer, Engineering Research and Development (Bill Heard) and U.S. Air Force Research Laboratory Munitions Directorate (Dr. Brad Martin).

TABLE OF CONTENTS

Page

LIST OF TABLES

LIST OF FIGURES

Figure Page

Figure Page

Figure Page

Figure Page

Figure Page

Figure Page

Figure Page

Figure Page

Figure Page

LIST OF SYMBOLS

t	Time
v	Velocity
C	Bar waves speed
ε_i ε_r & ε_t	Incident, reflected and transmitted strain in Kolsky Bar
σ	Stress
ε	Strain
l	Sample length
E	Young's modulus
ρ	Density
A	Area
$\dot{\varepsilon}$	Strain rate
$\ddot{\varepsilon}$	Second derivative of strain with respect to time
G_f	Gage factor
V_{in}	Input voltage

ABSTRACT

Lim, Boon Him. M.S.A.A., Purdue University, December 2013. Size and Rate Effects on Mechanical Behavior of Ultra High Performance Concrete. Major Professor: Chen Weinong.

Cor-Tuf, broadly characterize as a reactive powder concrete is a type of cementitious material. Cementitious materials have been observed to exhibit a strain-rate dependent mechanical behavior. The mechanical behavior of cementitious materials can also depend significantly on specimen sizes. Therefore it is crucial to determine the behavior of Cor-Tuf with different specimen sizes for high-rate applications. For this purpose, split Hopkinson pressure bar (SHPB), also known as Kolsky bar was utilized to determine the dynamic behavior of Cor-Tuf for different specimen sizes under uniaxial dynamic compression loading at different strain rates. It was observed that as strain rate increases the compressive strength decreases for the small specimen. However for specimens at larger diameter, the compressive strength was observed to be rate independent. The Young's modulus decreases as strain rate increases for all specimen sizes. However the critical strain and energy absorption per unit volume was observed to increase as the strain rate increases.

CHAPTER 1. INTRODUCTION

1.1 Dynamic Behavior of Materials

It is well known that the rate of deformation influences how materials behave. However, the mechanical properties of materials that can be found in engineering texts are usually characterized under quasi-static loading using standard procedures. The dynamic behavior of material can be drastically different from their behavior under static loading. Therefore, in order for us to model events such as earthquakes, explosions, structural impact etc., we need to fully understand how materials will behave under dynamic loading.

1.2 Concrete

Concrete is a material that has been widely used in civil and military applications. It is a brittle material made by cement, aggregate and water. Aggregate is the coarse particulate material such as sand or other rocks. Cement is made by calcium carbonate, also known as limestone, mixed with small portions of other materials such as clay. Cement acts as a binder as it can set and harden independently of the other materials in concrete, binding all the materials together.

Since concrete is an inhomogeneous material therefore its properties such as strength, Young's modulus, critical strain, energy absorption can differ significantly depending on the composition, manufacturing process, and specimen size.

In general, concrete can be categorized into four different types depending on the strength: normal strength concrete (NSC), high strength concrete (HSC), fiber reinforced high strength concrete (FRHSC) and high performance concrete (HPC).

1.2.1 Normal Strength Concrete

Normal strength concrete (NSC) contain cement, water, coarse aggregate, sand and usually have water to cement ratio about 0.6 [27]. The static compressive strength of NSC is usually less than 50 MPa. The reason for relatively low compressive strength is the presence of Interfacial Transition Zone (ITZ) [27] which is the weakest zone in the concrete and will be discussed in detail in section 2.2.1.1.

1.2.2 High Strength Concrete

In order to increase the compressive strength of NSC, HSC were introduced and are widely used. Similar to NSC, HSC is composed of cement, water, coarse aggregate and sand with lower water to cement ratio of about 0.3 [27]. In HSC, the ITZ is no longer the weakest zone, but coarse aggregate may be the weakest link [27] which leads to higher static compressive strength. The static compressive strength for HSC was observed to be about 80-90 MPa [27].

1.2.3 Fiber Reinforced High Strength Concrete

One major problem with HSC is the reduction in ductility with increasing strength. Therefore, to enhance the ductility of HSC, FRHSC had been introduced and are widely used in airport runways and protective buildings [20]. FRHSC is manufactured by adding 1-3% fibers by volume into HSC [14, 27]. The most common fibers used in FRHSC are either steel or polyethylene fiber. One major advantage of FRHSC is that it has higher energy absorption characteristics compared to HSC.

1.2.4 High Performance Concrete

In order to achieve compressive strength of more than 150 MPa, high performance concrete (HPC) was introduced. Two of the most common HPC are ultra-high-strength-concrete and reactive powder concrete (RPC). RPC was developed by Bouygues's laboratory and patented in France in 1990s [18]. For RPC, the higher compressive strength can be achieved by only using fine aggregate (no course aggregate) and lowering the water to cement ratio by using a superplasticizer. The reactive powder concrete used in this study is known as Cor-Tuf. The static compressive strength of Cor-Tuf was observed to be around 190 MPa-240 MPa [9]. The process of manufacturing Cor-Tuf will be discussed later in detail in section 3.1.

1.3 Problem Statement

This study is mainly focused on the dynamic behavior of RPC with different sizes. Cor-Tuf was fabricated in Geotechnical Structures Laboratory (GSL) in the Army Research and

Development Center (EDRC), Vicksburg, MS. The experiments to assess the static strength were performed by EDRC [9].

The purpose of this study is to find out how differently sized Cor-Tuf specimens behave under uniaxial dynamic compressive loading. Strain rates of 50/s to 200/s were investigated for generating the stress-strain response along with other mechanical properties of two differently sized Cor-Tuf specimens. Two different sizes of Kolsky Bars were utilized in this study to achieve different strain rates for differently sized specimens and will be discussed in subsequent sections.

CHAPTER 2. LITERATURE REVIEW

2.1 Kolsky Bar Background

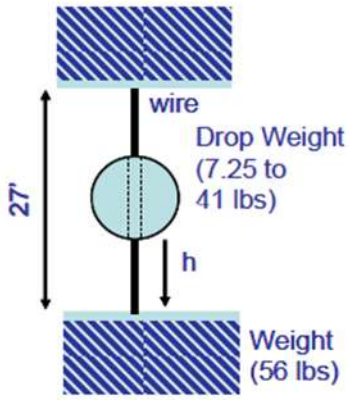

Figure 2-1 Apparatus of Herbert Kolsky Experiment (Figure was reproduced from Chen et al. [3])

Split Hopkinson pressure bar (SHPB) also known as Kolsky bar is widely used as a mechanism to apply controlled dynamic loading. The development of Kolsky bar used the principle of wave propagation in a bar initially discovered by John Hopkinson in 1872 [3]. John Hopkinson was conducting a rupture test on an iron wire using a drop weight impact. The apparatus of his experiment is shown in Figure 2-1. It was observed that the wire breaks at both ends, but the break point was observed to be independent of the mass of the drop weight. This experiment showed that the stress wave propagates along the iron wire. However, quantitative measurement of the stress waves was not possible in this experiment.

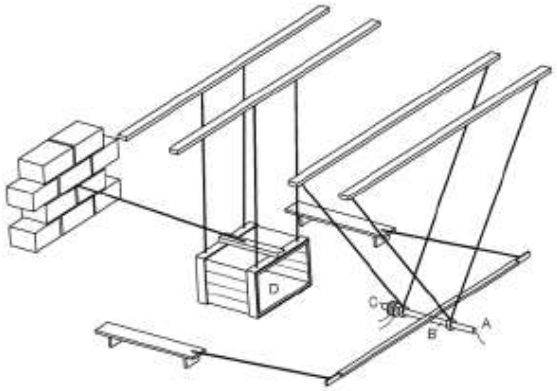

Figure 2-2 Apparatus of Bertam Hopkinson (Figure reproduced by Chen et al.[3])

To overcome this problem John Hopkinson's son, Bertam Hopkinson [3, 12], invented a pressure bar system to measure the pressure produced by explosive or high speed bullets. Figure 2-2 shows the apparatus used by Bertam Hopkinson. In the experiment, bars B and C were connected using a magnet. When bar B was impacted by a projectile from a detonated gun, caused bar C to launch which was captured by D. However, if the length of C was shorter than half of the loading duration, both bar B and bar C were launched. So by using appropriate length of C such that only C was launched, the magnetic attractive force between bar B and C could be calculated. Hence, Bertam Hopkinson was able to get a pressure-time curve for a given geometric configuration of bars B and C.

In 1948, Davis [3, 5] improved the pressure bar technique by using a parallel plate and cylindrical condenser microphones to measure the axial and radial movement of the bars. This measuring technique was more accurate than the technique used by Bertam Hopkinson.

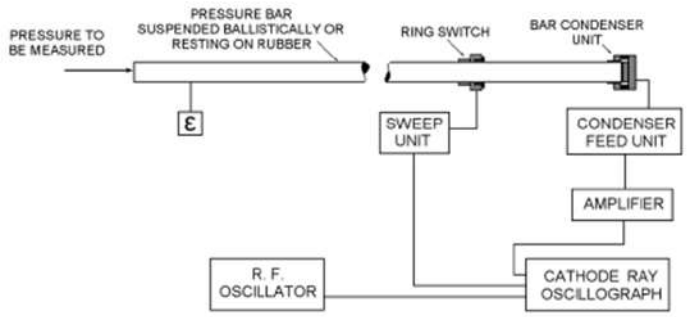

Figure 2-3 Davis Bar (Figure reproduced by Chen et al.[3, 5])

In 1949, Kolsky [16] used two bars with a specimen sandwiched in between for assessing the dynamic properties of the materials. By using this technique Kolsky not only improved the previous technique but also derived a set of equations to convert the raw data to obtain dynamic stress strain curves. Since most of the materials behave differently under dynamic loading conditions, a set of stress-strain curves at different strain rates are desired to develop rate-dependent material models. Kolsky Bars are ideal for obtaining these curves.

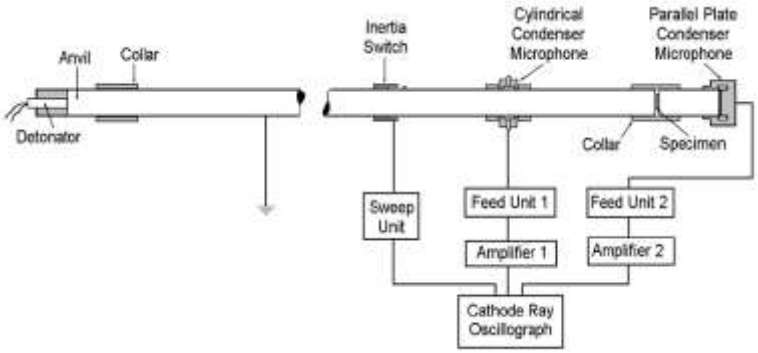

Figure 2-4 Original Kolsky Bar (Figure reproduced by Chen et al.[3, 16])

2.2 1-D Stress Waves Analysis

In typical Kolsky Bars, the striker, incident and transmission bars are fabricated using the same material and have the same cross sectional area, when the striker impact the incident bar, the particle velocities in the bars need to be compatible and the forces need to be in equilibrium i.e.:

$$V_{st} + V_R = V_I \qquad \text{Equation 2.1}$$

$$\sigma_{st} + \sigma_R = \sigma_I \qquad \text{Equation 2.2}$$

The stress and velocity are related by

$$\sigma = \pm \rho C V \qquad \text{Equation 2.3}$$

Since initially there is no stress in the striker (i.e. $\sigma_{st} = 0$), hence by solving equations 2.1 and 2.2 we get the magnitude of incident and the reflected waves as

$$\sigma_I = \frac{1}{2}\,\rho C V_{st} \qquad \text{Equation 2.4}$$

$$\sigma_R = \frac{1}{2}\,\rho C V_{st} \qquad \text{Equation 2.5}$$

Using the stress-strain relationship, the incident pulse can be represented as strain by

$$\varepsilon_I = \frac{1}{2}\,\frac{V_{st}}{C} \qquad \text{Equation 2.6}$$

The above equation is usually used as the calibration for the Kolsky bars. The reflected wave propagates through the striker and reflected at the end as tensile waves thus unloading the bar. Hence the incident wave has loading duration

$$T = \frac{2L_{st}}{C_{st}} \qquad \text{Equation 2.7}$$

The incident pulse then propagates through the incident bar into the specimen and finally to the transmission bar, as shown in Figure 2-5.

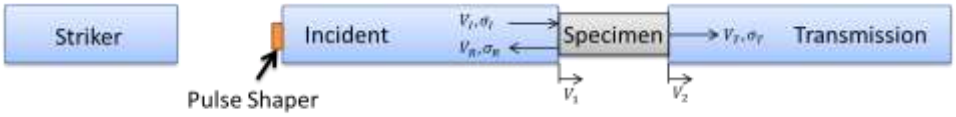

Figure 2-5 Split Hopkinson pressure (Kolsky) bar

The strain rate of the sample can be defined as

$$\dot{\varepsilon} = \frac{V_1 - V_2}{L} \qquad \text{Equation 2.8}$$

The incident bar velocity and transmission bar velocity are related to the incident, reflected and transmission waves as

$$V_1 = \frac{(\varepsilon_I - \varepsilon_R)}{C} \qquad \text{Equation 2.9}$$

$$V_2 = \frac{\varepsilon_T}{C} \qquad \text{Equation 2.10}$$

Hence the strain rate can be written as

$$\dot{\varepsilon} = \frac{1}{CL}(\varepsilon_I - \varepsilon_R - \varepsilon_I) \qquad \text{Equation 2.11}$$

By integrating the strain rate, the strain is obtained,

$$\varepsilon = \int \dot{\varepsilon}\ dt \qquad \text{Equation 2.12}$$

Since we know the stress acting on both ends of the specimen, the stress can be calculated by taking the average of the stresses on both ends

$$\sigma = \frac{A_b}{2A_s} E(\varepsilon_I + \varepsilon_R + \varepsilon_T) \qquad \text{Equation 2.13}$$

If the specimen is in stress equilibrium, i.e.:

$$\varepsilon_I + \varepsilon_R = \varepsilon_T$$ Equation 2.14

Then the strain rate and stress can be rewritten as:

$$\dot{\varepsilon} = \frac{-2}{CL}\varepsilon_R$$ Equation 2.15

$$\sigma = \frac{A_b}{A_s}E\varepsilon_T$$ Equation 2.16

In conclusion, if a specimen is under dynamic stress equilibrium, the following three equations can be used to obtain the strain-rate, stress and strain of a specimen using Kolsky Bars

$$\dot{\varepsilon} = \frac{-2}{CL}\varepsilon_R$$ Equation 2.17

$$\varepsilon = \int \dot{\varepsilon}\ dt$$ Equation 2.18

$$\sigma = \frac{A_b}{A_s}E\varepsilon_T$$ Equation 2.19

2.3 Concrete

Concrete is a brittle material composed of cement, aggregate and water. Concrete has been widely used in civil and military application because of its cost effectiveness. Moreover, weight is not a primary concern in civil engineering application where concrete is used. However, use of concrete in civil and military applications requires it to resist different kinds of loading which include gravitation loading, explosions, and earthquakes which span a wide range of strain rates. Therefore it is very important to understand how concrete will behave at different strain rates.

Reactive powder concrete (RPC) was developed in 1994 at Bouygues's laboratory in France by Richard et al. [18]. The main composition of RPC is Portland cement, silica fume, sand, and superplasticizer. RPC does not contain any course aggregate. The sand particles have a diameter of 150-600 μm. The strength of RPC is futher enhanced by lowering the water to cement ratio by utilizing superplasticizer. Two RPC were produced by Richard et al.: RPC200 and RPC800. Under quasi-static loading the RPC200 has compressive strength of 170-230 MPa, flexure strength of 30-60 MPa, Young's modulus of 50-60 GPa, and fracture energy of 20-40 kJ/m^2. In contrast, RPC800 has static compressive strength of 490-680 MPa when using quartz sand, 650-810 MPa when using steel aggregate, flexure strength of 45-141 MPa, Young's modulus of 65-75 GPa, and fracture energy of 1.2-20 kJ/m2 [18]. Many researchers have explored the quasi static behavior of reactive powder concrete, however only few studies and investigate the dynamic behavior of RPC.

2.4 Dynamic Behavior of Concrete

Most researchers agree that concrete is a rate dependent material [1, 2, 7, 13-15, 17, 19, 21, 25-30, 32, 34] which means that the mechanical properties such as strength, critical strain, Young's modulus, etc. depends on the loading rate. A comprehensive review of studies on compressive behavior of concrete is presented by Bischoff et al. in reference [2]

2.4.1 Dynamic Compressive Strength

Since concrete used by different researchers had different properties such as static compressive strength, Young's modulus, etc. therefore a feasible way to compare the data is to normalize the dynamic properties to its static properties (defined as the dynamic increase factors) and plot them against the strain rate. It is generally acceptable that under dynamic loading the compressive strength increases as compared to the quasi-static compressive strength [1, 2, 14, 17, 25, 27, 28].

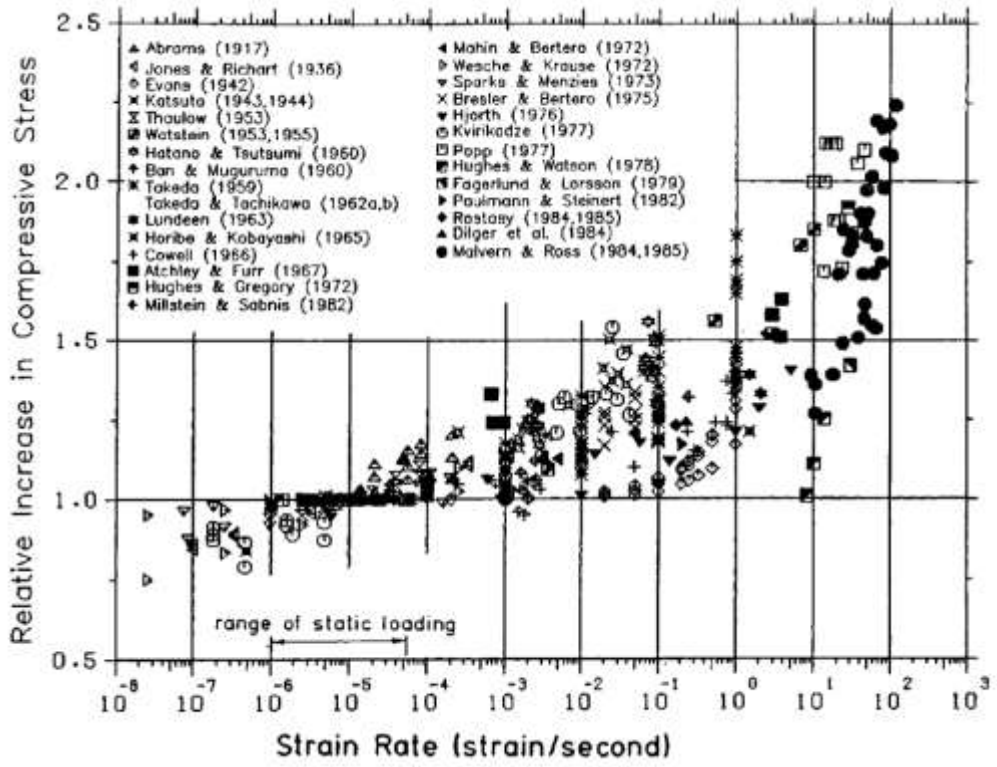

Figure 2-6 Relative Increase in Compressive Stress vs Strain Rate, figure reproduced from Bischoff et al. [2]

Figure 2-6 shows the Dynamic Increase Factor (DIF) vs strain rate for the concrete summarized by Bischoff et al. [1]. DIF is defined as the dynamic compressive strength

normalized by its static compressive strength. Several reasons for the increase in compressive strength are proposed including concrete quality, aggregate, curing and moisture conditions, age and radial inertia confinement. Effect of these factors are elaborated in following subsections.

2.4.1.1 Concrete Quality

The most important factor for the increase in Dynamic Increase Factor (DIF) with increasing strain rate is the concrete quality. Most researchers observed that the DIF decreases from NSC to HSC and FRHSC [2]. The primary reason for the higher DIF in NSC is the presence of Interfacial transition zone (ITZ) which is the weakest zone in concrete and the energy required to open cracks in this zone is lesser compared to other parts. Hence the static compressive strength decreases for NSC [27]. However on dynamic loading, the fast propagation of load forces cracks to propagate through the aggregate thus increasing the dynamic compressive strength which in turn increases the DIF.

For HSC, the ITZ is no longer observed to be the weakest zone. It was observed that during static loading, the cracks propagate through the aggregate. However, at high rate loading, HSC was observed to break into many pieces [27]. This suggests that many cracks propagate through the concrete simultaneously and the input energy was mostly dissipated in opening new cracks since the energy required to open new cracks is much more compared to propagating an already developed crack [2].

For FRHSC, under static loading, most cracks propagated through the aggregate. Since the static strength does not increase significantly compared to HSC, it was

concluded that adding fiber less than 3% in volume does not contribute to the increase in static strength. However, under dynamic loading conditions, FRHSC was observed to fracture into even small segments than HSC but maintained its integrity due to presence of the fiber [27].

Wang et al. [29] studied the influence of steel fiber on the compressive behavior of RPC under dynamic compression loading and observed that RPC with different fiber volumes was rate dependent and the compressive strength of RPC increased as strain rate was increased. However, from the analysis of the data presented, it can be observed that the specimen did not fail under first pulse of the compressive loading as the reflected pulse shows a plateau region which is the characteristic of the specimen which has not failed completely. Yang et al. [15] also studied the mechanical properties of RPC at high rate. One unique feature about their method was that they impact the RPC in such a way that it would not fracture into many pieces to enable them to get the energy absorption value. However, the drawback of this method was that since the sample did not fail completely the compressive strength could not be obtained. Yi [33] studied the blast resistant of RPC and observed that under blast loading, the blast resistant of RPC was much greater than NSC.

Some of the research on RPC is focused on replacing the expensive material in the RPC by a cheaper material. For instance, Pan et al. [13] used slag as a replacement for silica fume. They observed that by replacing silica fume with slag, the compressive strength decreases as the amount of slag increases. Compressive strength was observed to increase as the amount of steel fibers increased. They also observed an increase in

compressive strength with increasing strain rate. Zhang et al. [34] replaced portion of silica fume by ultra-fine slag and ultra-fine fly ash. The RPC thus obtained displayed superior static compressive strength (more than 200 MPa)

2.4.1.2 Lateral Inertia Confinement

As shown in Figure 2-1, the DSIF increases significantly when the strain rate increases above 30/s. It is arguable that the increase in DSIF is not because of the material effects but the "structural" effects. As strain rate increases, time available for micro-crack development and propagation is reduced, which leads to increment in the strength of concrete. In addition, it is also suggested that increase in strength may be a result of transition from uniaxial stress to uniaxial strain condition [2]. When a cylindrical specimen was loaded rapidly in the axial direction, it would not be able to expand in the lateral direction instantaneously due to the inertia restraint, causing the loading condition towards uniaxial strain condition in which the corresponding lateral stresses act as confinement. This transition violated the assumption of SHPB which states that the specimen must be under uniaxial stress condition. Furthermore, this transition may also cause increment in critical compressive strain and lead to increase in number of cracks.

2.4.1.3 Aggregate

The types of aggregates used in concrete also have influence on its dynamic behavior. As mentioned earlier, most cracks propagate through aggregate under dynamic loading. Aggregates that exhibits a good bonding characteristics minimize the difference in

stiffness with the surrounding mortar matrix leading to a better impact resistant [2]. In addition, it is also observed that a smaller size of aggregate has higher compressive strength [2].

2.4.1.4 Curing and Moisture Condition

It was observed by Ross that wet concrete tends to have higher DIF compared to dry concrete [19]. A dry specimen has relatively higher static strength compared to the same specimens tested statically under wet condition. However, at high rates, specimens in both conditions show similar compressive strengths. It can be concluded that moisture does not have a significant effect on the dynamic strength of concrete for compressive loading.

2.4.1.5 Age

The effect of age on the relative strength increase has been studied, but results are obscured by the interdependence of curing conditions. It was observed that when the age of concrete increased, the static strength increased as well. It was also observed that the DIF decreased as age increased [2]. Comparative analyses of the literature shows that age of the concrete had minimal effect on the dynamic mechanical properties of the concrete if moisture conditions were similar.

2.4.2 Critical Compressive Strain

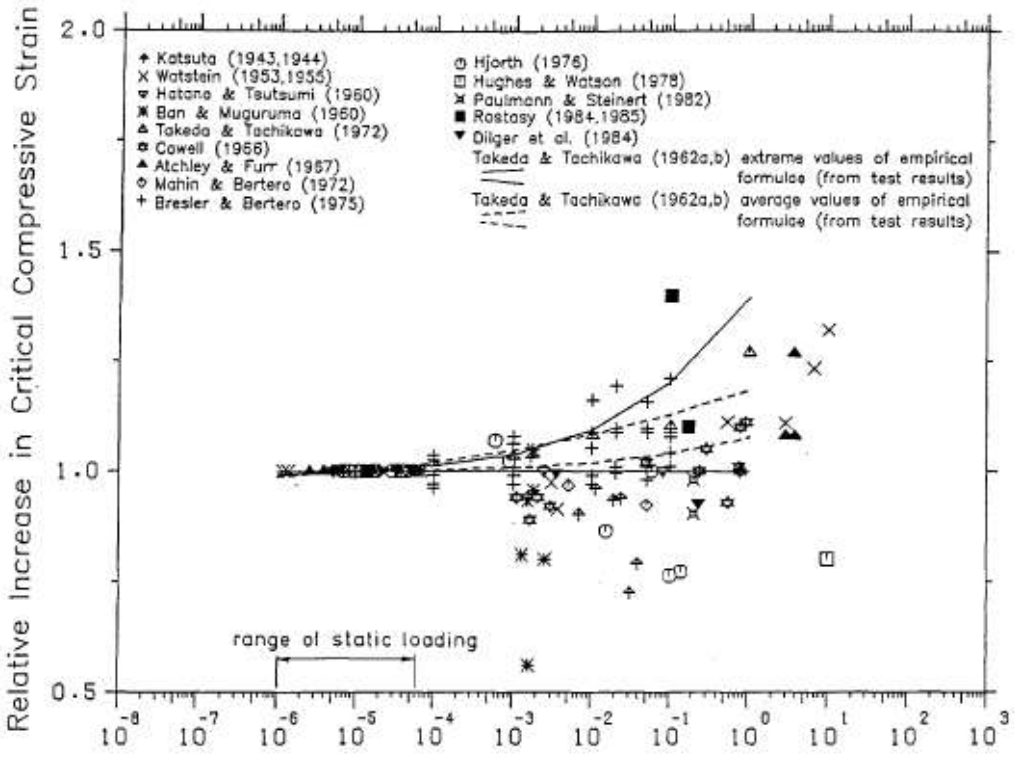

Figure 2-7 Strain Rate Influence on Critical Compressive Strain, picture reproduced from Bischoff et al. [2]

Figure 2-7 shows the relationship between critical compressive strains and strain rates for concrete summarized by Bischoff et la. [2]. Initially no trend could be discerned from the data. However after a detail observation, Bischoff [2] observed that all experiments which yield the result of decreasing critical strain with increasing strain rate utilized hydraulic machine. In true impact tests such as SHPB and drop hammer tests, the critical compressive strain was observed to increase as strain rate was increased.

2.4.3 Young's Modulus

It has been observed that the Young's modulus increases for the concrete as strain rate increases [2, 14, 28]. According to Bischoff et al. [2] this happen because there is a decrease in internal micro-cracking (for a given level of stress) with increased strain rate, resulting in a stress-strain curve that remains linear up to higher values of stress. On the other hand, Wang et al. [28] explained this happen caused by the relationship between crack velocity and strain rate in concrete. The crack velocity was observed to increase with increasing strain rate. However, crack velocity was still much slower compared to the wave propagation speed in concrete. With delayed response of strain with respect to high-velocity stress waves, the strain at a given stress decreases with the increase in strain rate. However Wang et al. explanation was wrong as concrete is not a viscoelastic material.

2.4.4 Energy Absorption per Unit Volume

It has been observed that the energy absorption per unit volume increases as strain rate increases [14, 17, 28]. As strain rate increases, more cracks form simultaneously in the specimen. The energy required to open a new crack is higher compared to the energy required to propagate cracks [27]. Therefore, the energy absorption tends to increase as strain rate increases.

Tai et al. [23, 24] studied the energy absorption of RPC with different volume fractions of steel fibers. They observed that the compressive strength increases as the strain rate is increased beyond a critical value. The energy absorption was also observed

to increase as strain rate was increased. A similar study has been performed by Wang et al. [30]. They use RPC with 2% steel fiber and observed that the compressive strength increases as strain rate increases. However, the analysis shows that the sample did not fail during the first wave pass.

2.5 Conclusions

From the literature review is it clear that concrete is a rate-dependent material. Under dynamic compressive loading, when strain rate increases, the compressive strength, critical compressive strain, Young's Modulus and the toughness of concrete will increase.

Although the rate dependence of the mechanical properties is evident in various types of concrete, till now, the effect of specimen size along with strain rate on the dynamic behavior of RPC has not been investigated. The main focus of this research is to find out how the specimen size affects the dynamic behavior of Cor-Tuf specimen at different strain rates.

CHAPTER 3. EXPERIMENTAL PROCEDURE

3.1 Specimen Preparation

Table 1-1 shows the composition of the Cor-Tuf used in current experimental study. A high shear batch plant with capacity of $1m^3$ was used to manufacture the Cor-Tuf. Four dry constituent materials (cement, sand, slica flour, slica fume) were pre-weighed and loaded into the mixer by hand followed by dry-blending for five minutes. After that, water and superplastizer were weighed and combined before being gradually added to the mixture which was actively mixing.

Table 3-1 Cor-Tuf Mixture Composition [9]

Material	**Product**	**Proportion by Weight**
Cement	Lafarge, Class H, Joppa, MO	1.00
Sand	US Silica, F55, Ottawa, IL	0.967
Silica Flour	US Silica, Sil-co-Sil 75, Berkeley Springs, WV	0.277
Silica fume	Elkem, ES 900 W	0.389
Superplasticizer	W.R. Grace, ADVA 170	0.0171
Water (tap)	Visksburg, MS municipal water	0.208

The mixing time was approximate 15 minutes to achieve paste condition. Resulting paste was mixed futher for 10 minutes. Total time for mixing was

approximately 25 minutes. The mixture was placed in bucket shaped molds with at 22^{o}C and 100% humidity. The molds were removed after 24 hours and remained at the facility for 7-days'. The specimens were then submerged in water with temperature of 85^{o}C for 4 days. Finally, the specimens were dried in an oven at 85^{o}C for two days. After drying the molds in oven, a suitable sized of core drill (inner diameter 19.05 mm, 76.20 mm) was used to drill out the Cor-Tuf specimens. After these, a wet saw was used to cut the specimen into a longer length than the desired length. After cutting, the specimen was placed into a jig and table grinder was used to polish one of the faces. Then the jig was flipped and the other face was polished to ensure the specimen did not move and become misaligned. This procedure was repeated until the final desired length was achieved. The two different size specimens of Cor-Tuf: 1) diameter 19.05 mm (0.75") by length 12.70 mm (0.5") 2) diameter 76.20 mm (3") by length 19.05 mm (0.75") that used in this study was prepared in the same manner. The complete manufacturing procedure for the Cor-Tuf required 13 days in total. Following the standard procedure (ASTM) C 39 (ASTM 2005a) the compressive strength of Cor-Tuf under quasi-static loading was determined to be 190 MPa-240 MPa [9].

3.2 Kolsky Bar Apparatus

A typical Kolsky bar consists of a gas gun, striker, incident bar, transmission bar and momentum trap bar. Two different sizes of Kolsky bar were fabricated using VascoMax C-350, also known as maraging steel were used in this study: i) a big Kolsky bars ii) a

small Kolsky bars. The geometric dimensions of both the bars are presented in Table 3-2. The Mechanical properties of maraging steel are presented in Table 3-3

Table 3-2 Properties of Kolsky Bars

Properties	Big Kolsky Bar	Small Kolsky Bar
Diameter [mm]	76.20	19.05
Length of Incident Bar [mm]	3048.00	4165.60
Length of Transmission Bar [mm]	3048.00	1473.20

Table 3-3 Properties of VascoMax C-350

VascoMax C-350	
Density [kg/m^3]	8100
Young's Modulus [GPa]	210
Wave Speed [m/s]	5092

Uniaxial compressive stress wave was generated by impacting a striker on the incident bar using a gas gun. The generated compressive wave propagated through the incident bar to the specimen and finally to the transmitted bar. Figure 3-7 shows the complete acquisition system for the Kolsky Bar. In order to record the strain history of the bars, two pairs of strain gages were attached on the incident and transmitted bars respectively. The pair of strain gages were attached on the surface on the bar 180 degree apart to eliminate the recording of bending waves. The strain gages then were then connected to the Wheatstone bridge. To amplify the signal, preamplifiers were used after the Wheatstone bridges. The preamplifiers were then connected to the oscilloscope for recording the raw pulse signals.

The strain gages used in this experiment were manufactured by Vishay Mcro-Measurements (WK-13-125Z-10C) with a resistance of 1000Ω and gage factor of 2.08. The signals were converted to strain by using the formula:

$$\varepsilon = \frac{2V_{out}}{G_f V_{in}} \qquad \text{Equation 3.1}$$

where V_{out} is the output voltage that been measured using oscilloscope

To ensure that the specimen deformed at a constant strain-rate as well as achieved stress equilibrium, a cylindrical shape piece of copper which acted as a pulse shaper [10, 11] was placed on the non-specimen end of the incident bar. This technique is discussed in details in section 3.3.

Figure 3-1 shows the strain history in the incident bar when a striker impacts the incident bar with a gap between the incident and transmitter bar. A compressive wave (A) was generated and propagated through the incident bar. Due to the gap, the wave reached the free end of the incident bar and reflected back (E). Note that the incident wave is compressive (+) and the reflected wave is tensile (-).

The distance between the strain gage and the bar end was 1644.65 mm (64.75”) and the time used to travel to the end and back to the strain gage(C) was about 662.6 μs The experimental bar wave speed can be calculated using following formula:

$$C_{exp} = \frac{2L_{sg}}{t_c} \qquad \text{Equation 3.2}$$

where L_{sg} is the distance between strain gage and the bar end, t_c is the time used to travel to the end and back to the strain gage

From the calibration, the experimental bar wave speed was determined to be around 5000 m/s which matches the theoretical bar wave speed 5100 m/s.

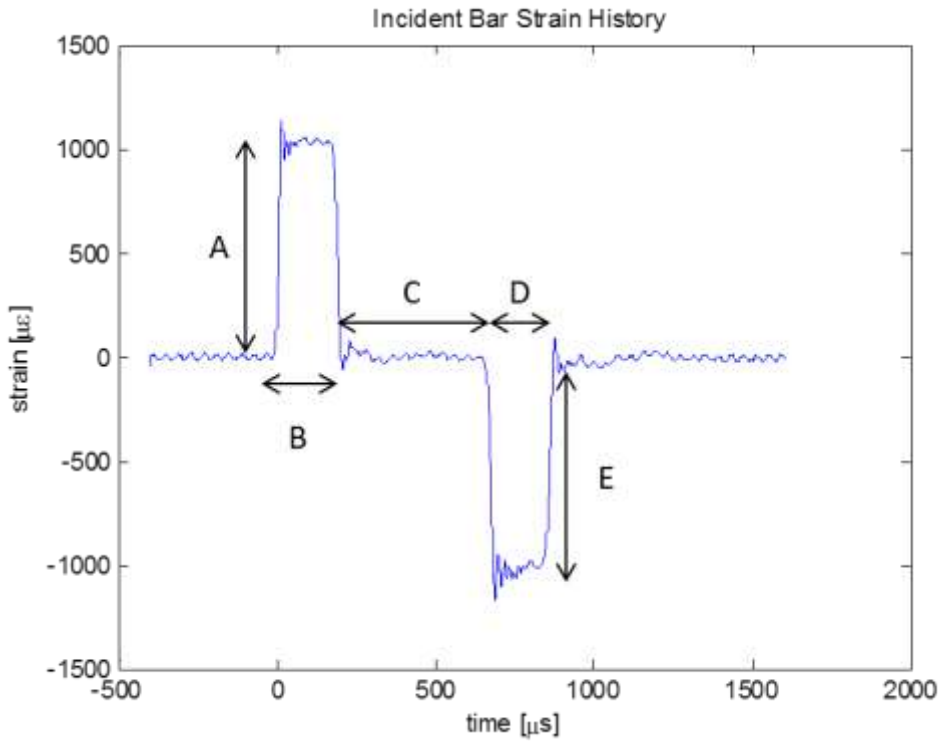

Figure 3-1 Incident Bar Strain History

By using 1D wave theory, the strain in the incident and transmission bar was converted to a set of dynamic stress-strain curves. A high speed camera (Cordin 550) was used in a representative set of experiments to record the high speed images to characterize the failure modes.

In current experiments, lubricant (Vaseline) was applied on both end faces of the sample to minimize friction between bar-ends and the sample [2]. The sample was then sandwiched between incident and transmission bar as shown in Figure 3-3.

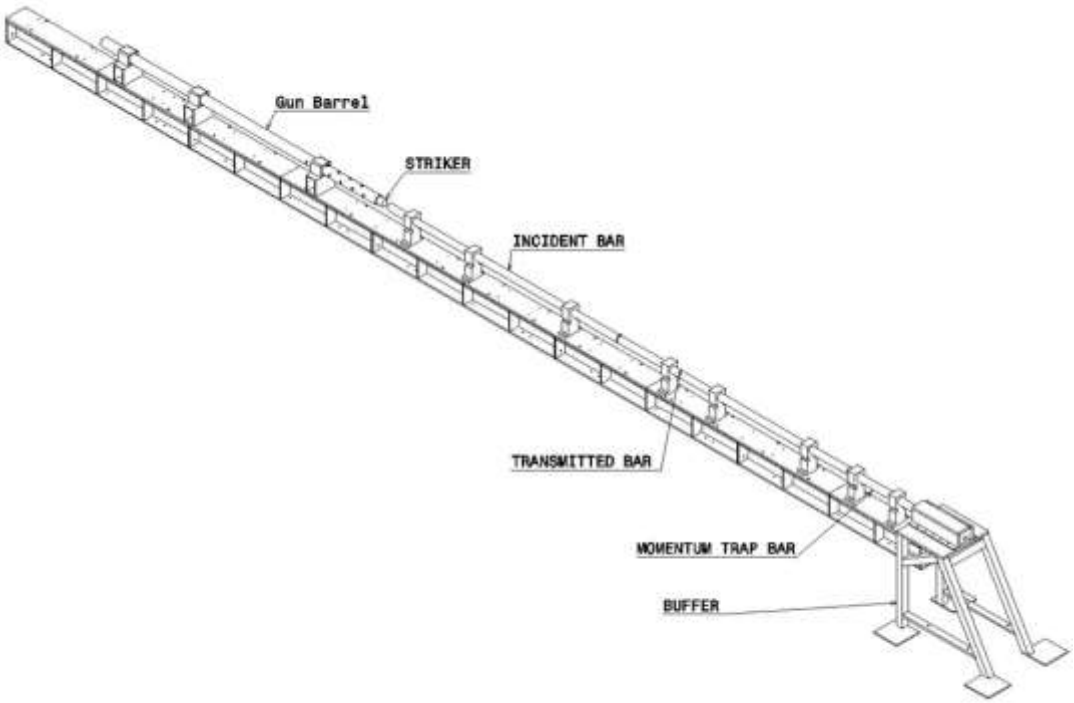

Figure 3-2 Isometric View of 3" Kolsky Bar

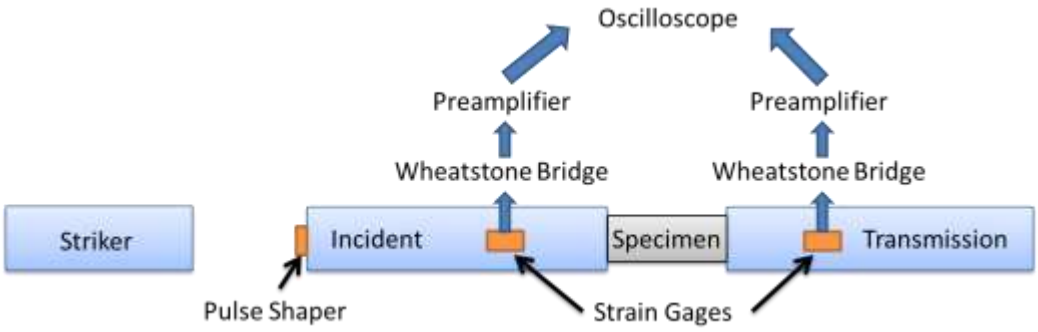

Figure 3-3 Data Acquisition for Kolsky Bar

3.3 Pulse Shaping Technique

Concrete is a brittle material which usually breaks at less than 1% strain under uniaxial compressive loading. In most cases, if the rectangular incident pulse was utilized,

concrete fails at fairly early stage. This prevents the specimen from achieving dynamic stress equilibrium as well as constant strain rate.

In order to deal with this problem, pulse shaping technique was introduced. Pulse shaping is a technique used to achieve desired incident pulse. This is essential as it helps specimen achieve constant strain-rate as well as stress equilibrium. To allow a brittle material to deform at a constant strain-rate and achieve stress equilibrium, it is necessary that the incident pulse has a ramp shape [10].

Duffy [3, 6] was probably the first person to use pulse shaping to smooth the pulse generated by the explosive loading on torsional Kolsky bar. Christistensen [3, 4] used pulse shaping on Kolsky bar to get ramp pulse. They employed conical shaped striker instead of a cylindrical shaped striker. By doing so, a ramp incident pulse was generated instead of a square pulse. A more accurate compressive stress-strain response for rocks was investigated using the pulse shaping technique. Although a desired pulse could be obtained using this technique but it was difficult to design and fabricate a conical striker.

The second technique for obtaining the desired pulse was to use a “three bar technique” by adding a pre-incident bar in front of the incident bar.[3, 8] A dummy specimen that was manufactured from the same material as the specimen was placed in between pre-incident and incident bar. The dummy specimen was usually slightly larger than the specimen. By doing so the incident pulse generated in the incident bar was same as the transmission pulse. This allowed the real specimen to deform at a constant strain-rate as well as achieve constant strain-rate.

The third technique which is also the technique which is implemented in this study is utilizing a circular piece of material usually made up with copper which is known as “pulse shaper”. There are several parameters that influence the shape of the pulse including pulse shaper material, dimension, striker material, striking velocity etc. The pulse shaper was placed in front of the incident bar as shown in Figure 3-3. When a striker strikes, the pulse shaper acts as a cushion. The code provided by Frew[10, 11] was utilized to aid in designing the suitable pulse shaper.

After getting the general idea on the pulse shaper, few experiments were done and changes to the pulse shaper were made in order to ensure that correct pulse shaper were used to get the ramp pulse.

Figure 3-4 compares the simulations results with the experimental for small Kolsky bars. For simulation, the pulse shaper had dimensions of length 1.64 mm and the diameter range from 7 to 9 mm. For experimental case the pulse shaper has a length of 1.64 mm and diameter of 7.36 mm. The length of the striker was 457.2 mm (18”) and it was travelling at 19.5 m/s. From the figure it can be observed that the simulation provided by Frew predicted the incident pulse accurately.

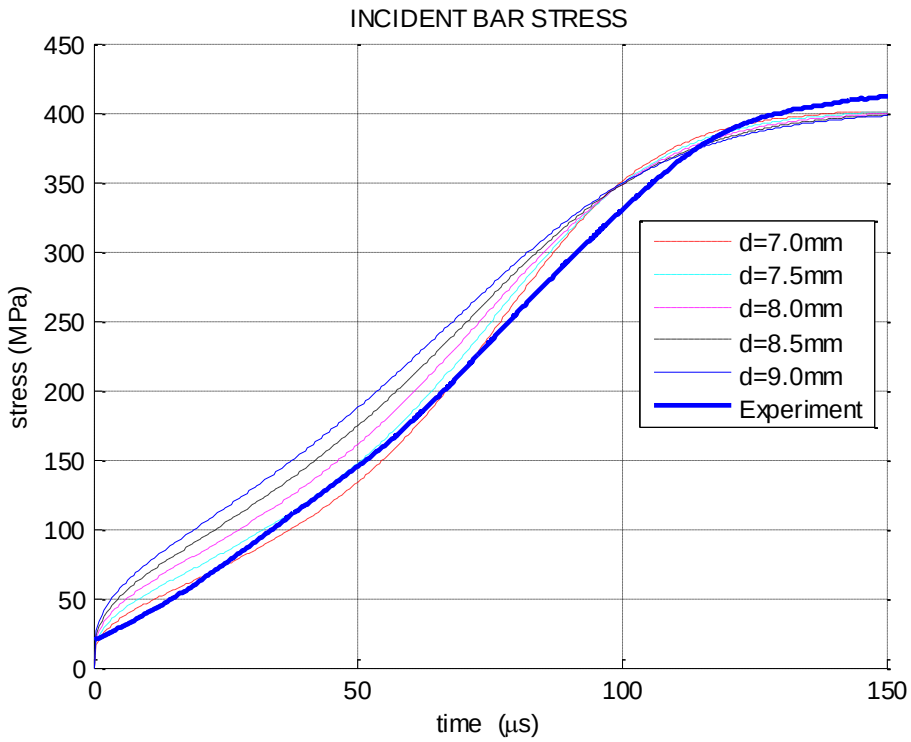

Figure 3-4 Comparison of simulation with experimental incident pulse for small diameter bar

Since the pulse shaper and the bars are linear elastic materials, so initially for large Kolsky Bars (3" diameter), it was postulated that the desired ramp pulse could be obtained by increasing the diameter of pulse shaper. Figure 3-5 compares the simulations results with the experimental results for the large diameter bar. For experimental results, the pulse shaper was placed in between incident and transmission bar such that the experimental pulse shown in the Figure 3-5 was actually the transmission pulse in the experiment. This setup was utilized to calculate the radial stress induced by radial inertia. The experimental pulse shaper had dimensions of length 1.1 mm and diameter 40 mm. The length of the striker is 304.8 mm (12") and it was

travelling at velocity 15 m/s. From the figure, it can be observed that the prediction using Frew simulation was inaccurate. This was probably because the simulation did not account for the radial stress induced by radial inertia.

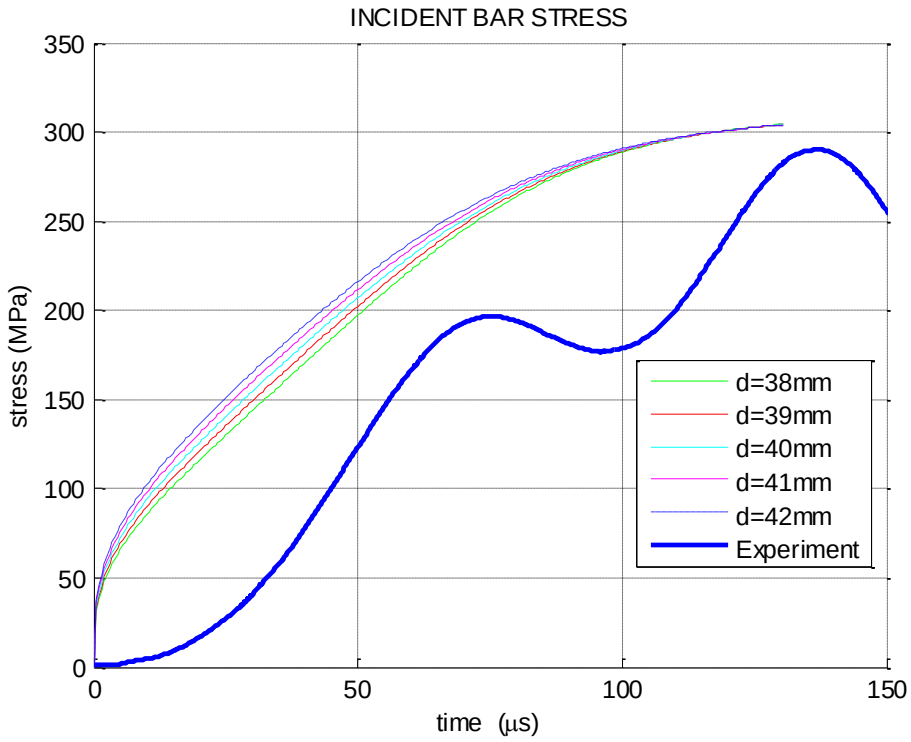

Figure 3-5 Comparison of Simulation with Experimental for Large Diameter Bar

According to Warren et al. [31], the radial inertia can be calculated by

$$\bar{P} = \frac{3\rho a_o^2}{16(1-\varepsilon_x)^3}\dot{\varepsilon}_x^2 + \frac{\rho a_o^2}{8(1-\varepsilon_x)^2}\ddot{\varepsilon}_x \qquad \text{Equation 3.3}$$

Figure 3-6 compares the stress in the transmission bar with the stress induced by the radial inertia. Under dynamic loading the axial stress contains 2 components; the actual axial stress and the stress induced by the radial inertia which acts as pressure. The radial inertia induced stress scales as the square of the diameter of the pulse shaper.

If the diameter of the pulse shaper increases by 4 times, it increases the stress induced by radial inertia 16 times. From the Figure 3-6, from time 90 µs to 110 µs the transmission stress is drops by 20 MPa from 200 MPa to 180 MPa. During the same time the change in the radial inertia calculated using equations 3.3 is about 66 MPa. This discrepancy may be because of the assumption of the retention of the shape of pulse shaper after the experiment in equation derived by Warren et al. which was observed to be false during the course of this study.

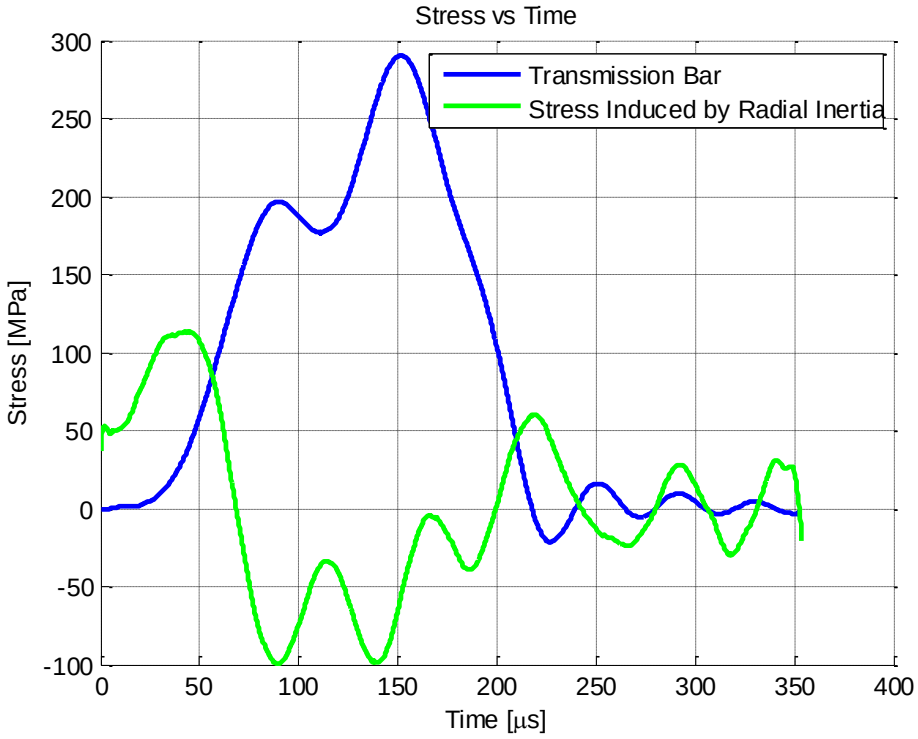

Figure 3-6 Transmitted Bar Stress and Stress Induced by Radial Inertia vs time

To overcome this problem, an annulus pulse shaper was used. Annulus pulse shapers have lesser radial inertia than the circular pulse shaper [22] and hence generate uniform ramp loading for bigger diameter bars. Figure 3-12 shows the incident pulse for a copper

pulse shaper with dimensions of outer diameter 46.45 mm, inner diameter 35.62 mm and thickness of 1.68 mm. Using this method, a ramp shaped incident pulse was obtained.

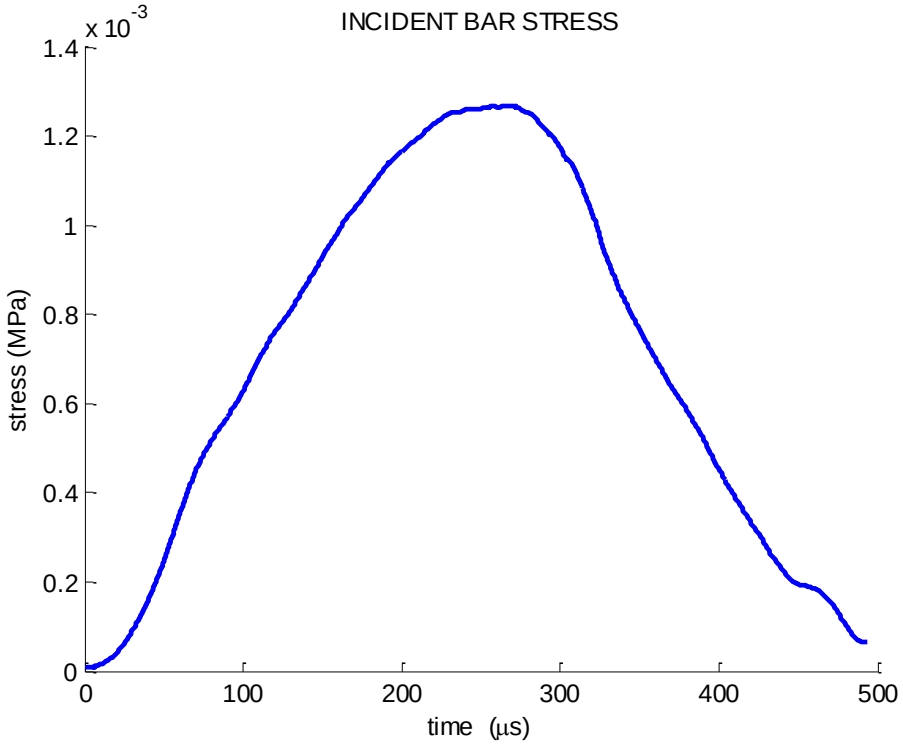

Figure 3-7 Incident Pulse for Annulus Pulse Shaper

In conclusion, a circular pulse shaper was utilized to generate a ramp pulse in small diameter bar. On the other hand, to reduce the stress induced by radial inertia, an annulus shaped pulse shaper was used in the large diameter bar.

3.4 High Speed Camera

In some of the experiments, high speed camera was incorporated to observe how the sample fails. The high speed camera used in this experiment was Cordin 550 which is

able to take 32 shots of high speed images at a resolution of 1 megapixel at maximum 2 million frames per second. External trigger was connected from the oscilloscope to the high speed camera to trigger the high speed camera.

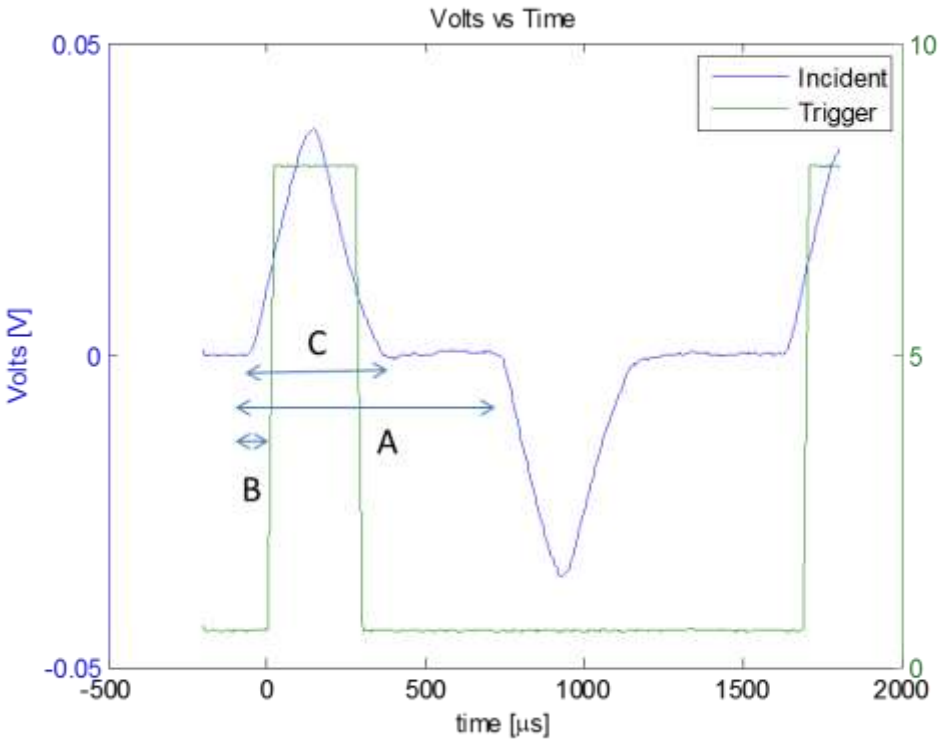

Figure 3-8 Incident Strain History and Trigger Signal

Figure 3-8 shows the trigger signal and incident strain history vs. time. When the oscilloscope was triggered, 8 V rising signal was sent from external trigger to the high speed camera. Time used for the incident pulse to propagate from the strain gage to the end of incident bar and reflect back to the strain gage is represented by A as shown in the figure. Time taken by the signal to reach the end of incident bar is 0.5A. Trigger delay signal was generated at time B. Therefore the delay trigger t_d can be calculated from

$$t_d = \frac{A}{2} - B$$ Equation 3.4

Since the camera was capable of taking 32 shots and the sample failed during the first pulse length which is indicated as C. The frame rate can be determined using equation 3.5.

$$frame\ rate = \frac{32}{C}$$ Equation 3.5

3.5 Experimental Sequence

In a typical Kolsky bar experiment, first the bar was calibrated using Equation 2.6. Then dimensions including diameter and length as well as the weight of the specimen were recorded. After that, the suitable material, size and shape for the pulse shaper were determined before cutting the pulse shaper to the desired shape. Subsequently, the data acquisition system was setup. After setting up the system, the Wheatstone bridges were balanced and the recording system (digital oscilloscope) was triggered. After that, the pulse shaper was placed in front of the incident bar using Vaseline. To minimize the end effects, lubrication was applied on the face of the specimen and the specimen was sandwiched in between the incident and transmission bar.

After completing the setup, the striker was launched using the gas gun to achieve desired striking velocity. When the striker struck the pulse shaper, a desired ramp pulse was generated in the incident bar. The compressive incident pulse propagated through the incident bar and reached the specimen. Part of the pulse was reflected back at the bar specimen interface and part of it was transmitted to the

sample. The pulse travelling to the sample reached the transmission face and part of it was transmitted as the transmitted pulse and part of it was reflected back to the sample. The pulse bounced back and forth in the specimen to build up the stress level in the specimen. When the stress level reached the compressive strength, the sample failed.

3.6 Data Reduction

Figure 3-9 shows the typical raw data that was obtained from the Kolsky Bar experiment. The strain history recorded by the incident strain gage as shown in black in the figure 3-9 contains the information on the incident and reflected pulse. Similarly, the transmitted strain gage pulse contains the transmitted pulse. By using appropriate time shifting scheme, the incident, transmitted and reflected pulse were obtained.

After the time was shifted properly, the incident, reflected and transmitted that were obtained are shown in Figure 3-10. To utilize the Kolsky bar equations, specimen must be in dynamic equilibrium. This was checked by adding the incident and reflected pulses and comparing with the transmitted pulse. If they were in good agreement then it was concluded that the specimen is in dynamic stress equilibrium. Kolsky Bar equations were applied only for the specimens for which dynamic equilibrium was verified.

Figure 3-12 shows the strain-rate vs. time obtained from one of the experiment. The strain rate was calculated using Equation 2.17. Plateau region can be clearly observed in the Figure 3-12. Hence it can be concluded that the specimen deformed at a

specific constant strain-rate. The strain rate was obtained by averaging the values in the plateau region.

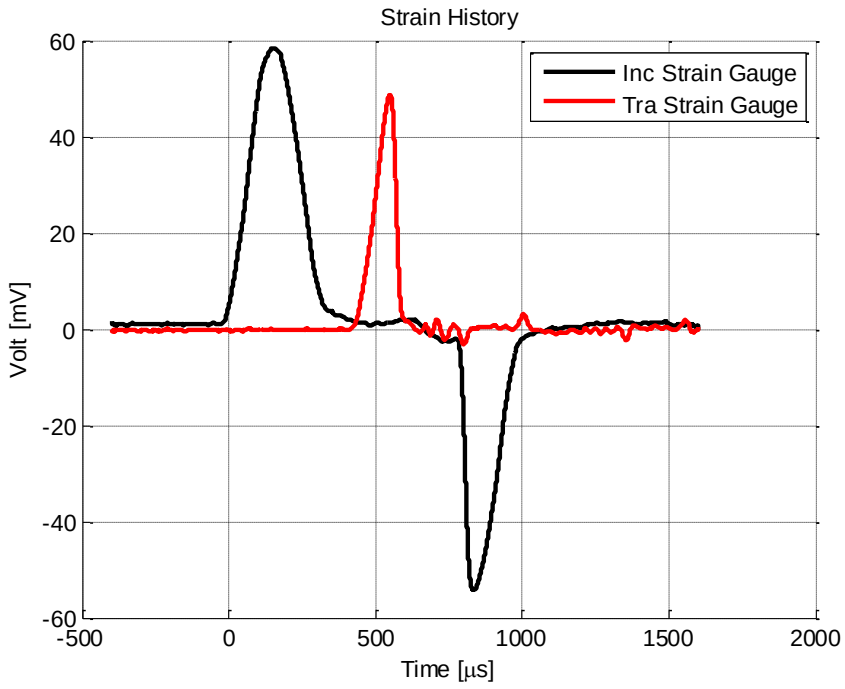

Figure 3-9 Experimental Records from a Typical Kolsky Bar Experiment

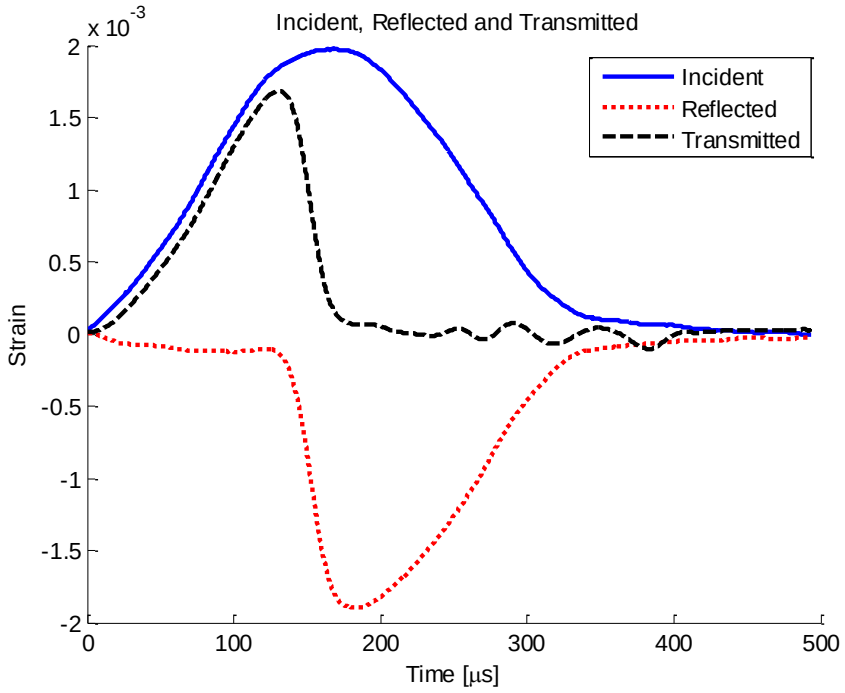

Figure 3-10 Incident, Reflected and Transmitted Signal

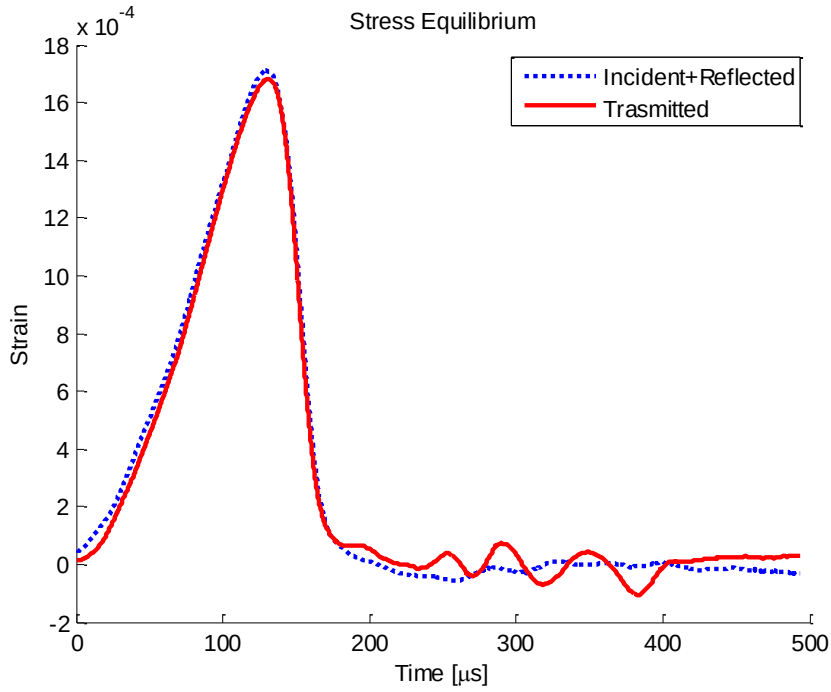

Figure 3-11 Stress Equilibrium

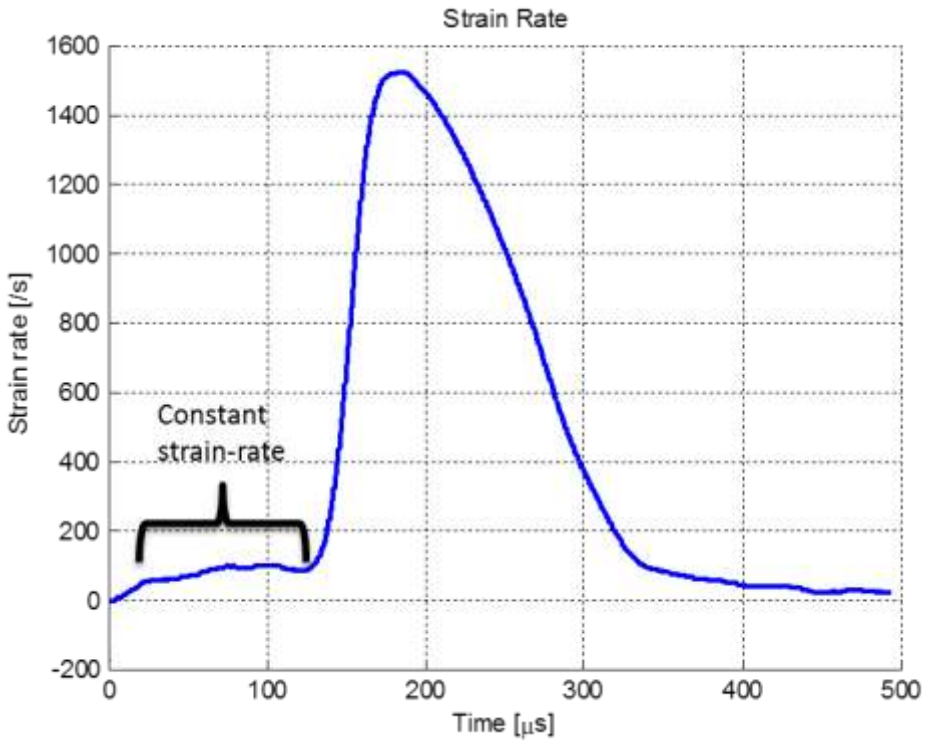

Figure 3-12 Strain Rate vs Time

Figure 3-13 shows the stress strain curve at a specific constant strain rate where several important parameters such as compressive strength, critical strain, critical energy absorption per unit volume, and Young's modulus were determined. The compressive strength is the highest peak in the stress-strain curve. However in order to get compressive strength it was important that the specimen fails catastrophically during the first pulse. The justification of failure will be discussed in section 4.1. The strain corresponding to the compressive stress is defined as the critical strain. The slope of the curve is defined as the Young's modulus. Finally the area under the stress strain curve up to failure is defined as the critical energy absorption per unit volume.

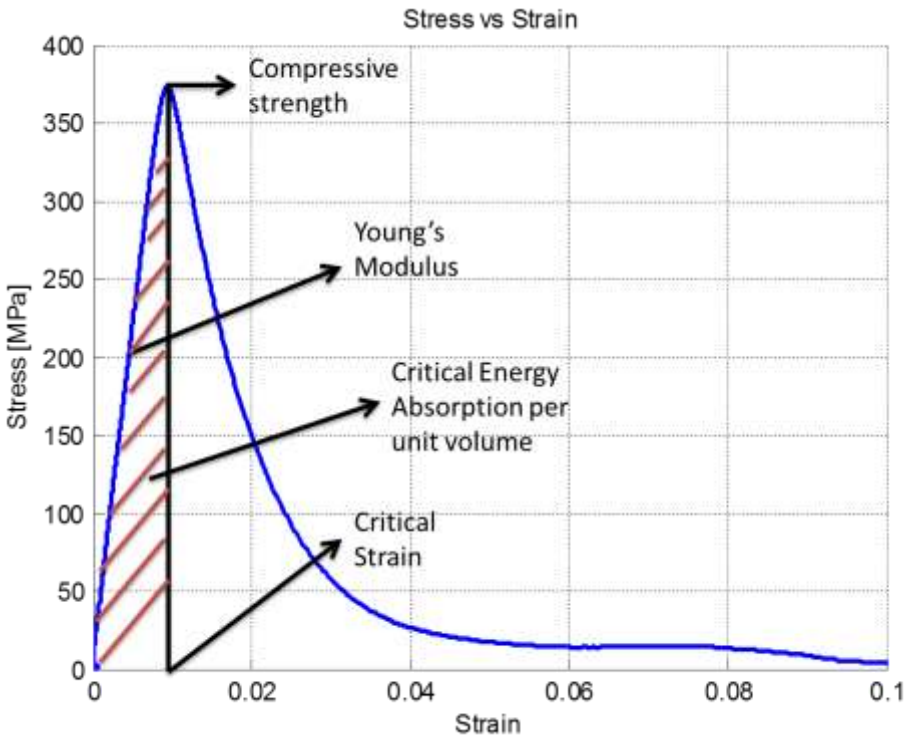

Figure 3-13 Stress Strain Curve

CHAPTER 4. RESULTS AND DISCUSSION

4.1 Verification of Failure During First Wave Pass

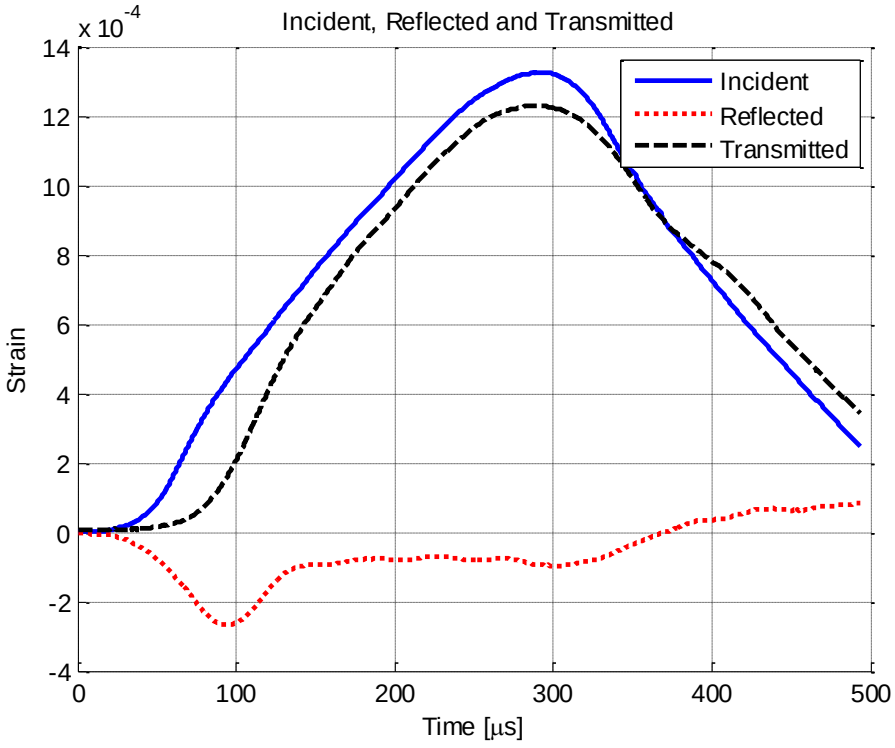

Figure 4-1 Incident, Reflected and Transmitted Signals on Sample that Did Not Fail Catastrophically

To ensure that the compressive strength can be obtained accurately, it is very important to ensure that the specimen failed catastrophically during the first pulse. This was done by checking the reflected wave. Since concrete is a brittle material, it leaves a free surface when it fails catastrophically. According to 1-D wave theory when a compressive

stress wave propagates to a free surface, it reflects back as tension with the same magnitude. By ensuring that the plateau region of the reflected wave is followed by a sharp decrease in value, thereby indicating the aforementioned free surface reflection, it can be concluded that the sample has failed during the first loading pulse and compressive strength is obtained. For clarification, both valid and invalid tests are described in Figures 3-10 and 4-1, respectively. Figure 3-10 demonstrates a proper reflected waveform history, wherein the sample is deformed in a constant strain rate environment as described by the reflected signal plateau region lasting from 27 μs to 113.6 μs us followed immediately by a sharp decrease in signal, thereby indicating incident bar acceleration resulting from sample free surface generation due to sample fracture. In contrast, as can be seen in Figure 4-1, the sample undergoes a constant strain rate deformation defined during the time period of 120 μs to 296 μs, but due to the lack in sample failure, no free surface at the bar end is created and the sample simply unloads with the passage of the stress wave. Figure 4-1 shows the incident, reflected and transmitted pulses for the specimen that did not fail catastrophically. The plateau region clearly remained on the reflected pulse, moreover when unloading the reflected wave was observed to increase in magnitude. This was probably because of the tension wave sent back in the incident bar by partially damaged specimen trying to return to the original length.

4.2 Results for Small Cor-Tuf Under Dynamic Compressive Loading

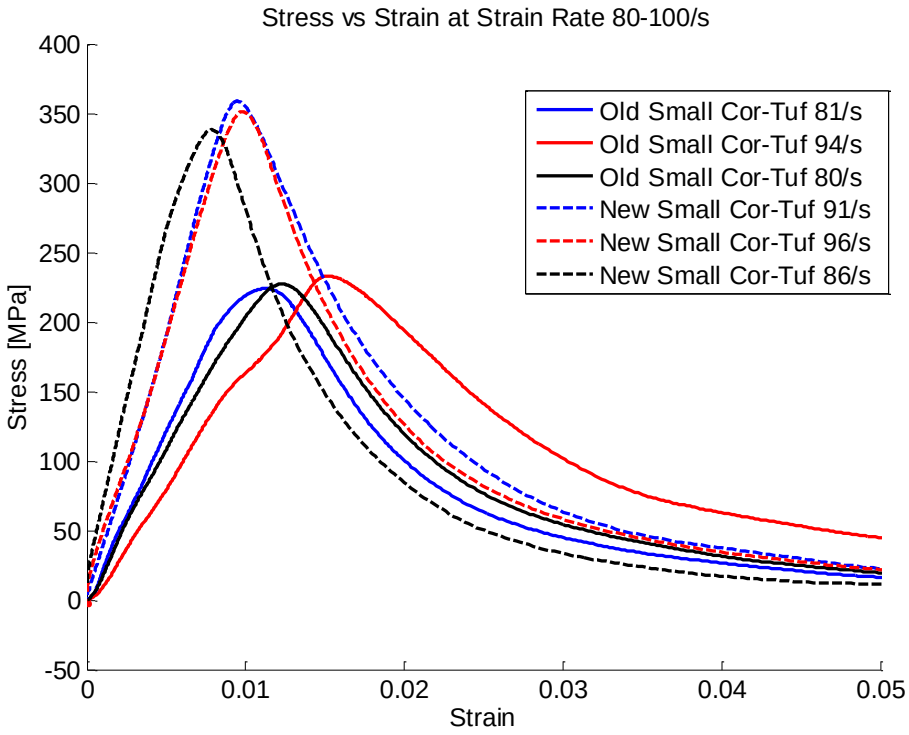

Figure 4-2 Stress Strain Curve for Small Cor-Tuf

For small Cor-tuf (diameter 0.75”), two different batches of Cor-Tuf were obtained from ERDC at different times. The first batch is henceforth called “old small Cor-Tuf” and the second batch is called “new small Cor-Tuf”. According to the manufacturer, the mechanical properties might be slightly different from batch to batch. Figure 4-2 shows the comparison in the stress-strain curve for different batches at strain rate around 100/s. From the figure, it can be observed that the new Cor-Tuf had higher compressive strength and Young’s Modulus and lower critical strain compared to the old Cor-Tuf.

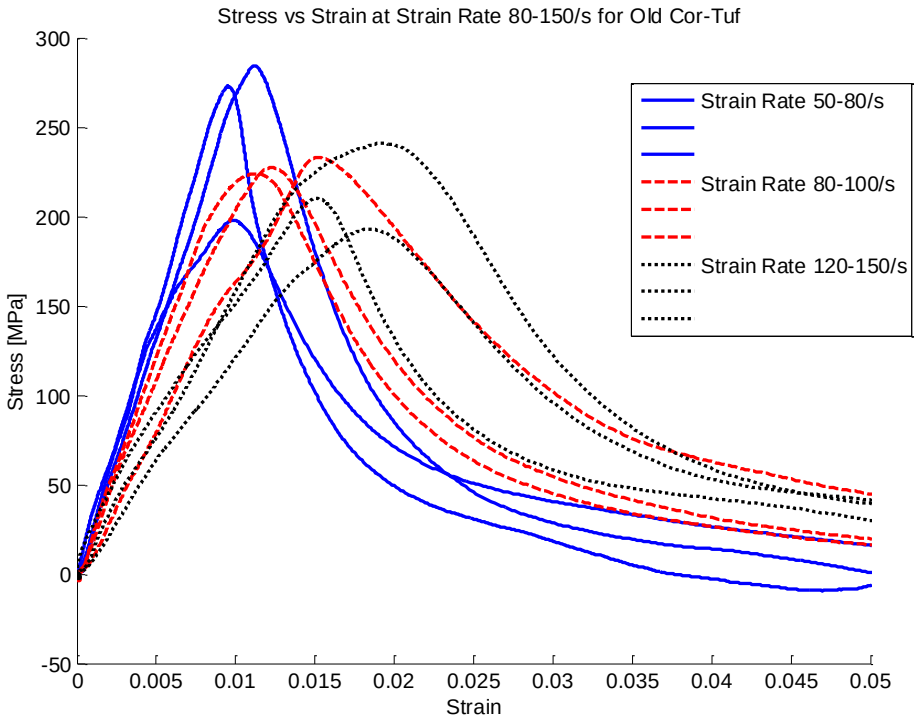

Figure 4-3 Stress Strain Curve at Different Strain Rate for Small Old Cor-Tuf

Figure 4-3 compared some of the stress-strain curve for the old Cor-Tuf at different strain rates. It can be observed that the strength and Young's Modulus decreased as strain rate was increased. However, the critical strain increases as strain rate increases. The summary of all the properties is presented in section 4.4.

To investigate the reasons behind the counter-intuitive trends observed in the experiments on the small Cor-Tuf, all specimens of the new small Cor-Tuf were loaded with the same incident pulse.

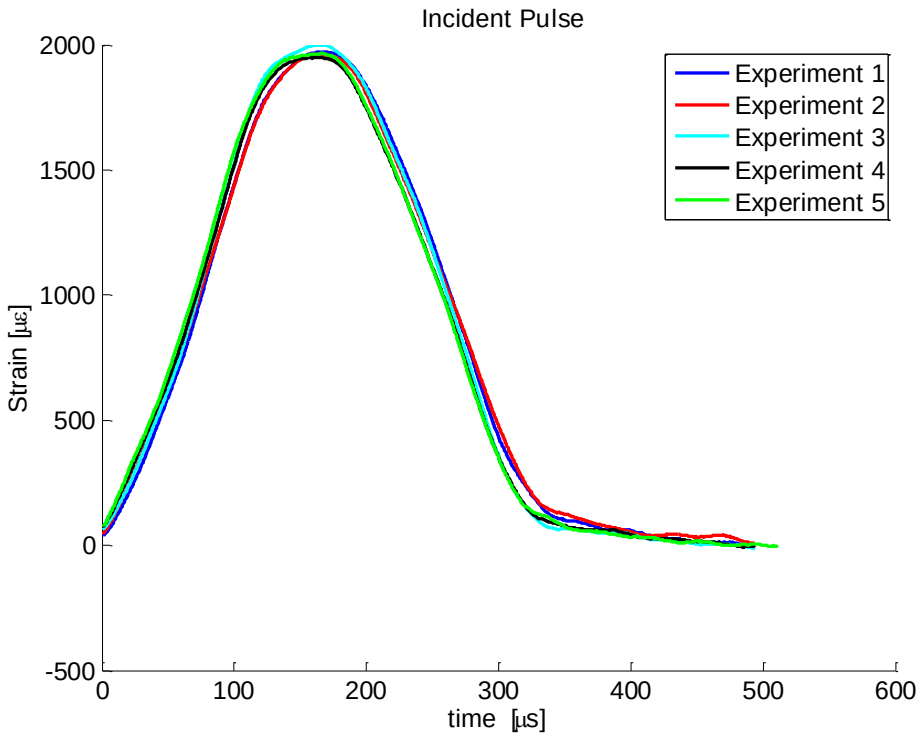

Figure 4-4 Incident Pulse for the New Small Cor-Tuf

Figure 4-4 shows the incident pulse used to load the new small Cor-Tuf. From the figure, it can be observed that the incident pulse for all experiments had the same shape which proves that all the specimens were loaded using the same loading.

Figure 4-5 shows transmitted pulse obtained from the experiments. The compressive strength of the specimens was directly related to the magnitude of the transmitted pulse. From the figure, it shows that the specimens in experiment 1 and 2 had higher strength compared to experiment 3 and 5 since the transmitted pulse has higher magnitude at the peak.

Figure 4-6 shows the obtained reflected waves. The strain rate is related to the reflected pulse. More negative the reflected pulse, higher the strain rate. From the

figure it can be observed that experiment 3 and 5 had higher value of strain rate compared to experiment 1 and 2.

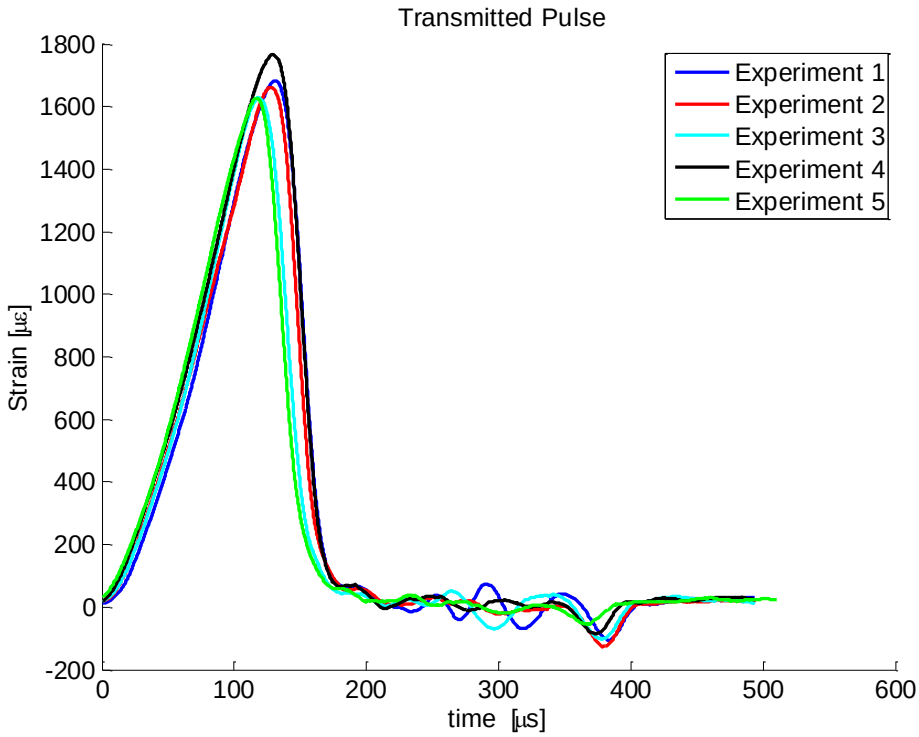

Figure 4-5 Transmitted Pulse for the New Small Cor-Tuf

Figure 4-7 shows the stress vs. strain curve obtained from the new Cor-Tuf. Since the generated incident pulse will split into incident and transmission pulse after loading, higher magnitude of the transmitted wave for stronger Cor-Tuf will lead to lower magnitude in reflected pulse.

Hence, the reason behind the decreasing strength with strain rate is the intrinsic behavior of Cor-Tuf. Since some specimens of the Cor-Tuf were stronger than others, the transmitted pulse became higher thus lowering the reflected pulse which gave rise to lower strain rate.

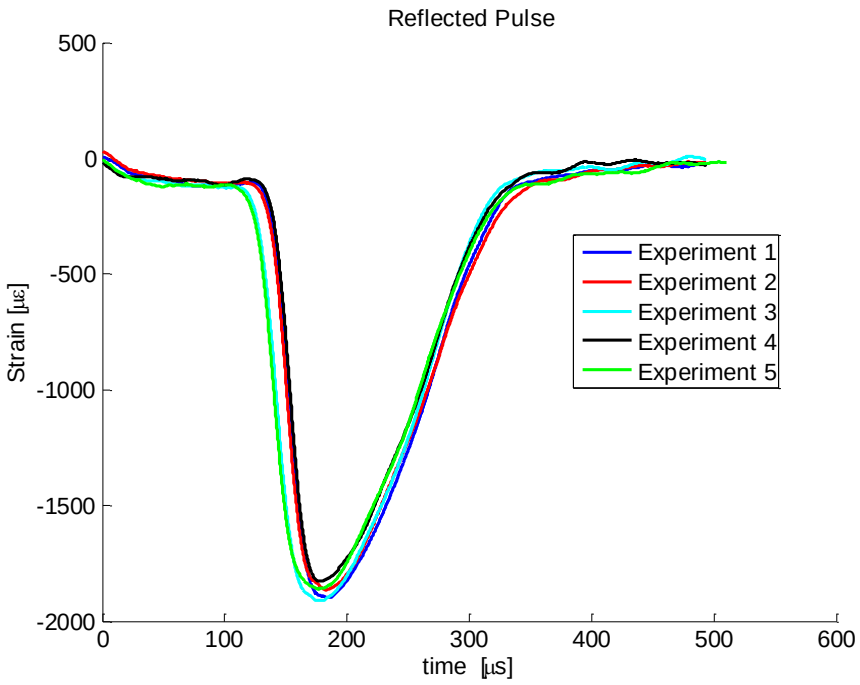

Figure 4-6 Transmitted Pulse for the New Small Cor-Tuf

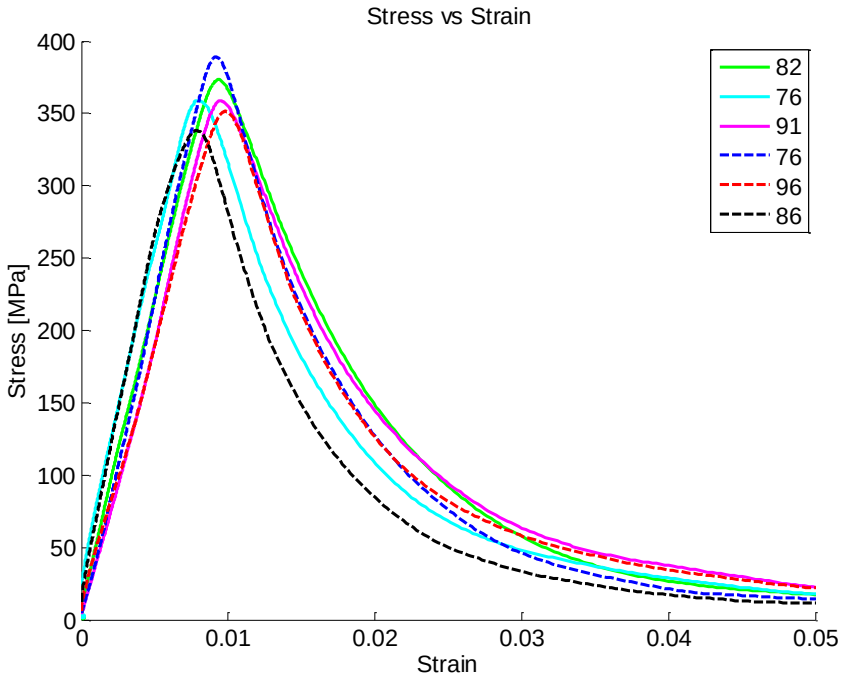

Figure 4-7 Stress Strain Curve for New Small Cor-Tuf

4.3 Results for Big Cor-Tuf Under Dynamic Compressive Loading

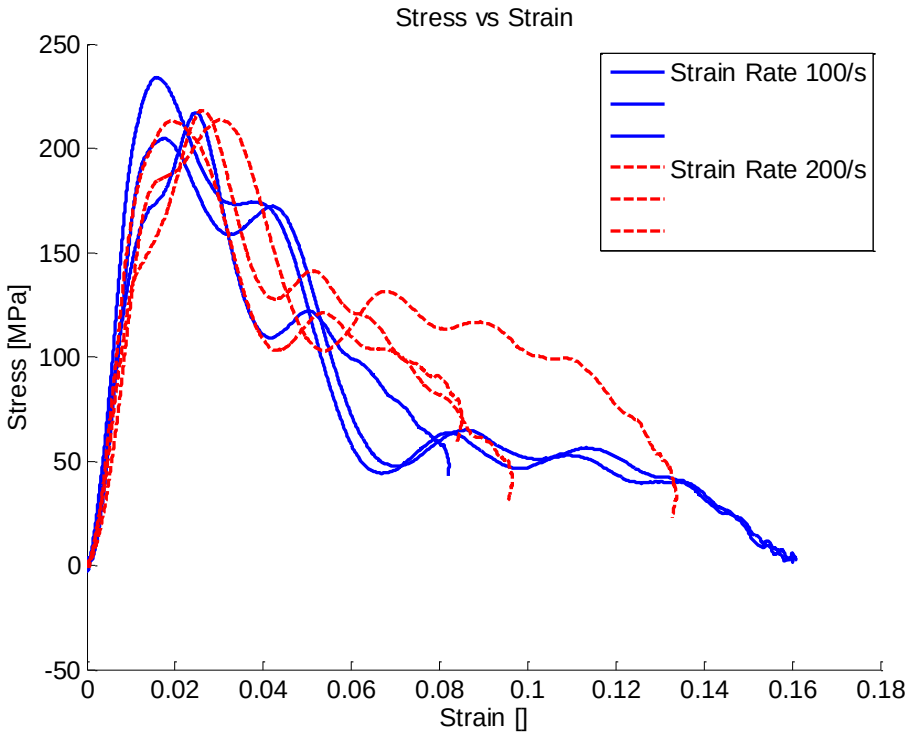

Figure 4-8 Stress Strain Curve for Big Cor Tuf

Figure 4-8 shows the stress strain curve for new big Cor-Tuf. The compressive strength and Young's modulus do not show significant change as the strain rate increases. However the critical strain and critical energy absorption increases as the strain rate increases. Besides that, the post-peak ductility in the big Cor-Tuf can be clearly observed. Initially the stress is in a linear relation with the strain until the strain reaches around 1%. The specimen had already failed at strain around 1% however the outer part of the specimen held the failed specimen together due to radial stress that was induced by inertia. Hence the specimen can take further load. The specimens showed softening

behavior after 1% strain which further proved that the specimen was already failed and was only supported by radial inertia stress.

4.4 Comparison of Results for Different Size Cor-Tuf

4.4.1 Compressive Strength

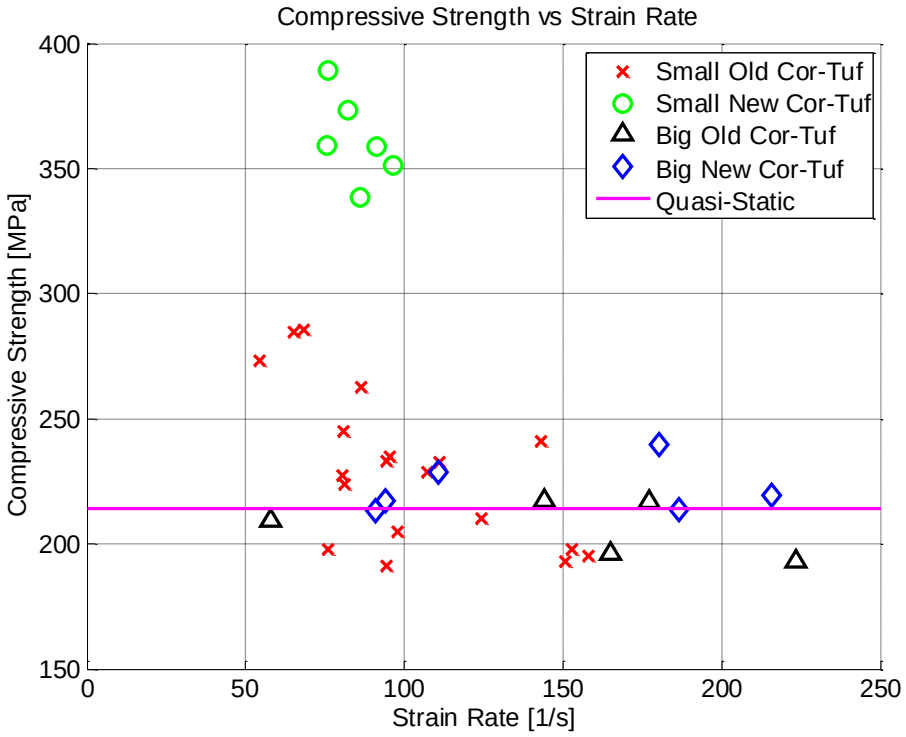

Figure 4-9 Compressive Strength vs Strain Rate

Figure 4-9 shows the compressive strength vs. strain rate for the Cor-Tuf. For the big Cor-Tuf, the strength does not change significantly as the strain rate increases. This might due to the fact that the amount of flaws was almost the same for all the specimens of the big Cor-Tuf. The compressive strength for new small Cor-Tuf is higher

compared to the old small Cor-Tuf. This proves that the mechanical properties of Cor-Tuf change from batch to batch. However, for all the small Cor-Tuf specimens, strength is decreases as the strain rate increases due to the intrinsic behavior of small Cor-Tuf.

4.4.2 Critical Energy Absorption per Unit Volume

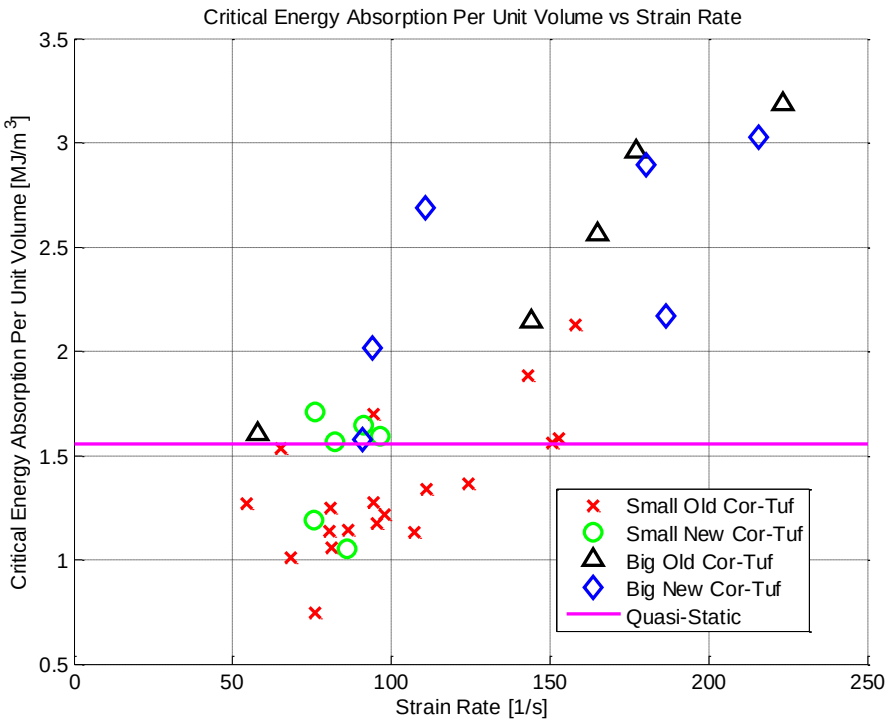

Figure 4-10 Critical Energy Absorption per Unit Volume vs Strain Rate

Figure 4-10 shows the critical energy absorption per unit volume vs. strain rate for both small and big Cor-Tuf. The critical energy absorption is the area under the stress strain curve up to failure. It can be observed the critical energy absorption per unit volume increases as strain rate increases. The probable reason behind the increase is the increase in the number of cracks in the specimen with increasing strain rate. Since the

energy used to open a new crack is much more than the energy used to propagate a crack, higher number of cracks led to higher critical energy absorption per unit volume as strain rate was increased. For big Cor-Tuf, the value is higher compared to small Cor-Tuf because big Cor-Tuf can take load after failure due to radial inertia that acts as confinement.

4.4.3 Critical Strain

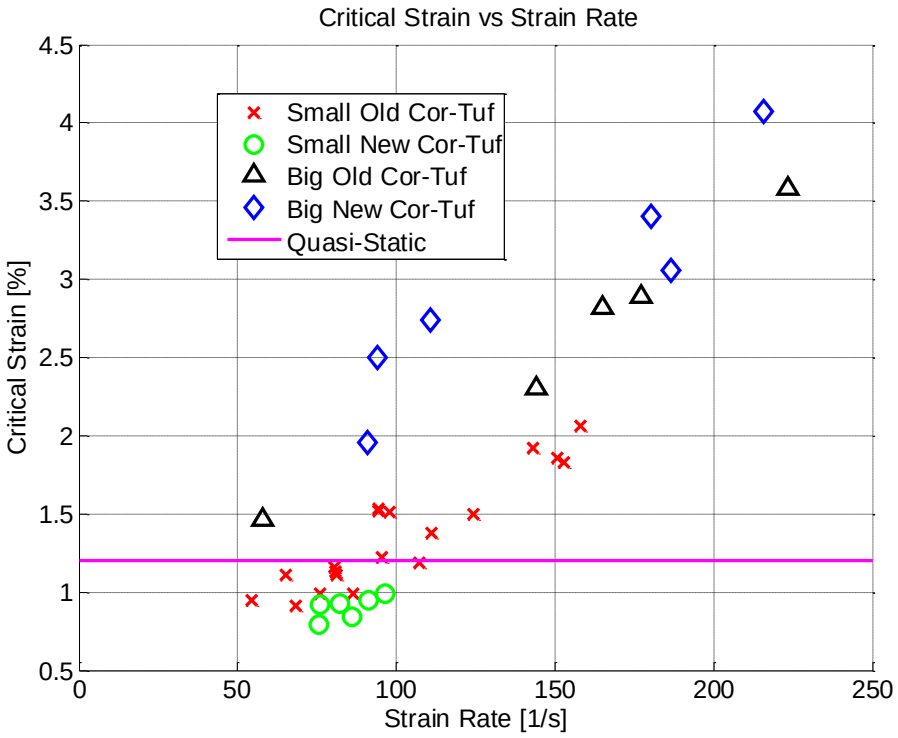

Figure 4-11 Critical Strain vs Strain Rate

Figure 4-11 shows the critical strain vs. strain rate for small and big Cor-Tuf. The critical strain can be observed to increase as strain-rate was increased. This is the same trend that has been observed in the literature. The reason might be larger number of flaws in

some specimens compared to other specimens. Specimen with more flaws generally is weaker which leads to a lower compressive strength hence lower transmitted pulse with higher reflected pulse. Since strain rate and strain are related to the magnitude of reflected pulse, more flawed specimen gives rise to higher strain as well as strain rate. Hence as strain rate increases the critical strain of Cor-Tuf also increases.

4.4.4 Young's Modulus

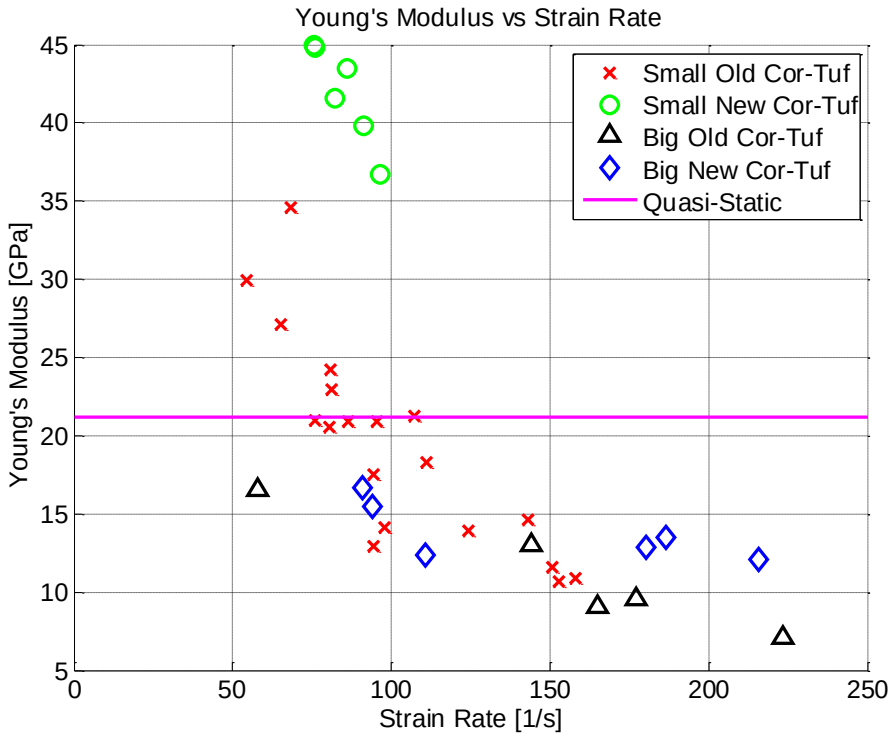

Figure 4-12 Young's Modulus vs Strain Rate

Figure 4-12 shows the Young's modulus vs. strain rate. All sizes of Cor-Tuf, Young's modulus decreases as strain rate was increased. For small Cor-Tuf, the Young's modulus drops more significantly as strain rate was increased when compared to the big Cor-Tuf.

The reason for the reduction in Young's modulus as strain rate was increased may be the variability in the number of preexisting flaws in the specimens. The compressive strength and critical strain decreases as strain rate increases due to the scatter in the distribution of flaws. Since the slope of stress strain curve is the Young's modulus, as the strain increases and compressive strength decreases the Young's Modulus also decreases as strain rate increases.

CHAPTER 5. CONCLUSIONS

Different sizes of Kolsky bars were utilized to characterize the dynamic behavior of differently sized Cor-Tuf specimens under uniaxial compressive stress loading. To ensure that the specimen deformed at a constant strain rate as well as achieving stress equilibrium, a pulse shaper was used. A circular annealed copper pulse shaper was used in small Kolsky Bars. To avoid the negative effects of radial inertia, annulus pulse shapers were used in big Kolsky bar. By utilizing the high speed camera it was concluded that the small Cor-Tuf failed in axial splitting failure mode as shown in Figure A-65 and Figure A-70. On the other hand, the big Cor-Tuf failed in combined axial splitting and shear mode due to the radial inertia that acted as a confinement as shown in Figure A-116 and Figure A-121. For small Cor-Tuf, the compressive strength decreased as strain rate increased, this is different from what has been observed by others, this might due to the variability in strength of Cor-Tuf specimens. The reduction of compressive strength as strain rate increases was due to the intrinsic behavior of Cor-Tuf instead of the strain rate effects. On the other hand, the compressive strength of big Cor-Tuf was observed to be rate independent. This might due to the fact that the amount of flaws was almost the same for all the big Cor-Tuf specimens. The critical strain and critical energy absorption per unit volume were observed to increase as strain rate was

increased. The Young's modulus showed a decline as critical strain increases due to the decrease in compressive strength and increase in critical strain with increasing strain rate. The reason for the reduction in Young's modulus as strain rate was increased may be the variability in the number of preexisting flaws in the specimens. Similarly, the reduction in Young's modulus as strain rate increases was also due to the intrinsic behavior of Cor-Tuf instead of the strain rate effects.

Also comparing the stress strain curves of big and small Cor-Tuf , prominent post-peak ductility was observed in the big Cor-Tuf, which is due to the radial inertia that acts as a confinement. Therefore, if the diameter of the Cor-Tuf was increased futher, it is possible that the stress-strain curve will tend towards the stress-strain curves exhibited by ductile materials. It will be interesting to investigate the limiting diameter for brittle to ductile failure mode shift.

LIST OF REFERENCES

LIST OF REFERENCES

1. Bischoff, P. and S. Perry, *Impact Behavior of Plain Concrete Loaded in Uniaxial Compression.* Journal of Engineering Mechanics, 1995. **121**(6): p. 685-693.

2. Bischoff, P.H. and S.H. Perry, *Compressive behaviour of concrete at high strain rates.* Materials and Structures, 1991. **24**(6): p. 425-450.

3. Chen, W.W. and B. Song, *Split Hopkinson (Kolsky) Bar: Design, Testing and Applications*. 2010: Springer.

4. Christensen, R.J., S.R. Swanson, and W.S. Brown, *Split-hopkinson-bar tests on rock under confining pressure.* Experimental Mechanics, 1972. **12**(11): p. 508-513.

5. Davis, R.M., *A critical study of the Hopkinson pressure bar.* Proc. R. Soc. London, 1948(A240): p. 375-457.

6. Duffy, J., J.D. Campbell, and R.H. Hawley, *On the Use of a Torsional Split Hopkinson Bar to Study Rate Effects in 1100-0 Aluminum.* Journal of Applied Mechanics, 1971. **38**(1): p. 83-91.

7. Elfahal, M.M., et al., *Size effect for normal strength concrete cylinders subjected to axial impact.* International Journal of Impact Engineering, 2005. **31**(4): p. 461-481.

8. Ellwood, S., L.J. Griffiths, and D.J. Parry, *Materials testing at high constant strain rates.* Journal of Physics E: Scientific Instruments, 1982. **15**(3): p. 280.

9. Erin M. Williams, S.S.G., Paul A. Reed, Todd S. Rushing, *Laboratory Characterization of Cor-Tuf Concrete With and Without Steel Fibers.* 2009.

10. Frew, D.J., M.J. Forrestal, and W. Chen, *Pulse shaping techniques for testing brittle materials with a split hopkinson pressure bar.* Experimental Mechanics, 2002. **42**(1): p. 93-106.

11. Frew, D.J., M.J. Forrestal, and W. Chen, *Pulse shaping techniques for testing elastic-plastic materials with a split Hopkinson pressure bar.* Experimental Mechanics, 2005. **45**(2): p. 186-195.

12. Hopkinson, B., *A Method of Measuring the Pressure Produced in the Detonation of High Explosives or by the Impact of Bullets.* Proceedings of the Royal Society of London. Series A, Containing Papers of a Mathematical and Physical Character, 1914. **89**(612): p. 411-413.

13. Huang Hsing Pan, J.-P.P., Yuh-Shiou Tai, and Chao-Shun Chang, *Static-Dynamic Properties of Reactive Powder Concrete with Blast Furnace Slag.* Applied Mechanics and Materials, 2011. **82**(July, 2011): p. 100-105.

14. Jiao, C., et al., *Behavior of steel fiber-reinforced high-strength concrete at medium strain rate.* Frontiers of Architecture and Civil Engineering in China, 2009. **3**(2): p. 131-136.

15. Ju, Y., et al., *Experimental study of dynamic mechanical properties of reactive powder concrete under high-strain-rate impacts.* Science China Technological Sciences, 2010. **53**(9): p. 2435-2449.

16. Kolsky, H., *An Investigation of the Mechanical Properties of Materials at very High Rates of Loading.* Proceedings of the Physical Society. Section B, 1949. **62**(11): p. 676.

17. Lok, T. and P. Zhao, *Impact Response of Steel Fiber-Reinforced Concrete Using a Split Hopkinson Pressure Bar.* Journal of Materials in Civil Engineering, 2004. **16**(1): p. 54-59.

18. Richard, P. and M. Cheyrezy, *Composition of reactive powder concretes.* Cement and Concrete Research, 1995. **25**(7): p. 1501-1511.

19. Ross CA, J.D., Tedesco JW, Huges ML, *Moisture and strain rate effects on concrete strength.* ACI Material Journal, 1996.

20. Shah, S.P. and S.H. Ahmad, *High Performance Concrete: Properties and Applications*. 1994: McGraw-Hill Ryerson, Limited.

21. Shkolnik, I.E., *Influence of high strain rates on stress–strain relationship, strength and elastic modulus of concrete.* Cement and Concrete Composites, 2008. **30**(10): p. 1000-1012.

22. Song, B., et al., *Radial Inertia Effects in Kolsky Bar Testing of Extra-soft Specimens.* Experimental Mechanics, 2007. **47**(5): p. 659-670.

23. Tai, Y.S., *Flat ended projectile penetrating ultra-high strength concrete plate target.* Theoretical and Applied Fracture Mechanics, 2009. **51**(2): p. 117-128.

24. Tai, Y.S., *Uniaxial compression tests at various loading rates for reactive powder concrete.* Theoretical and Applied Fracture Mechanics, 2009. **52**(1): p. 14-21.

25. Tang, T., L. Malvern, and D. Jenkins, *Rate Effects in Uniaxial Dynamic Compression of Concrete.* Journal of Engineering Mechanics, 1992. **118**(1): p. 108-124.

26. Tedesco, J.W. and C.A. Ross, *Strain-rate-dependent constitutive equations for concrete.* Journal Name: Journal of Pressure Vessel Technology; Journal Volume: 120; Journal Issue: 4; Other Information: DN: Paper presented at the pressure vessels and piping conference, July 27--31, 1997, Orlando, FL (US); PBD: Nov 1998, 1998: p. Medium: X; Size: pp. 398-405.

27. WANG, S., et al., *Effect of high strain rate loading on compressive behaviour of fibre-reinforced high-strength concrete*. Vol. 63. 2011, London, ROYAUME-UNI: Telford. 15.

28. Wang, S., M.-H. Zhang, and S.T. Quek, *Mechanical behavior of fiber-reinforced high-strength concrete subjected to high strain-rate compressive loading.* Construction and Building Materials, 2012. **31**(0): p. 1-11.

29. Wang, Y., et al., *Experimental and numerical studies on dynamic compressive behavior of reactive powder concretes.* Acta Mechanica Solida Sinica, 2008. **21**(5): p. 420-430.

30. Wanpeng Wang , Y.H., Xintao Ren, Yibo Xiong,Kang zhao, Xiao She, *Impact Experimental Study for Dynamic Character of Reactive Powder Concrete.* Advanced Materials Research, 2011: p. 187-191.

31. Warren, T.L. and M.J. Forrestal, *Comments on the Effect of Radial Inertia in the Kolsky Bar Test for an Incompressible Material.* Experimental Mechanics, 2010. **50**(8): p. 1253-1255.

32. Xiao, S., H. Li, and G. Lin *Dynamic behaviour and constitutive model of concrete at different strain rates*. Magazine of Concrete Research, 2008. **60**, 271-278.

33. Yi, N.-H., et al., *Blast-resistant characteristics of ultra-high strength concrete and reactive powder concrete.* Construction and Building Materials, 2012. **28**(1): p. 694-707.

34. Yunsheng, Z., et al., *Preparation of C200 green reactive powder concrete and its static–dynamic behaviors.* Cement and Concrete Composites, 2008. **30**(9): p. 831-838.

APPENDIX

APPENDIX

A1: Dynamic Uniaxial Compressive Experiments on Small Old Cor-Tuf

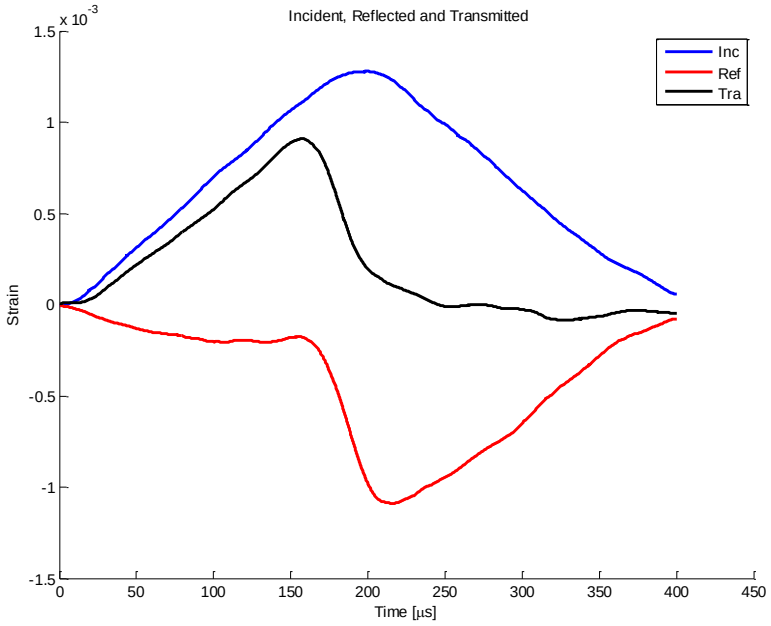

Figure A-1 Experiment 1 Incident, Reflected and Transmitted Pulse

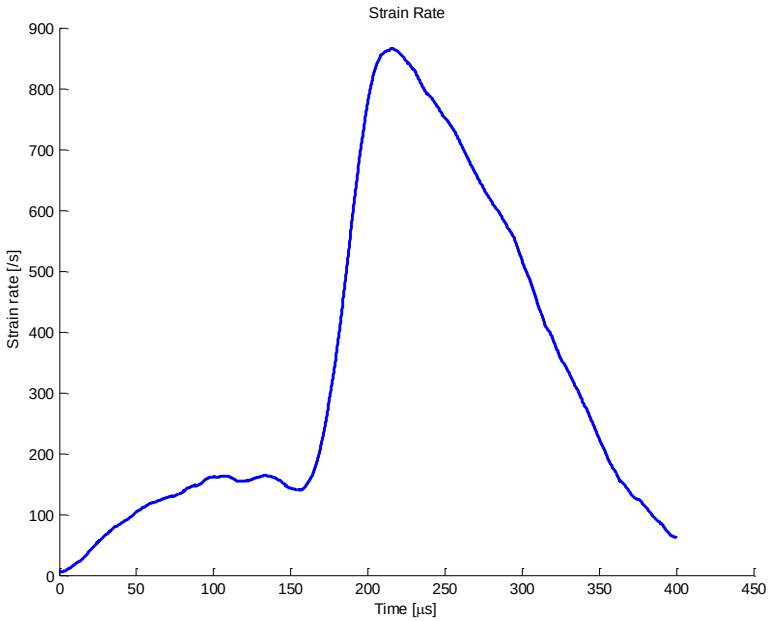

Figure A-2 Experiment 1 Strain Rate History

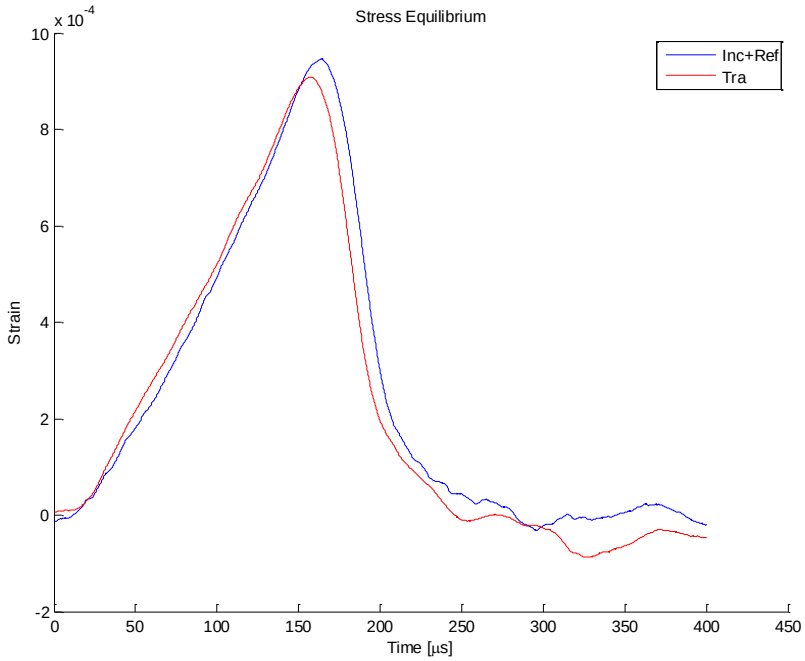

Figure A-3 Experiment 1 Stress Equilibrium

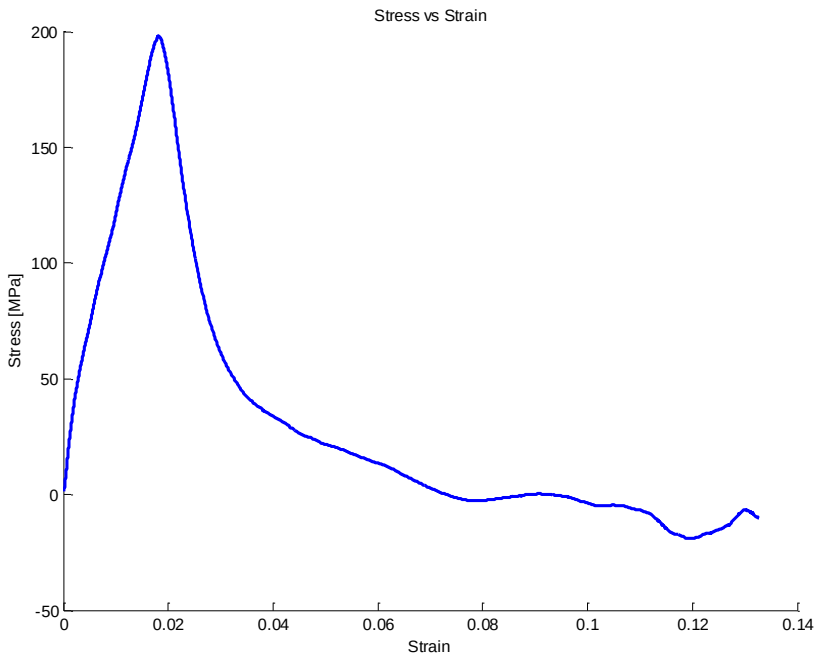

Figure A-4 Experiment 1 Stress Strain Curve

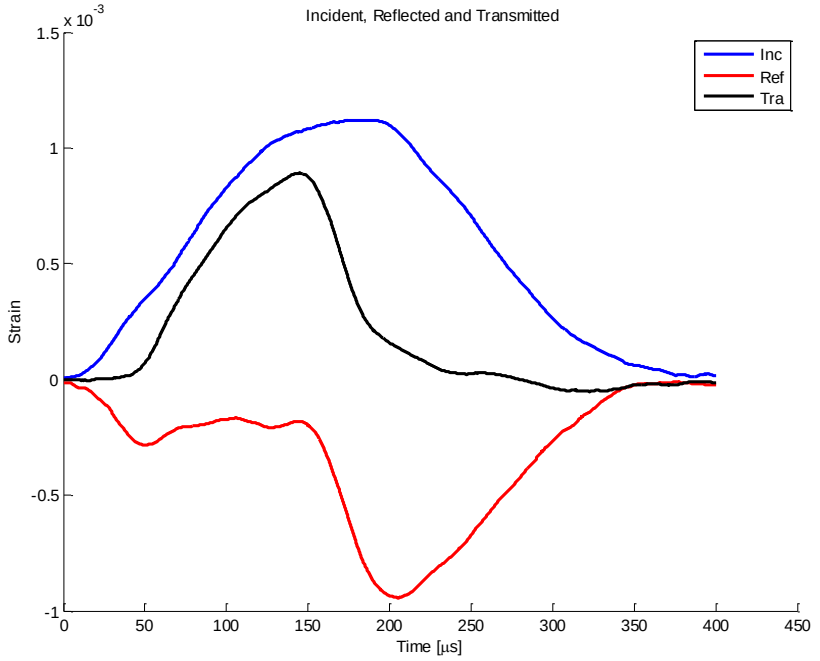

Figure A-5 Experiment 2 Incident Reflected and Transmitted Pulse

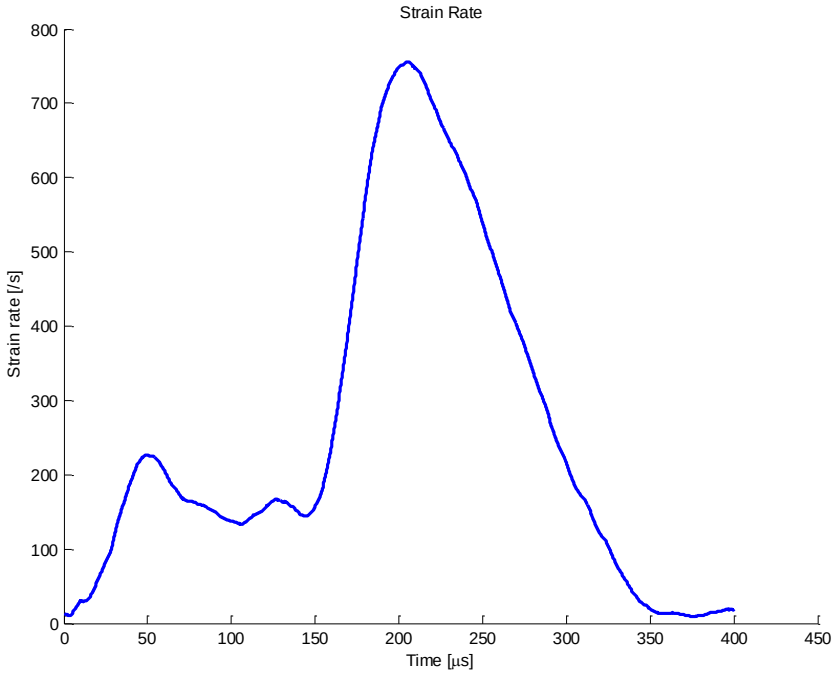

Figure A-6 Experiment 2 Strain Rate History

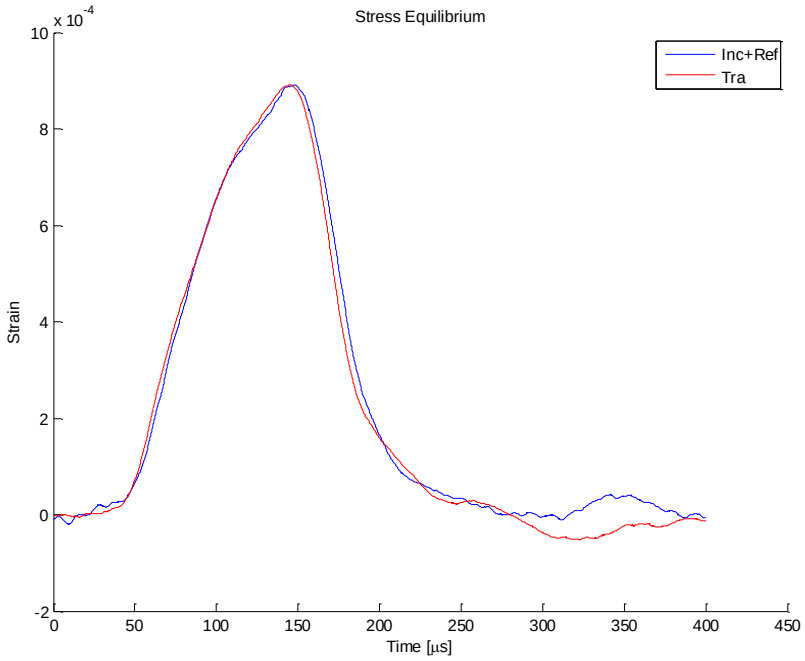

Figure A-7 Experiment 2 Stress Equilibrium

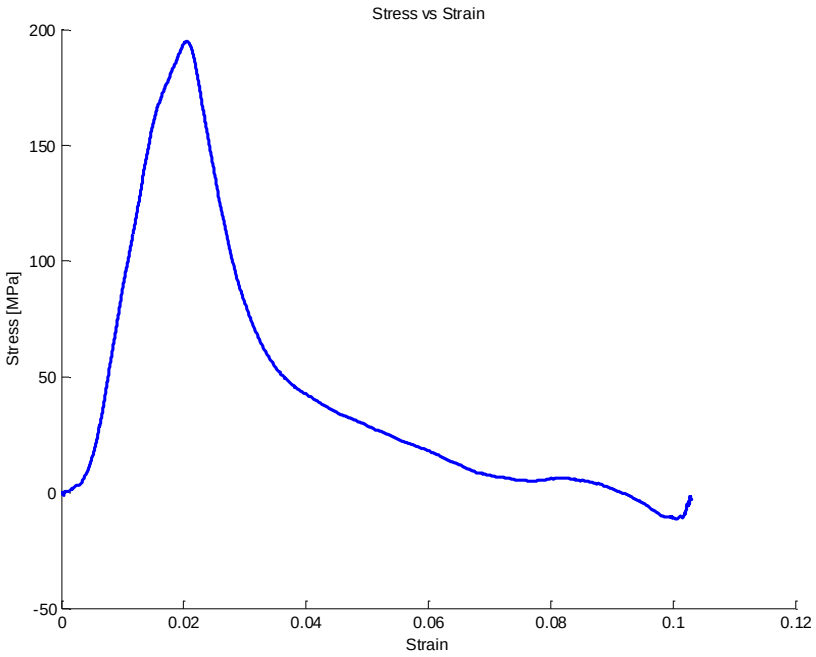

Figure A-8 Experiment 2 Stress Strain Curve

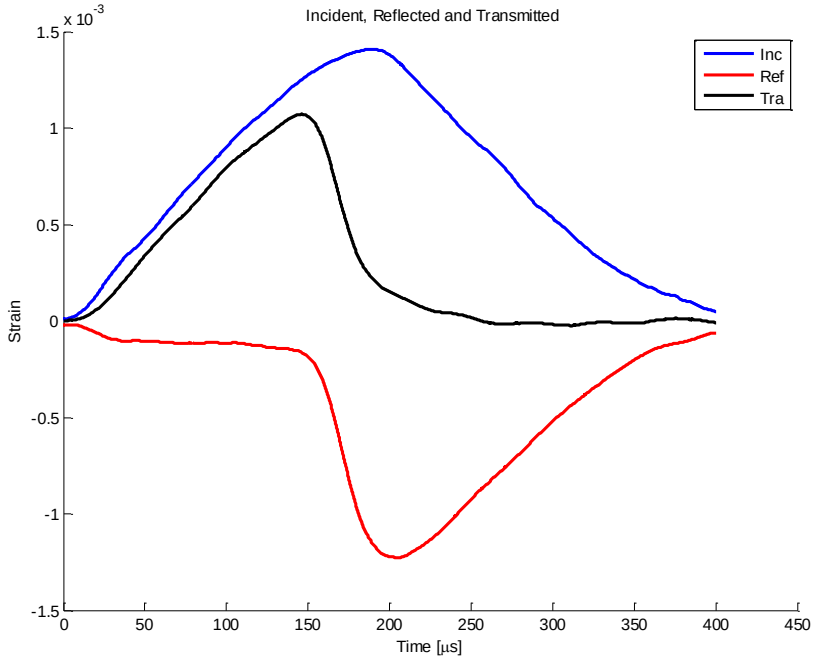

Figure A-9 Experiment 3 Incident Reflected and Transmitted Pulse

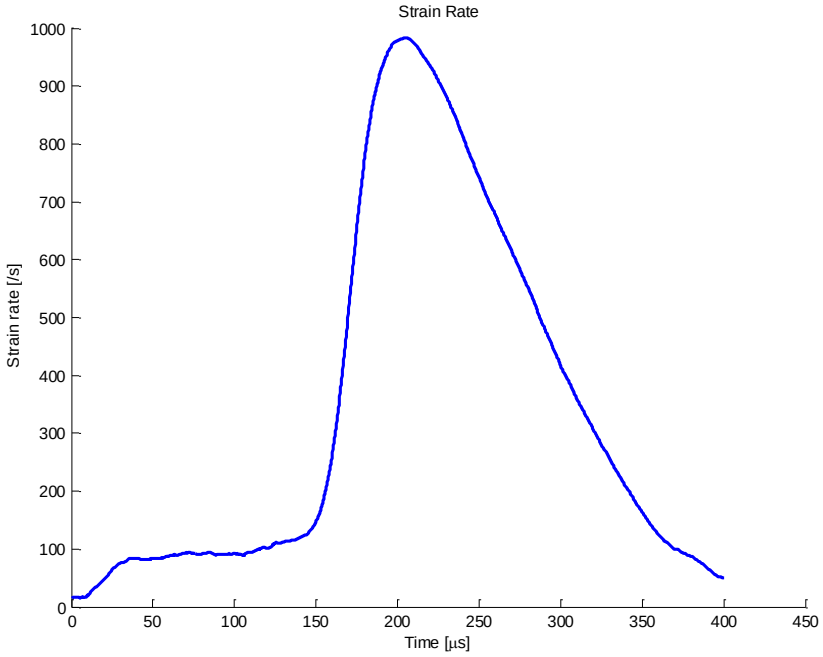

Figure A-10 Experiment 3 Strain Rate History

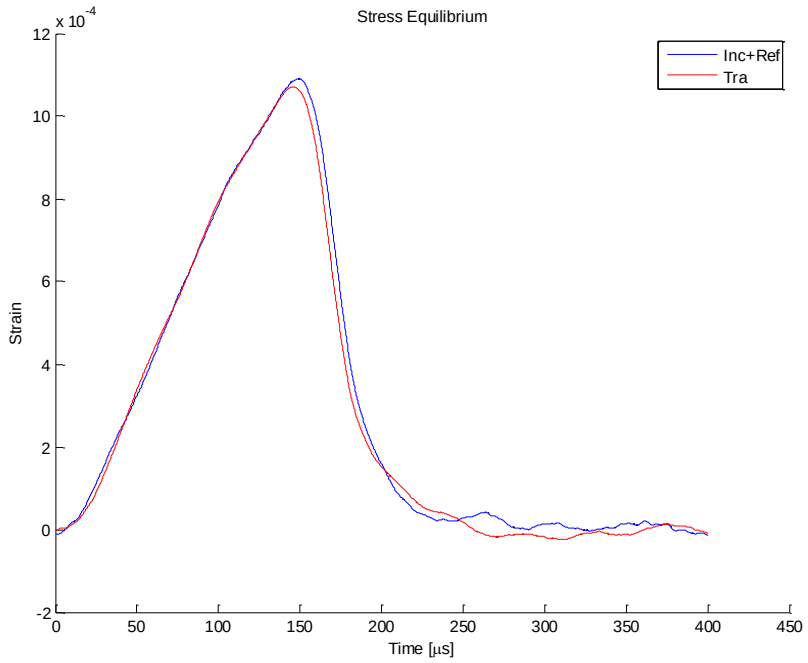

Figure A-11 Experiment 3 Stress Equlibrium

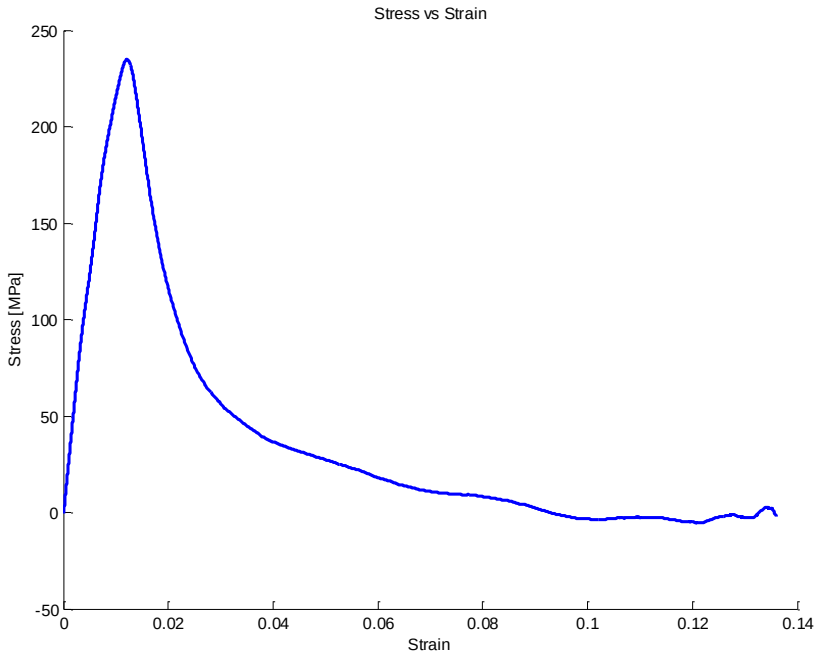

Figure A-12 Experiment 3 Stress Strain Curve

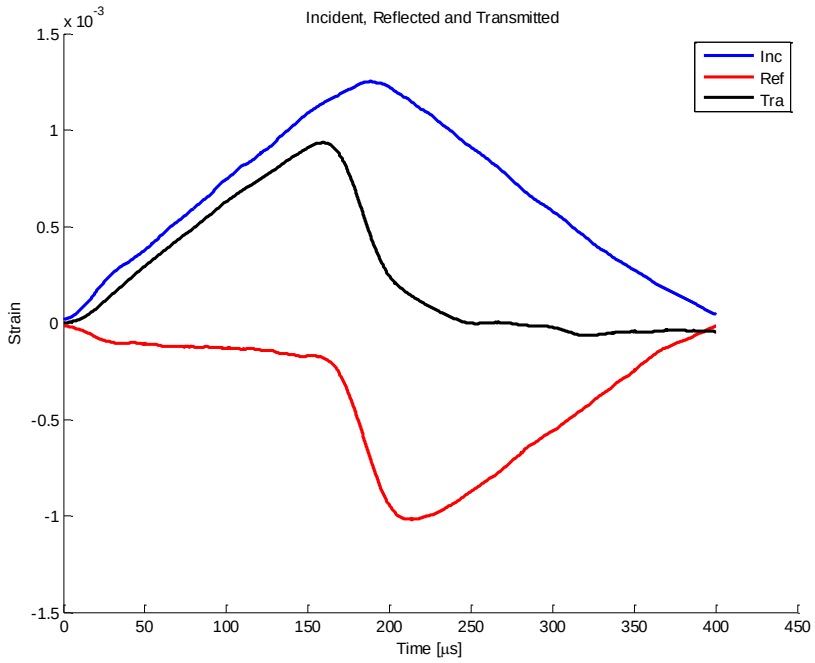

Figure A-13 Experiment 4 Incident Reflected and Transmitted Pulse

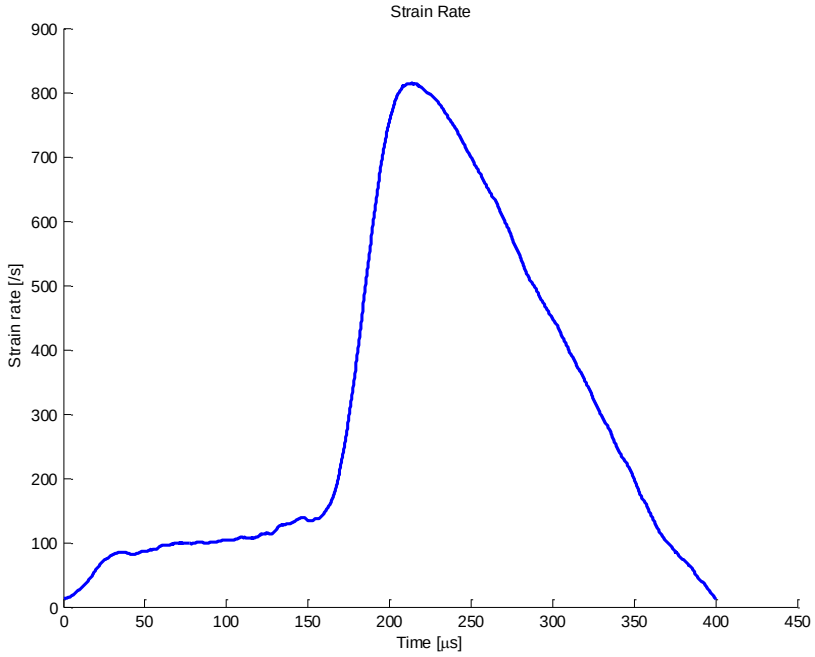

Figure A-14 Experiment 4 Strain Rate History

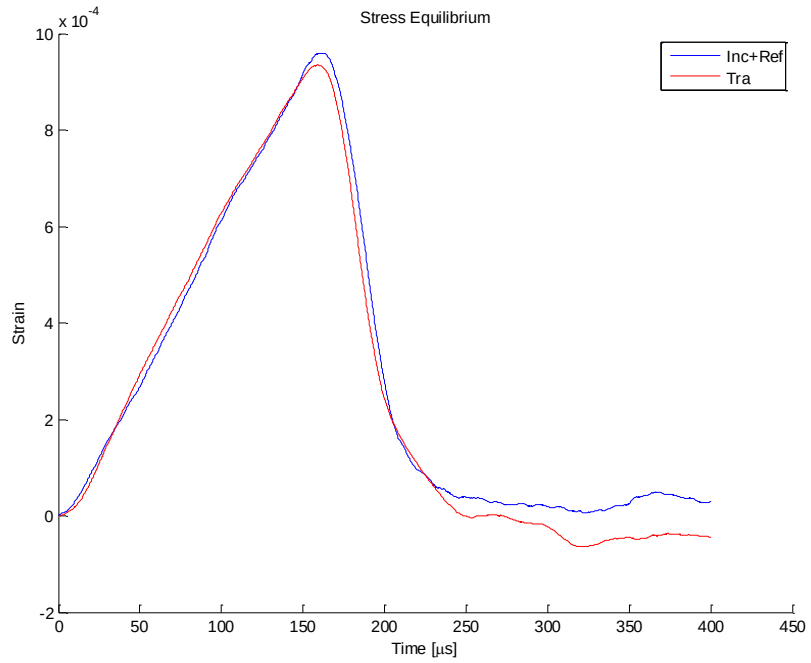

Figure A-15 Experiment 4 Stress Equilibrium

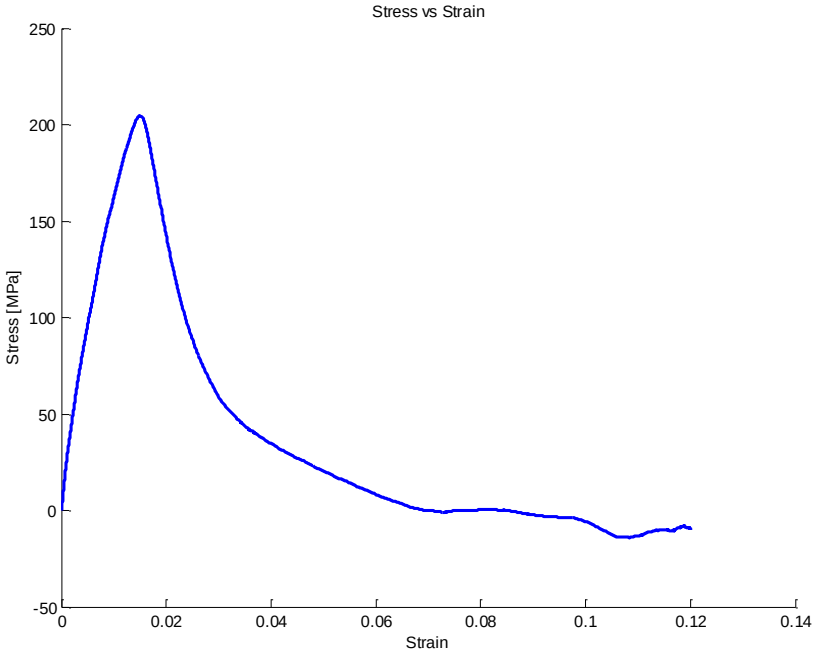

Figure A-16 Experiment 4 Stress Strain Curve

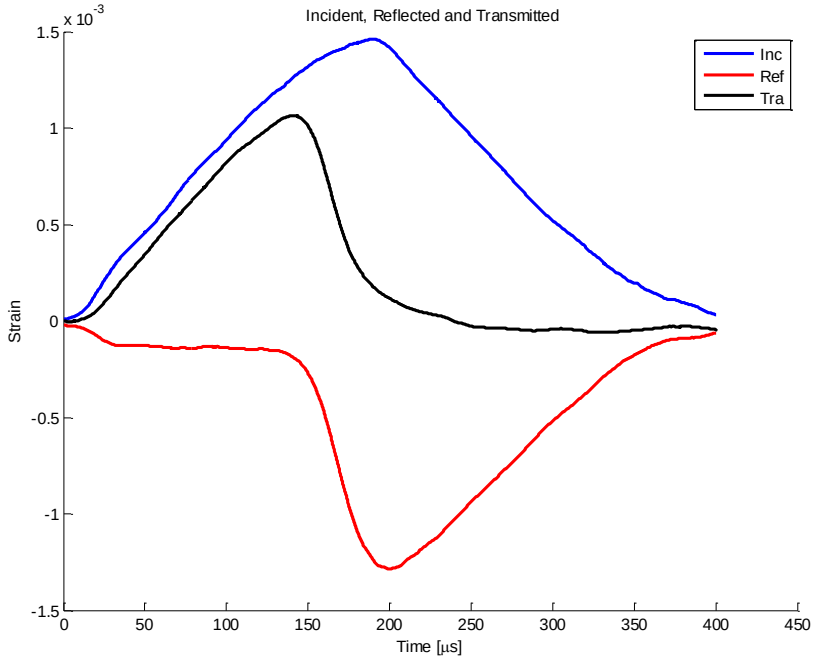

Figure A-17 Experiment 5 Incident Reflected and Transmitted Pulse

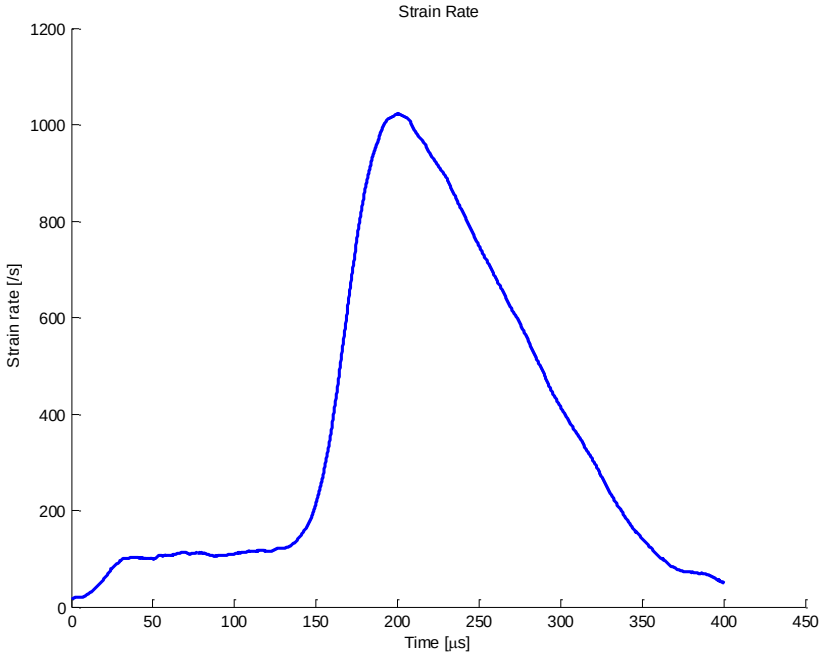

Figure A-18 Experiment 5 Strain Rate History

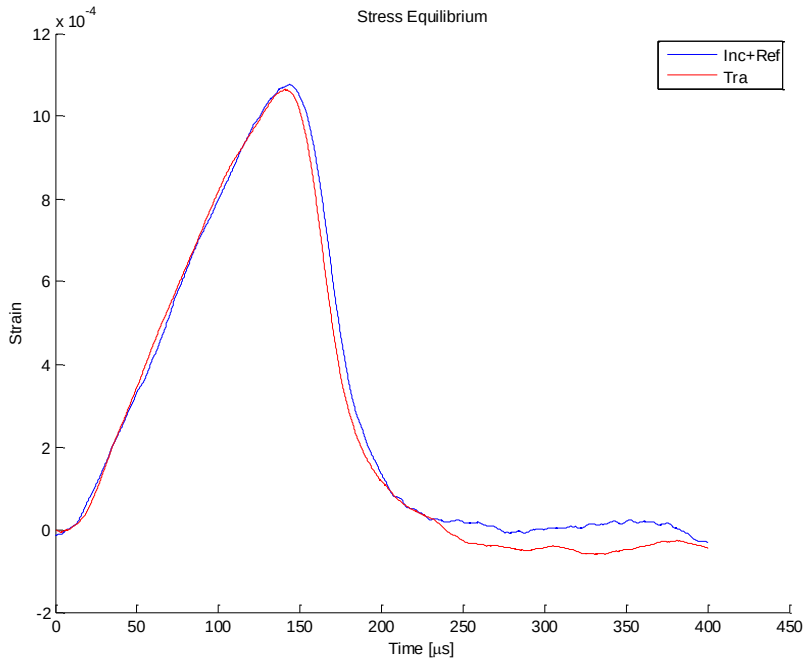

Figure A-19 Experiment 5 Stress Equilibrium

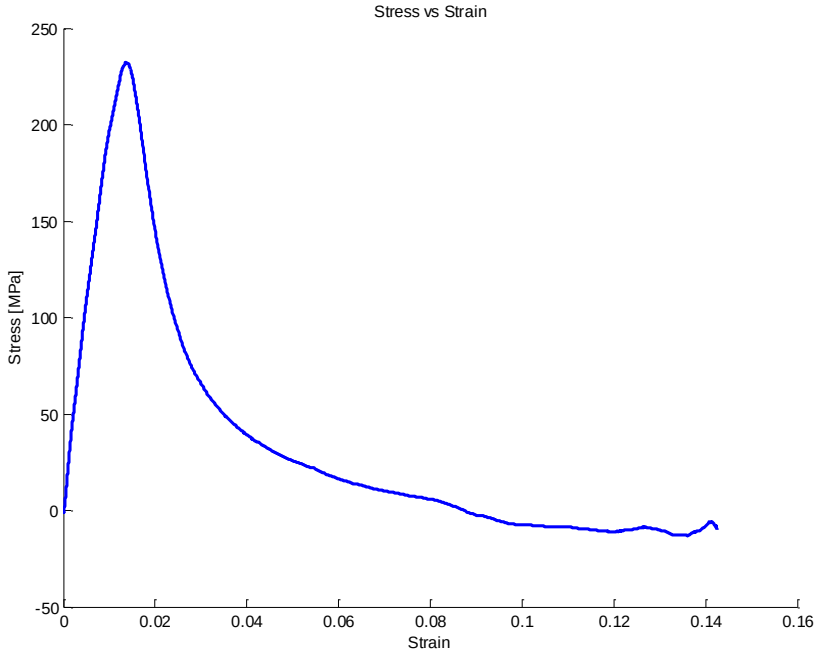

Figure A-20 Experiment 5 Stress Strain Curve

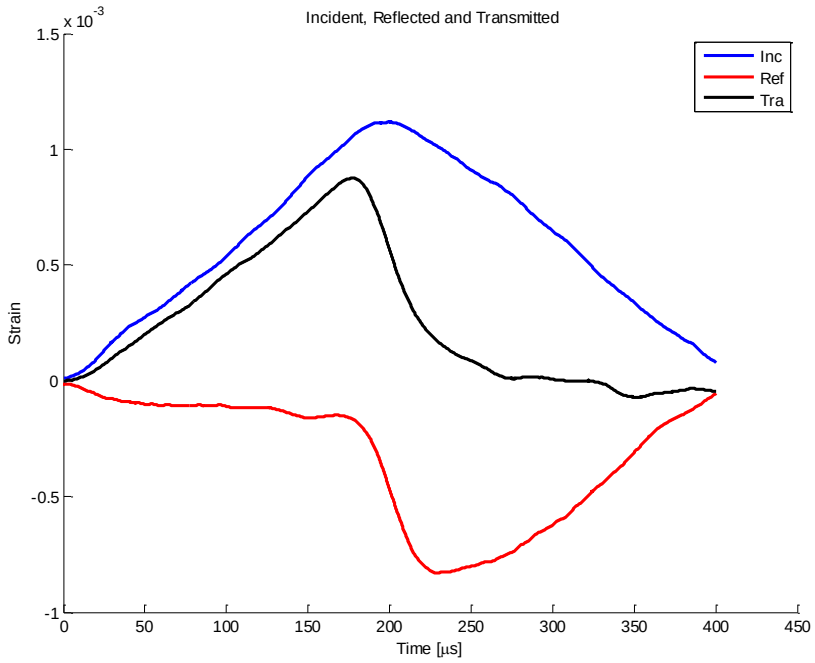

Figure A-21 Experiment 6 Incident Reflected and Transmitted Pulse

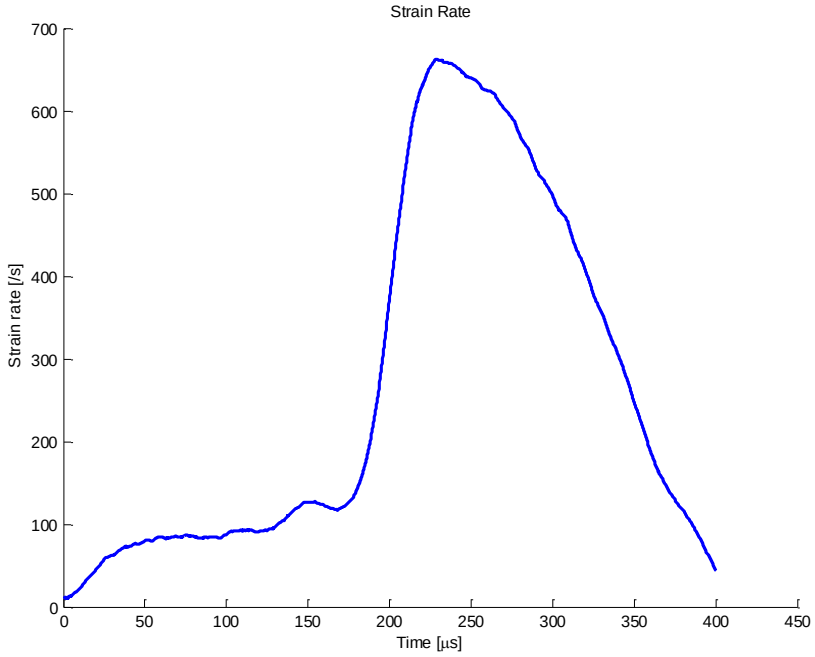

Figure A-22 Experiment 6 Strain Rate History

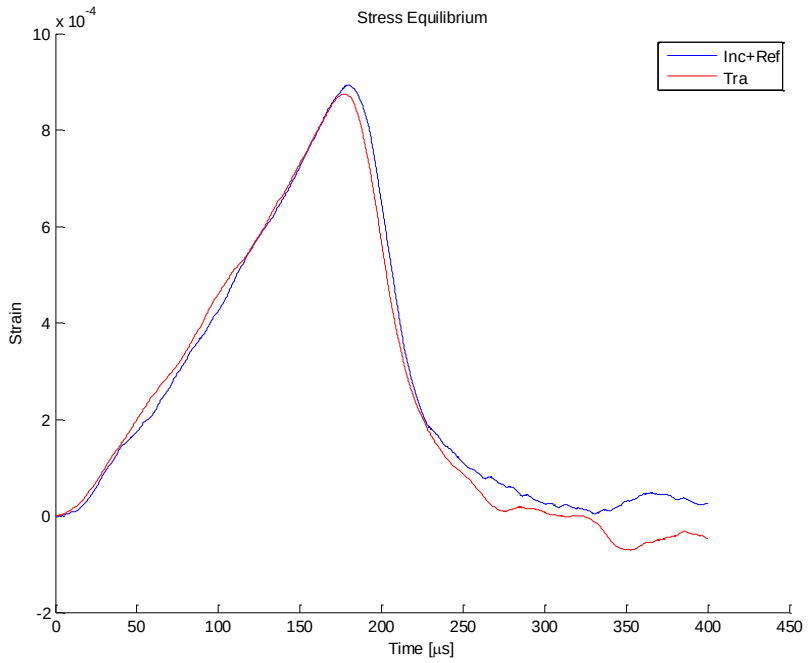

Figure A-23 Experiment 6 Stress Equilibrium

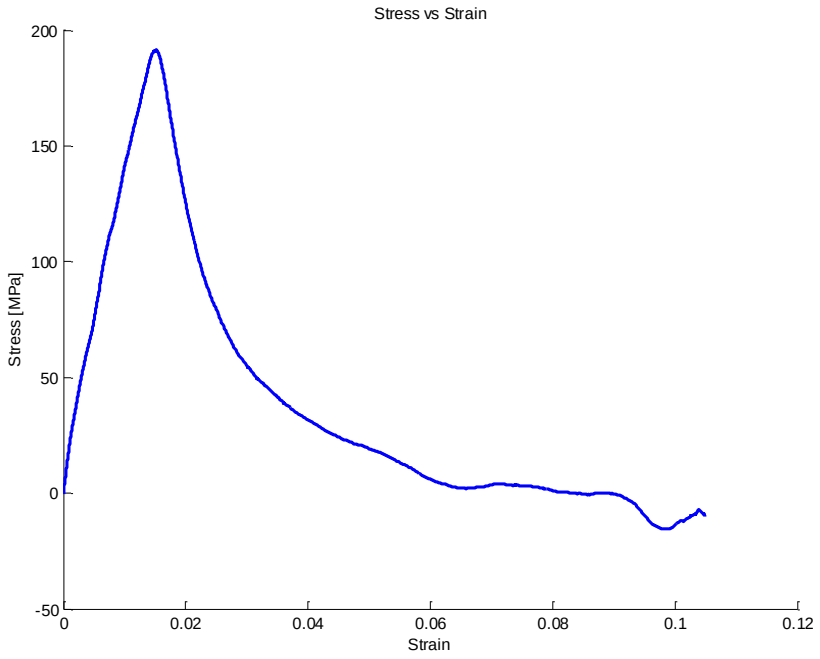

Figure A-24 Experiment 6 Stress Strain Curve

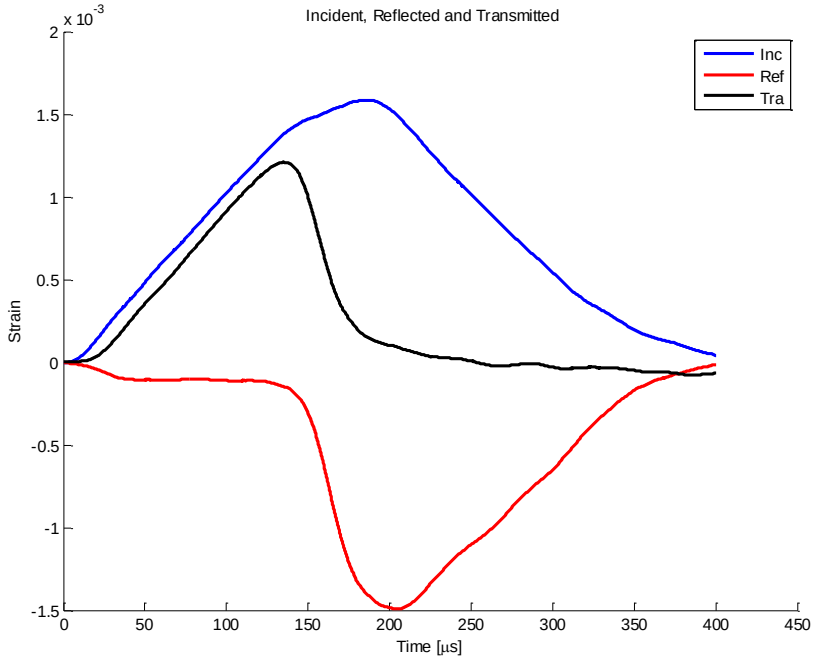

Figure A-25 Experiment 7 Incident Reflected and Transmitted Pulse

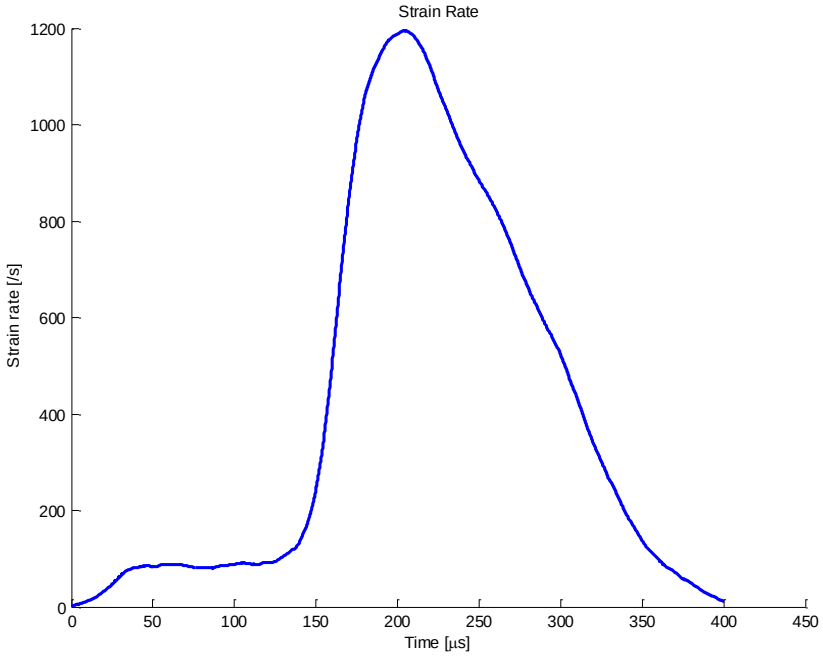

Figure A-26 Experiment 7 Strain Rate History

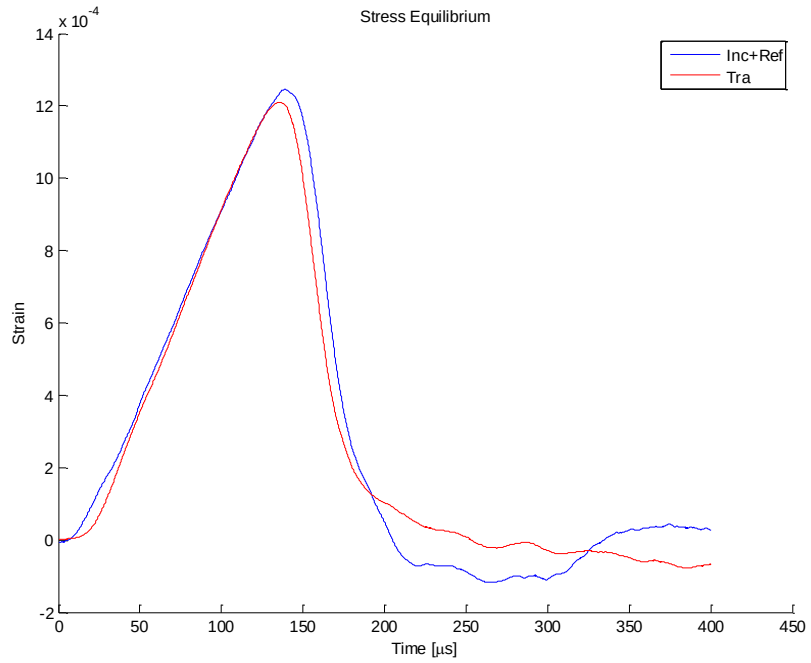

Figure A-27 Experiment 7 Stress Equilibrium

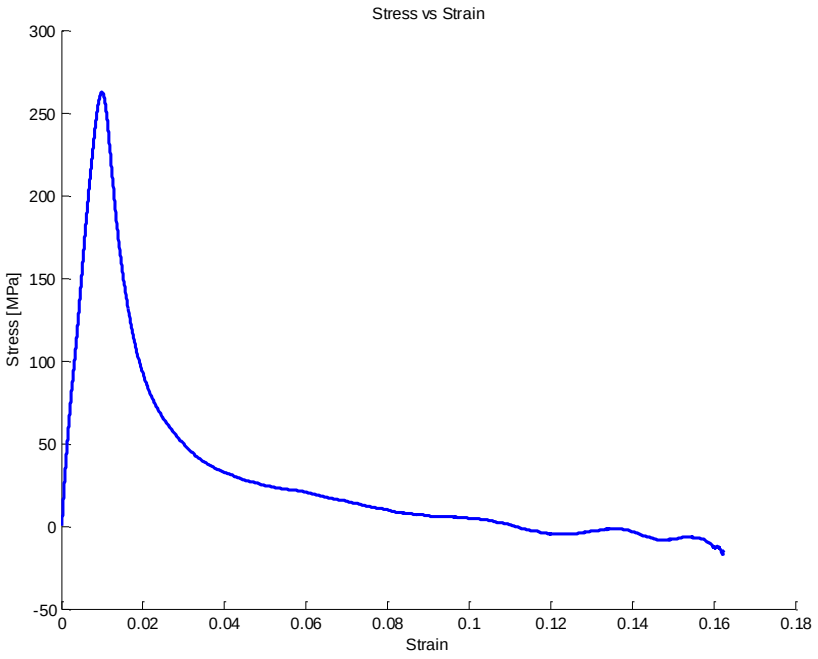

Figure A-28 Experiment 7 Stress Strain Curve

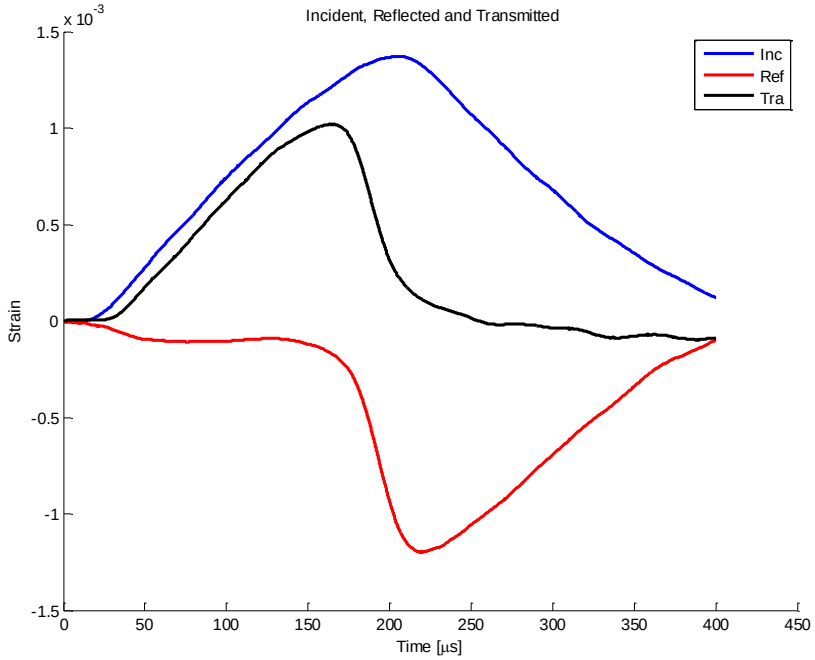

Figure A-29 Experiment 8 Incident Reflected and Transmitted Pulse

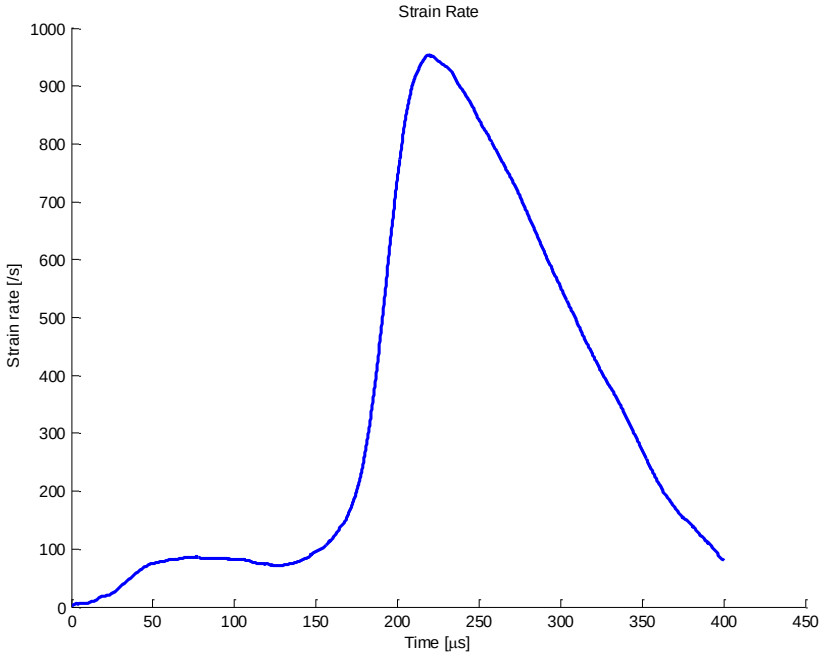

Figure A-30 Experiment 8 Strain Rate History

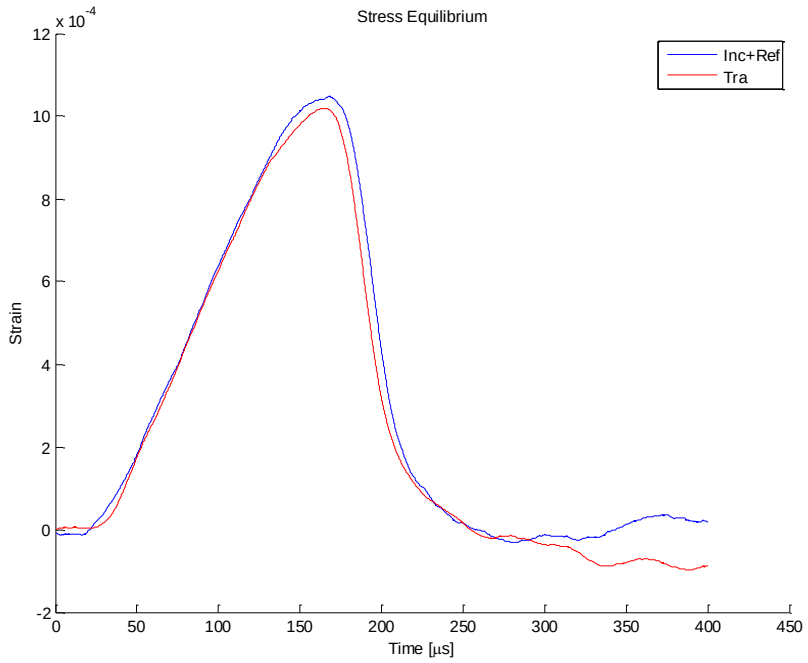

Figure A-31 Experiment 8 Stress Equilibrium

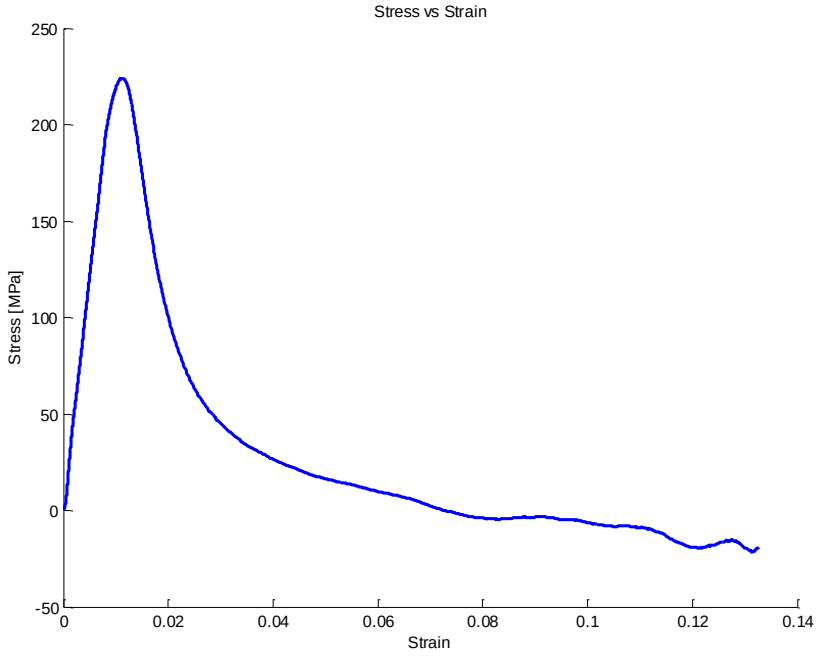

Figure A-32 Experiment 8 Stress Strain Curve

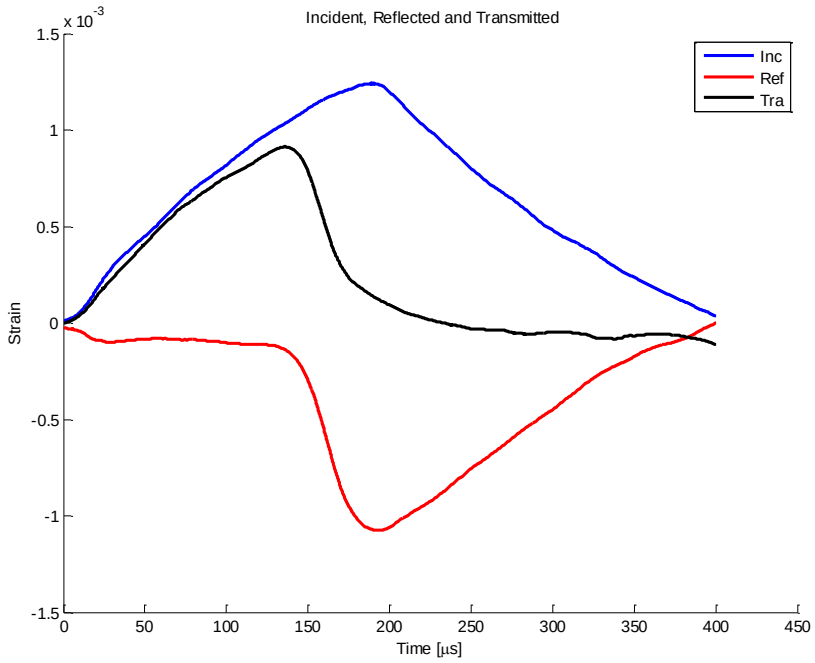

Figure A-33 Experiment 9 Incident Reflected and Transmitted Pulse

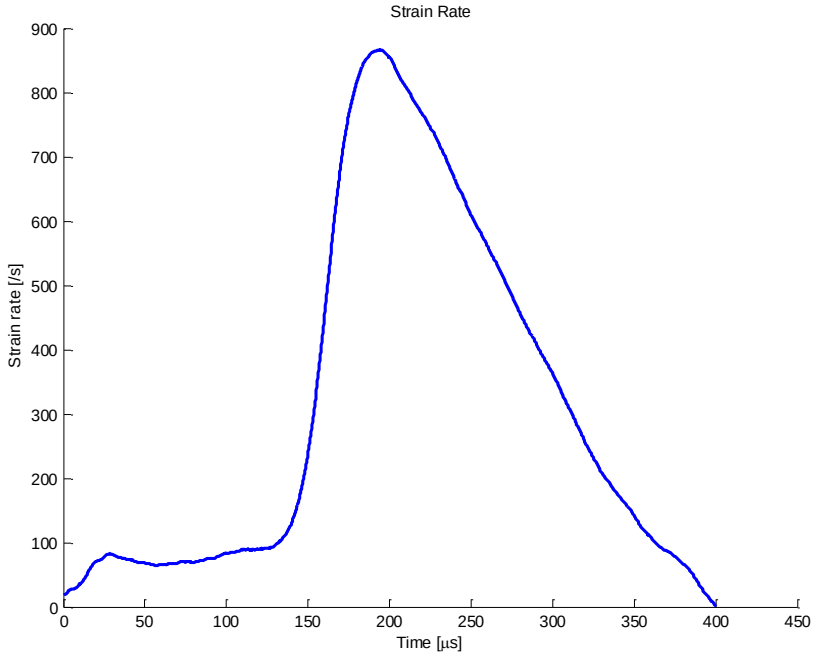

Figure A-34 Experiment 9 Strain Rate History

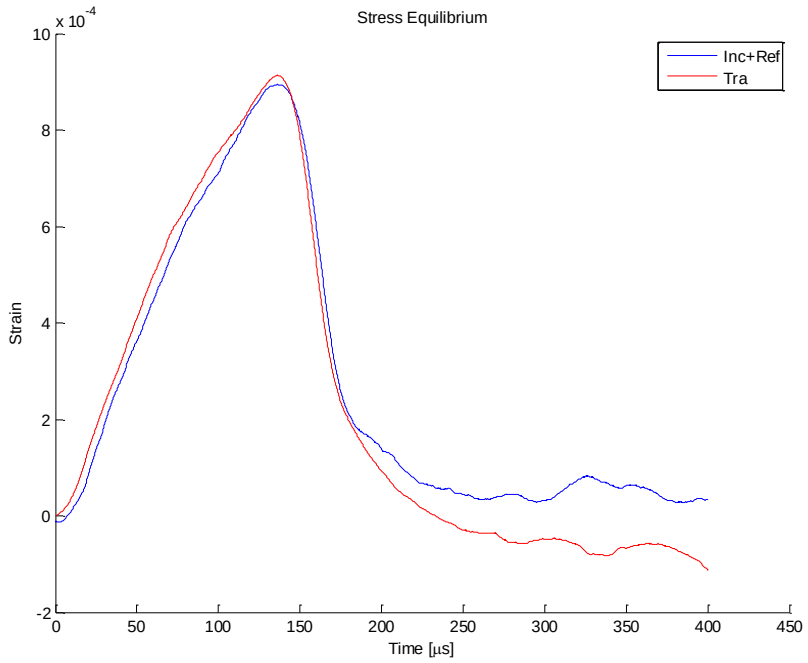

Figure A-35 Experiemnt 9 Stress Equilibrium

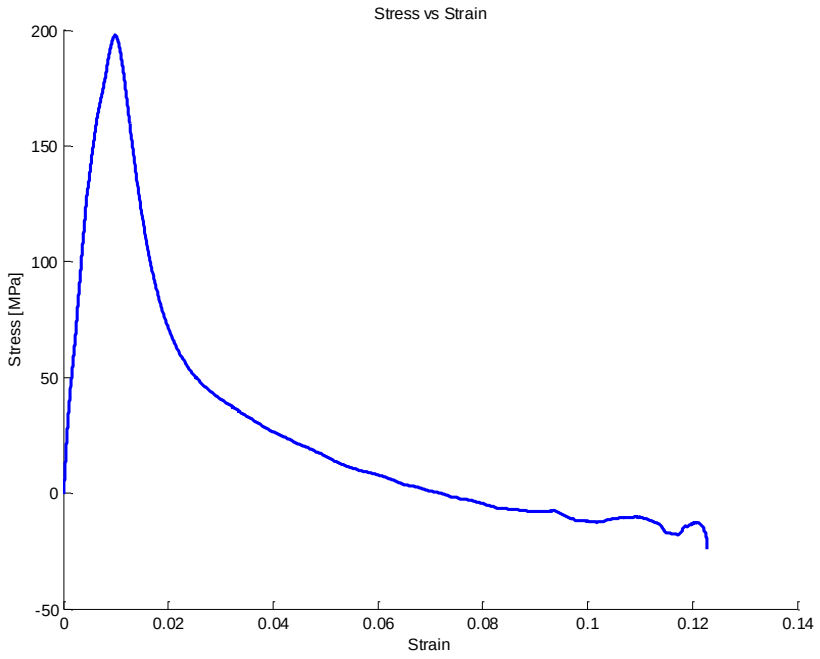

Figure A-36 Experiment 9 Stress Strain Curve

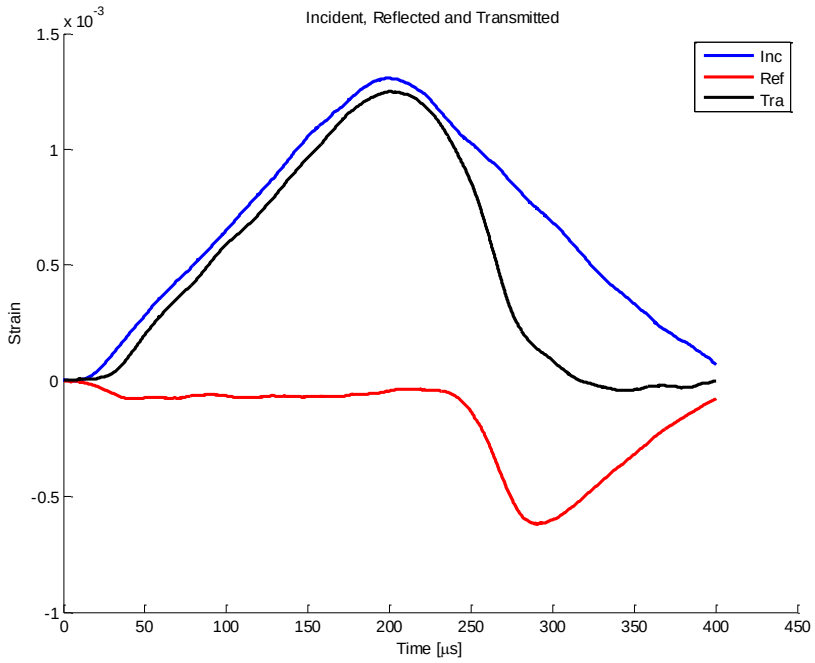

Figure A-37 Experiment 10 Incident Reflec ted and Transmitted Pulse

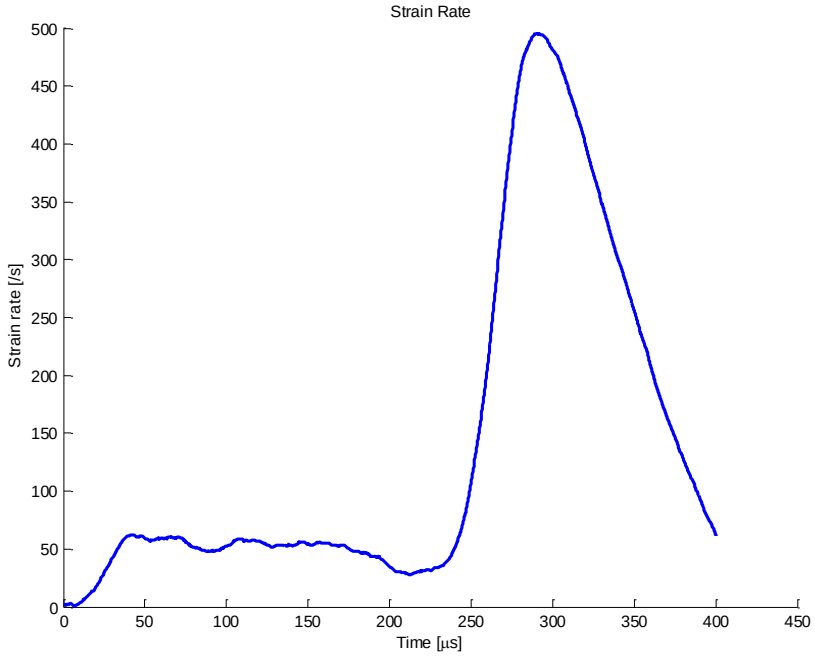

Figure A-38 Experiment 10 Strain Rate History

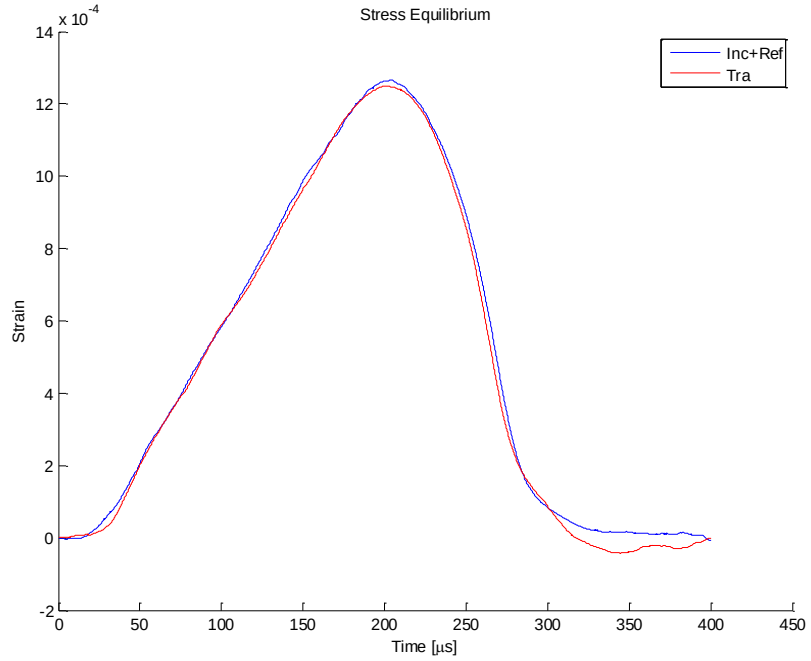

Figure A-39 Experiment 10 Stress Equilibrium

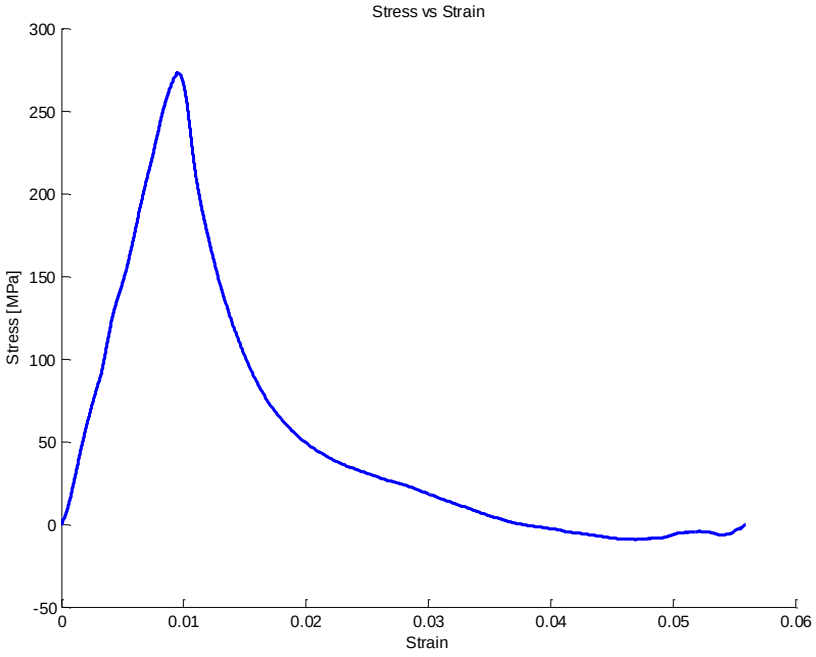

Figure A-40 Experiment 10 Stress Strain Curve

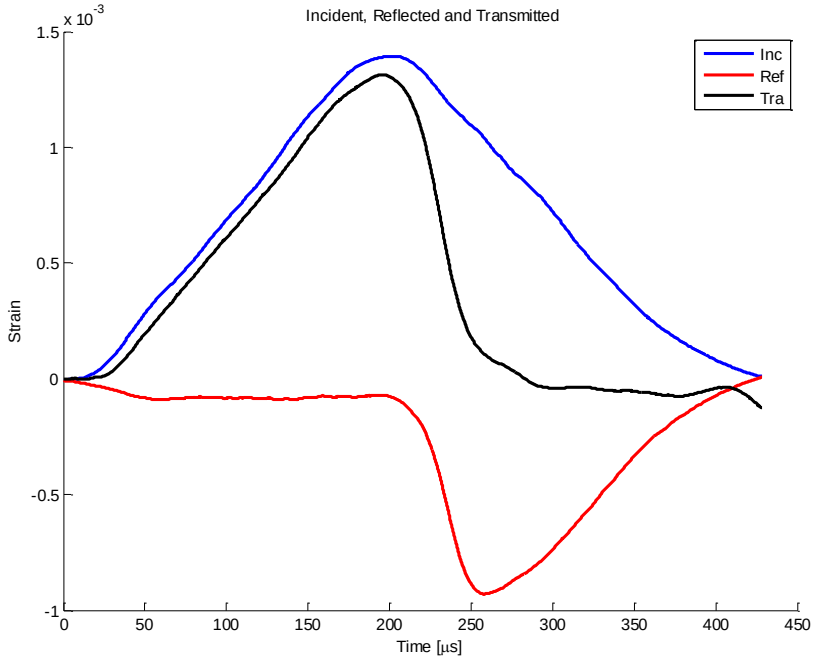

Figure A-41 Experiment 11 Incident Reflected and Transmitted Pulse

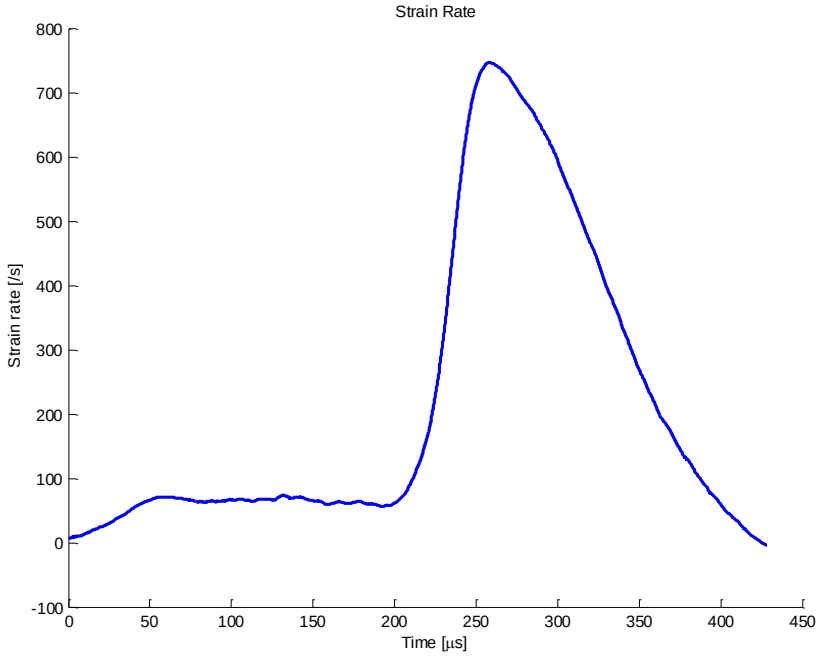

Figure A-42 Experiment 11 Strain Rate History

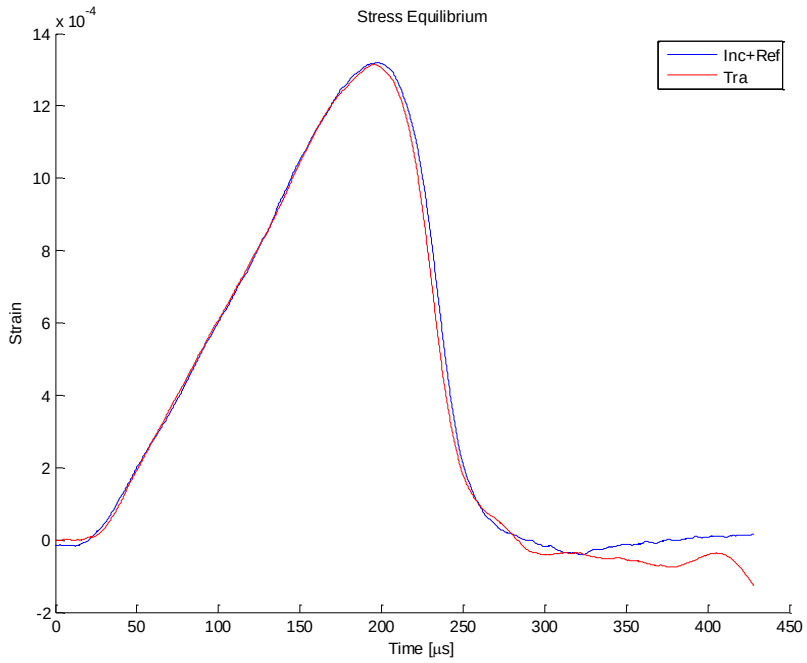

Figure A-43 Experiment 1 Stress Equilibrium

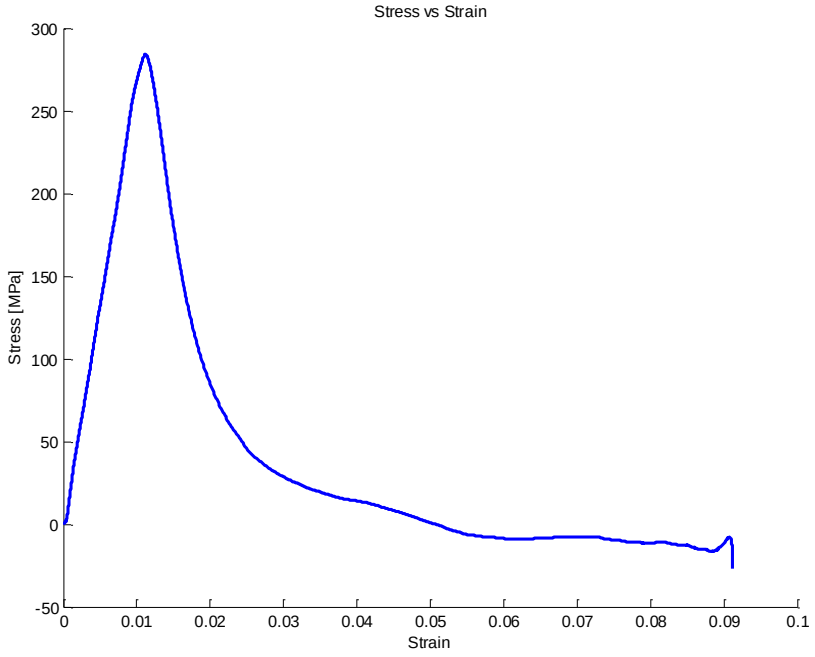

Figure A-44 Experiment 11 Stress Strain Curve

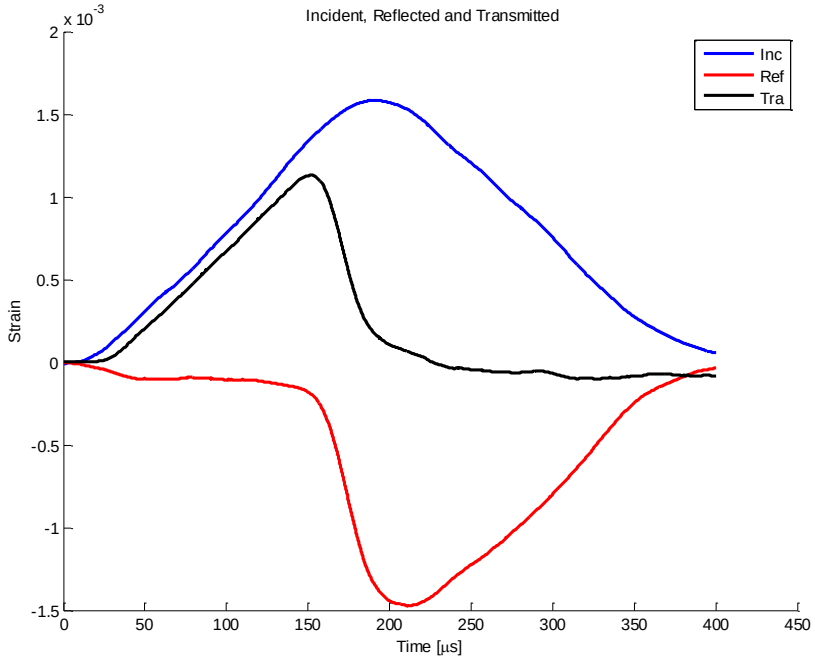

Figure A-45 Experiment 12 Incident Reflected and Transmitted Pulse

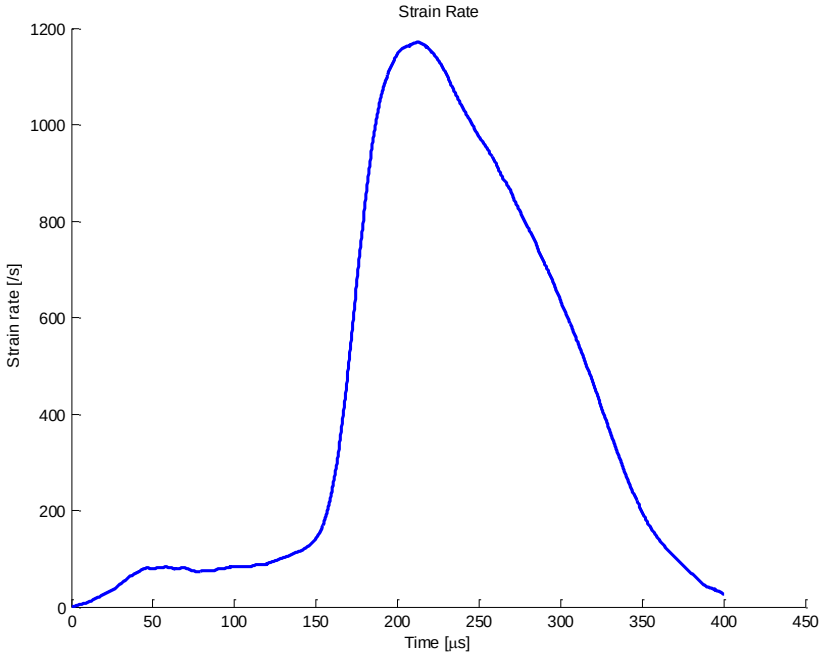

Figure A-46 Experiment 12 Strain Rate History

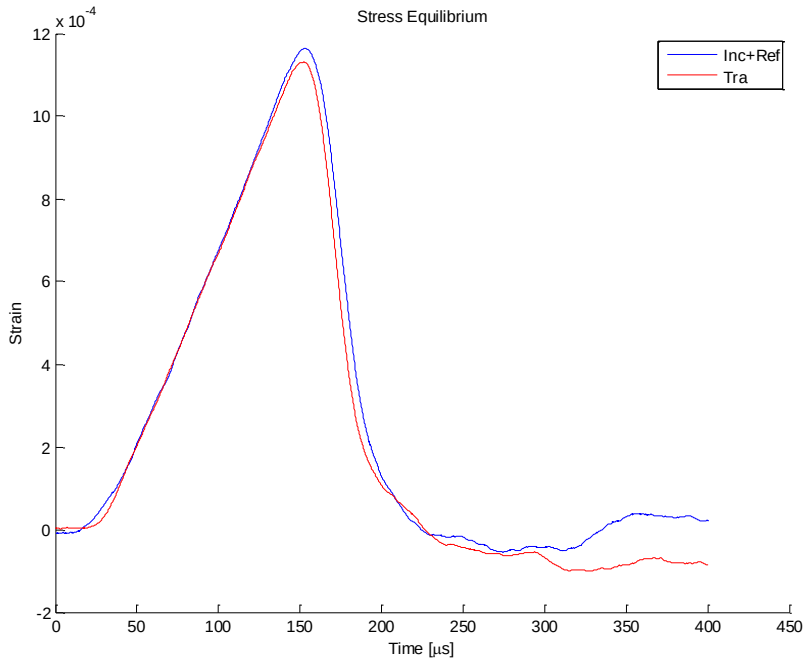

Figure A-47 Experiment 12 Stress Equlibrium

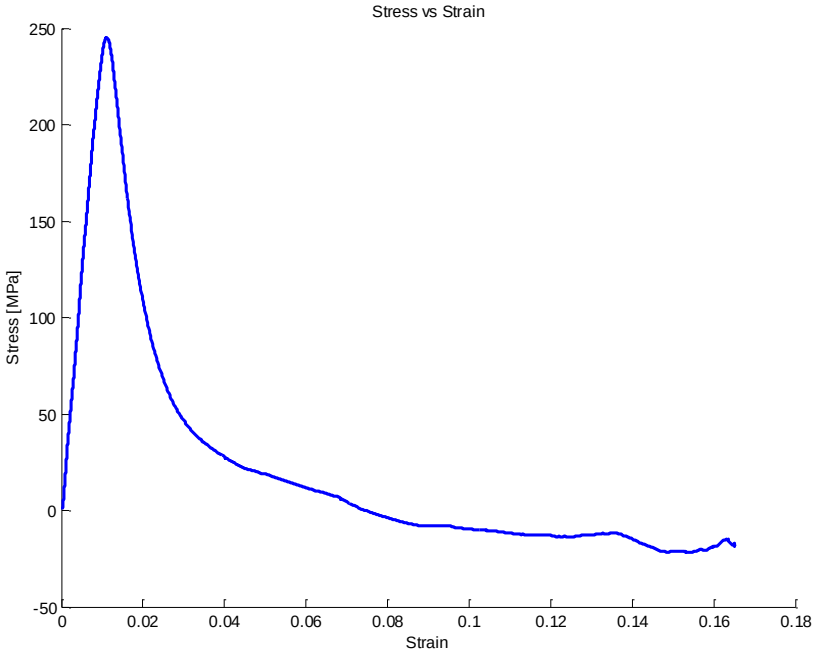

Figure A-48 Experiment 12 Stress Strain Curve

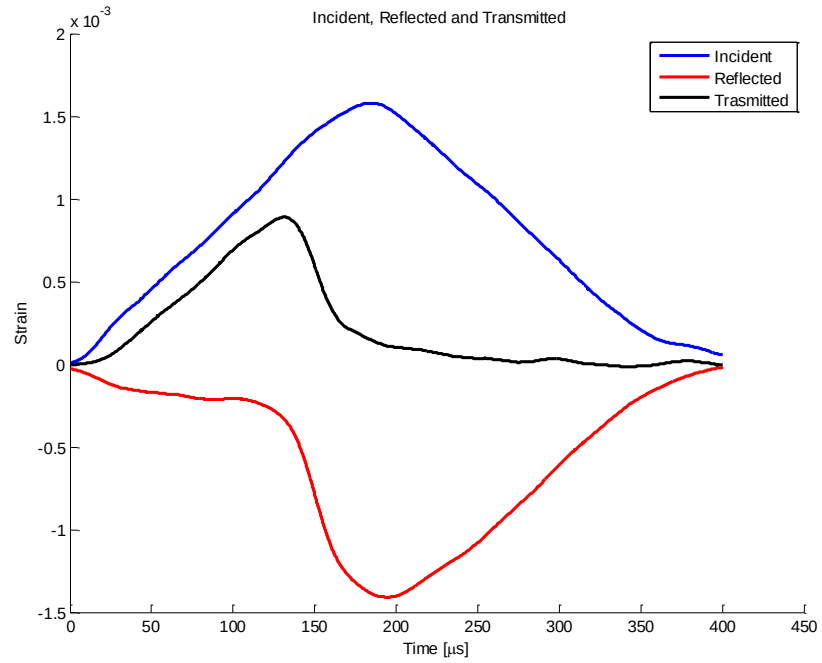

Figure A-49 Experiment 13 Incident Reflected and Transmitted Pulse

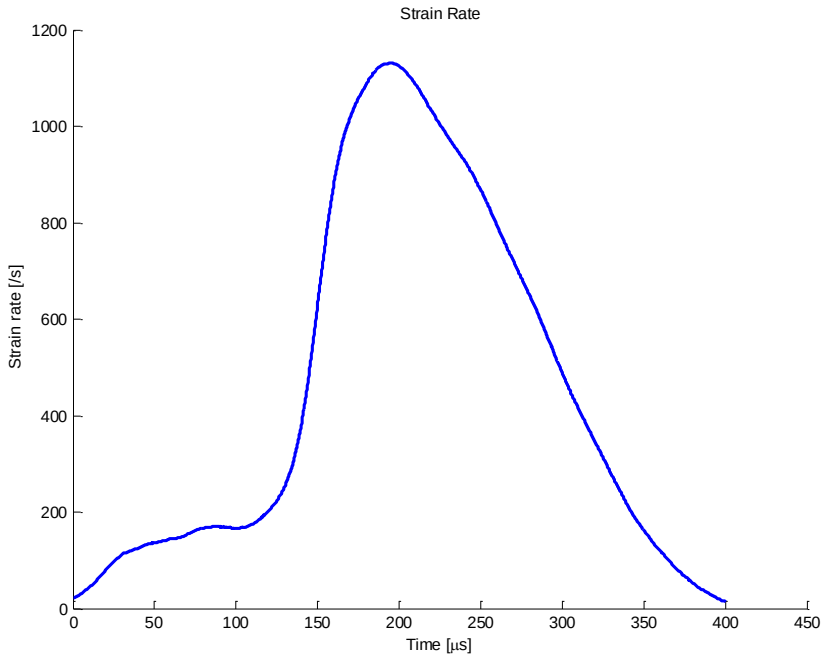

Figure A-50 Experiment 13 Strain Rate History

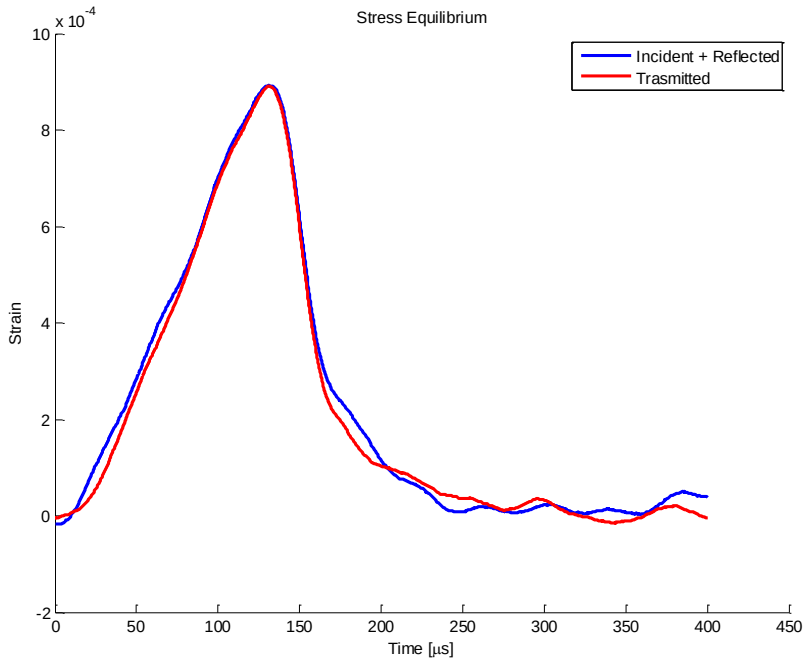

Figure A-51 Experiemnt 13 Stress Equlibrium

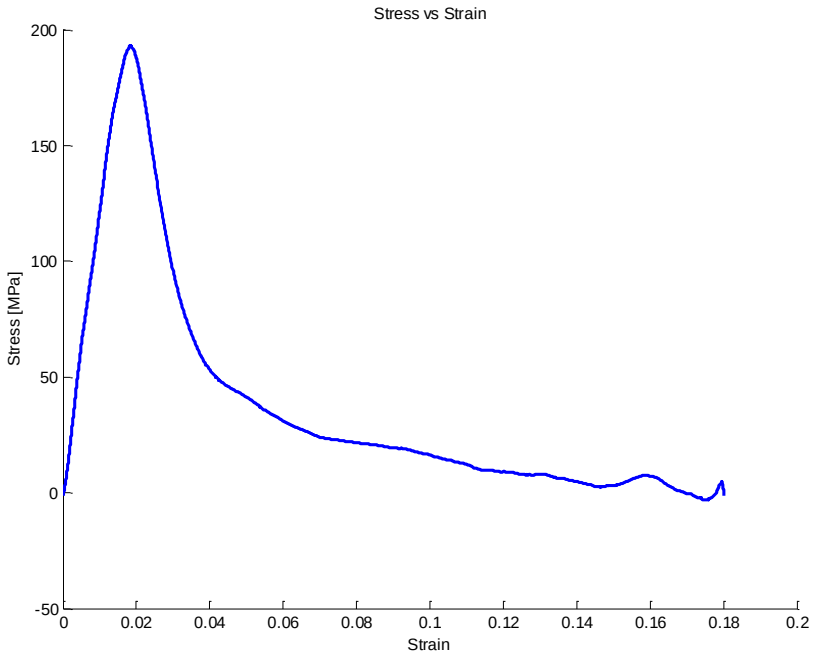

Figure A-52 Experiment 13 Stress Strain Curve

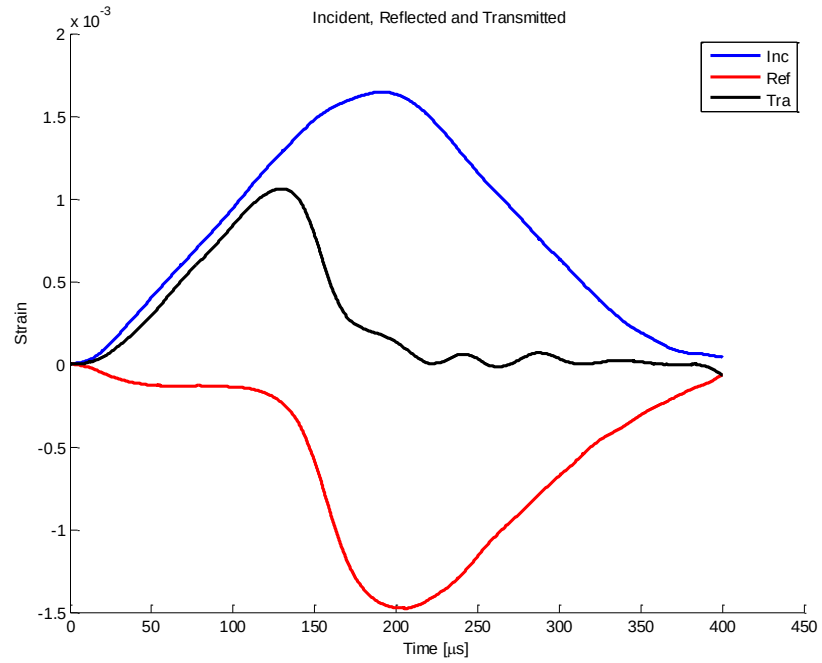

Figure A-53 Experiment 14 Incident Reflected and Transmitted Pulse

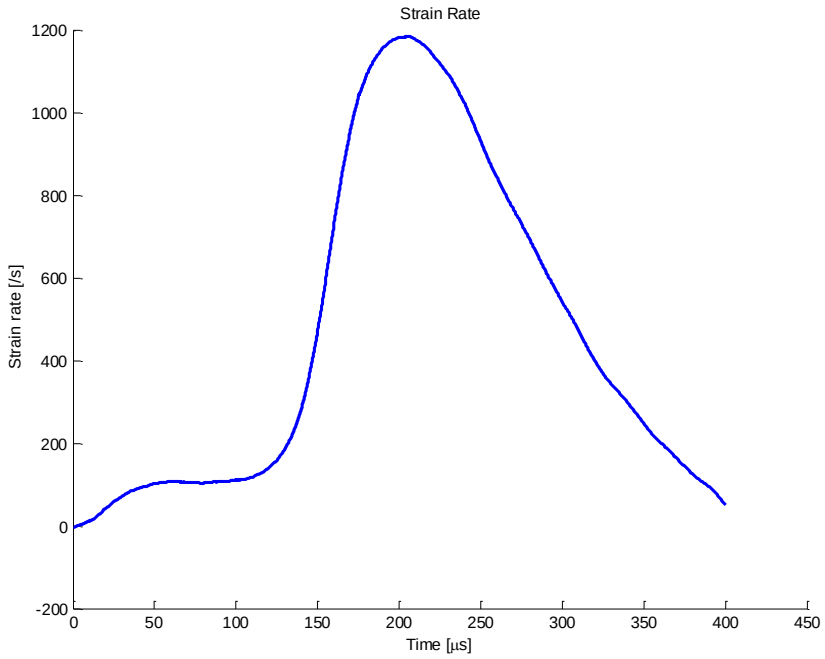

Figure A-54 Experiment 14 Strain Rate History

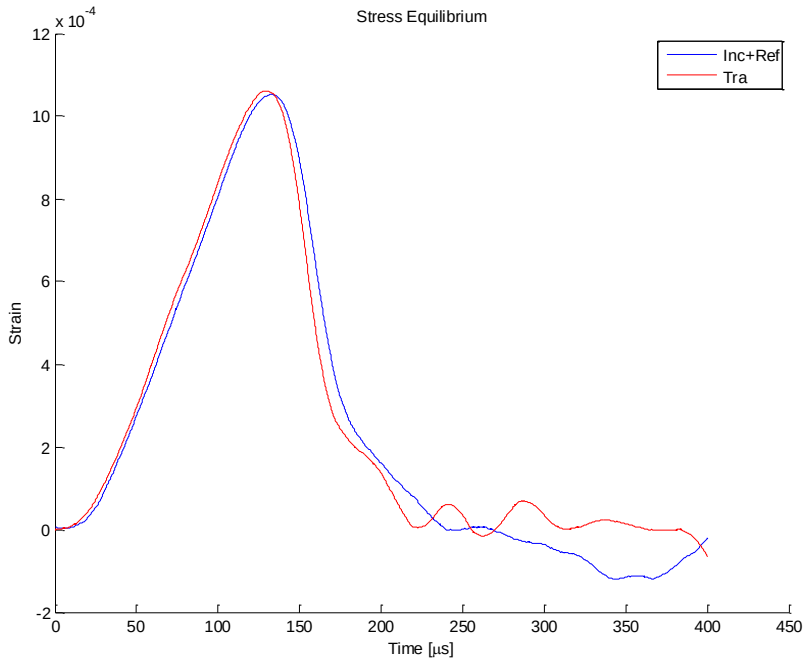

Figure A-55 Experiment 14 Stress Equilibrium

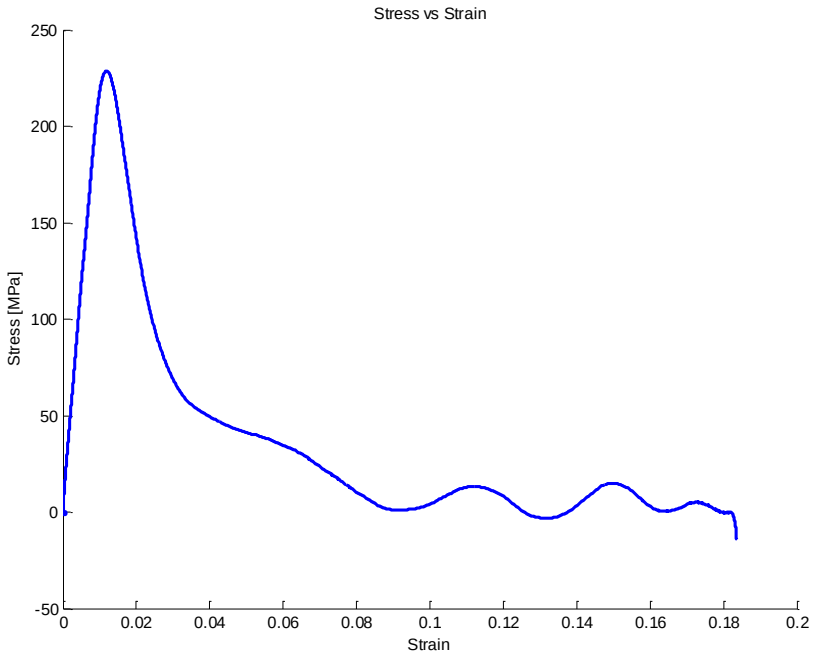

Figure A-56 Experiemnt 14 Stress Strain Curve

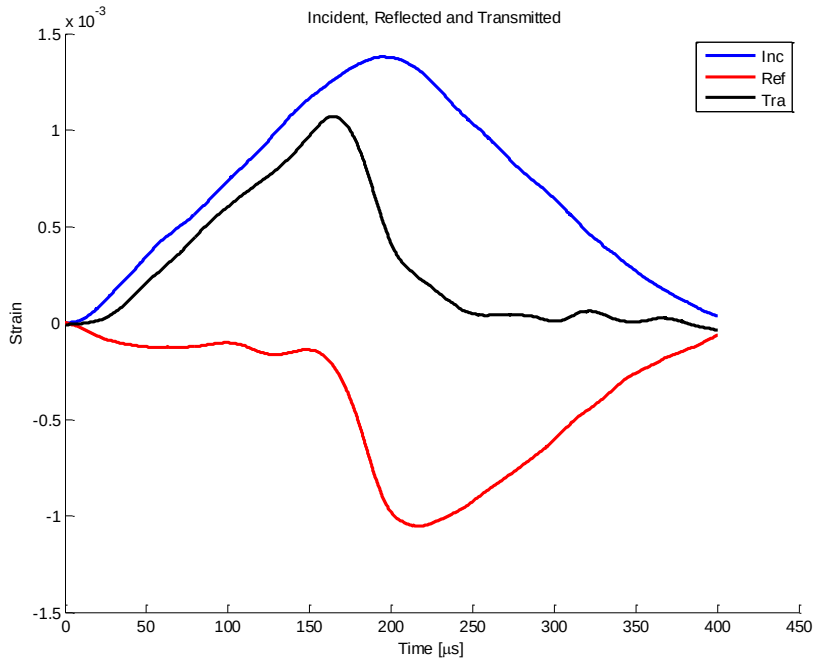

Figure A-57 Experiment 15 Incident Reflected and Transmitted Pulse

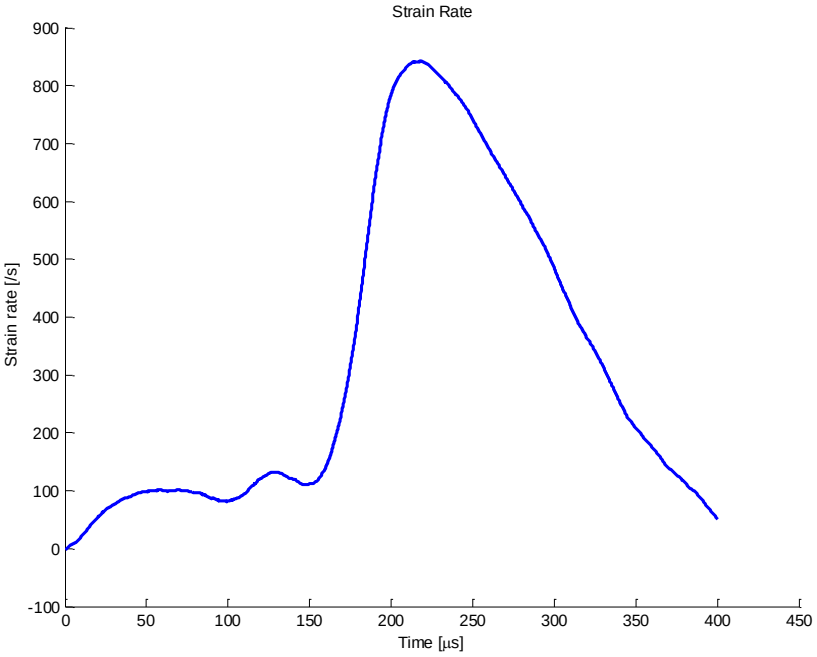

Figure A-58 Experiment 15 Strain Rate History

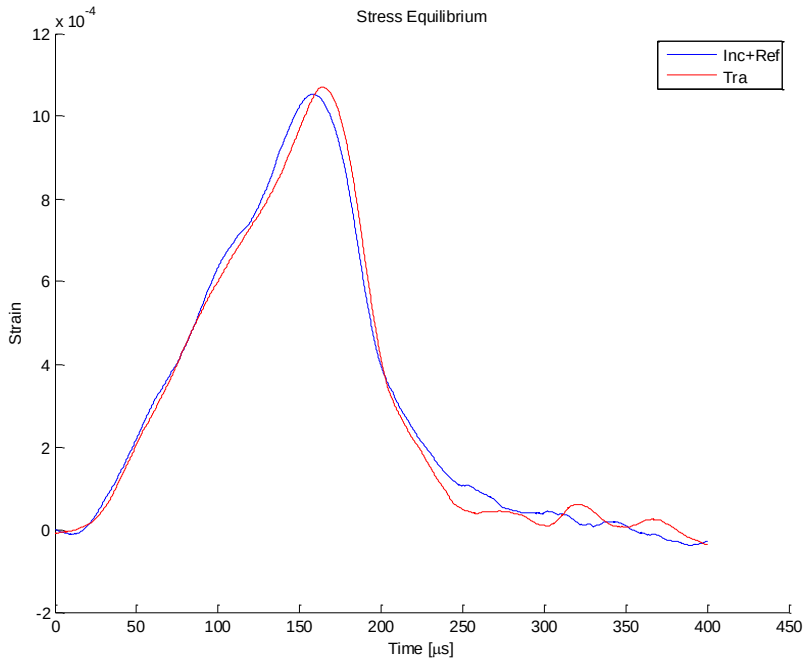

Figure A-59 Experiment 15 Stress Equilibrium

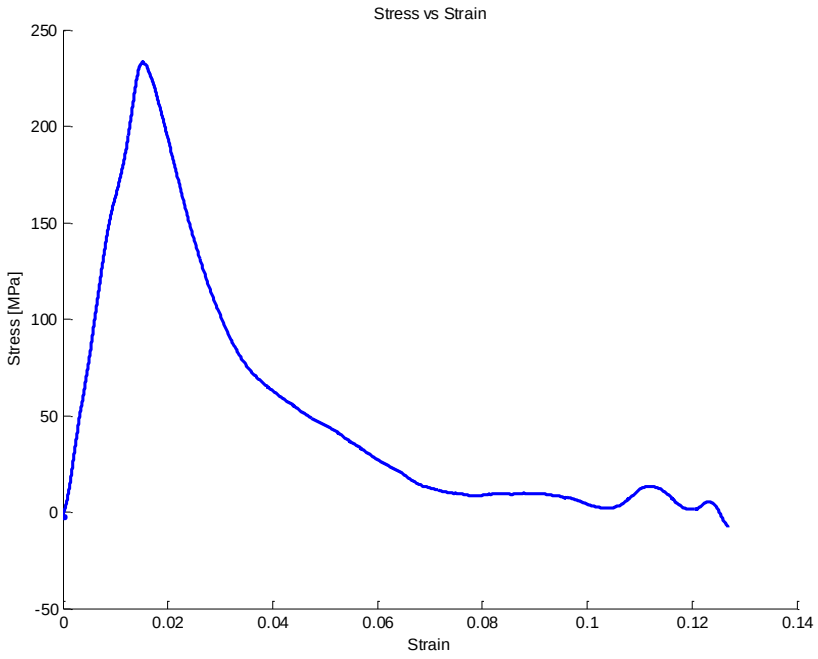

Figure A-60 Experiment 15 Stress Strain Curve

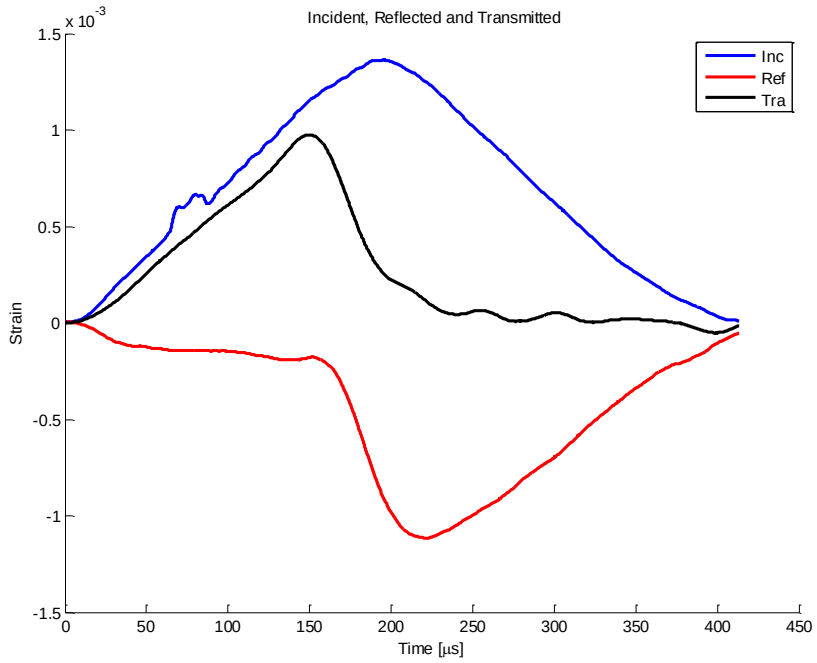

Figure A-61 Experiment 16 Incident Reflected and Transmitted Pulse

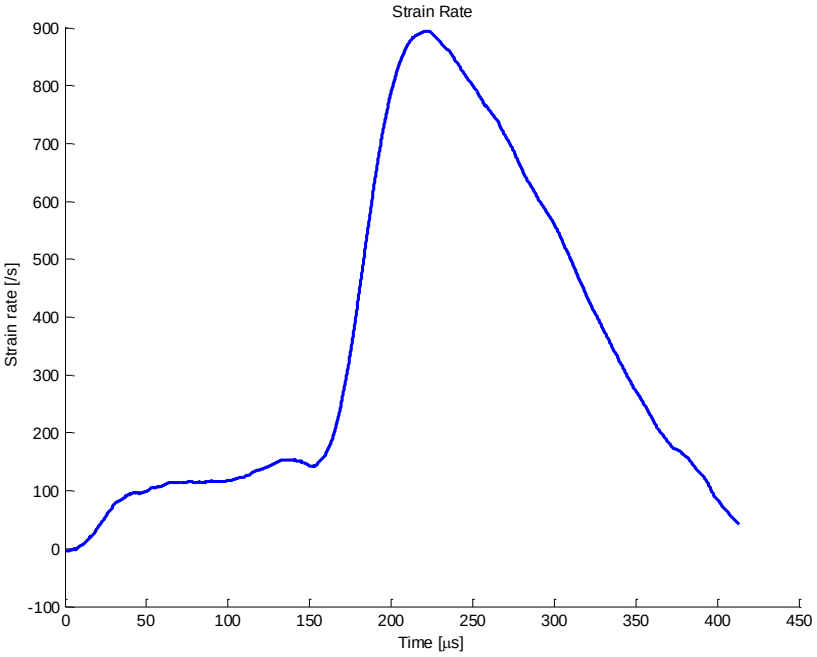

Figure A-62 Experiment 16 Strain Rate History

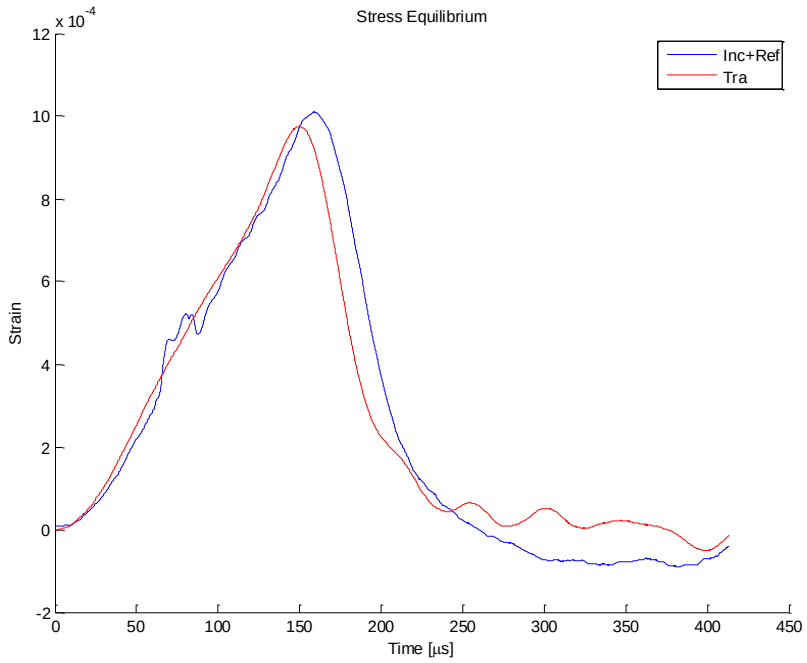

Figure A-63 Experiment 16 Stress Equilibrium

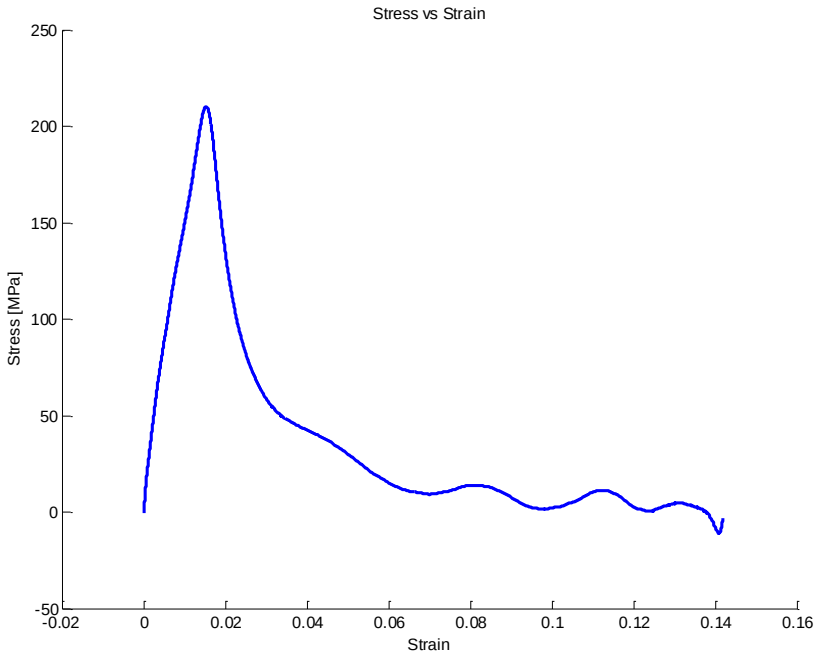

Figure A-64 Experiment 16 Stress Strain Curve

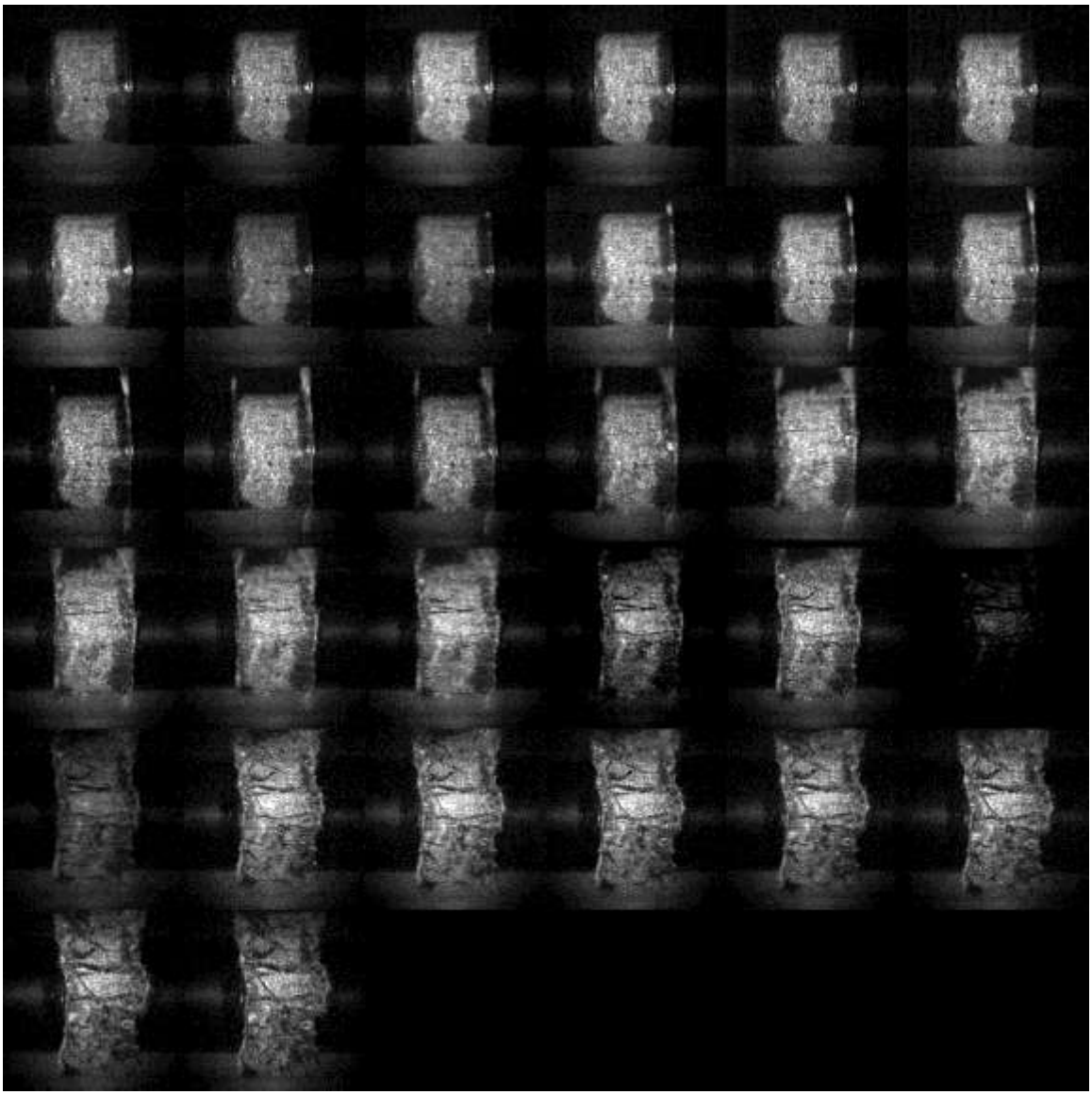

Figure A-65 Experiment 16 High Speed Images at Frame Rate 83770 fps

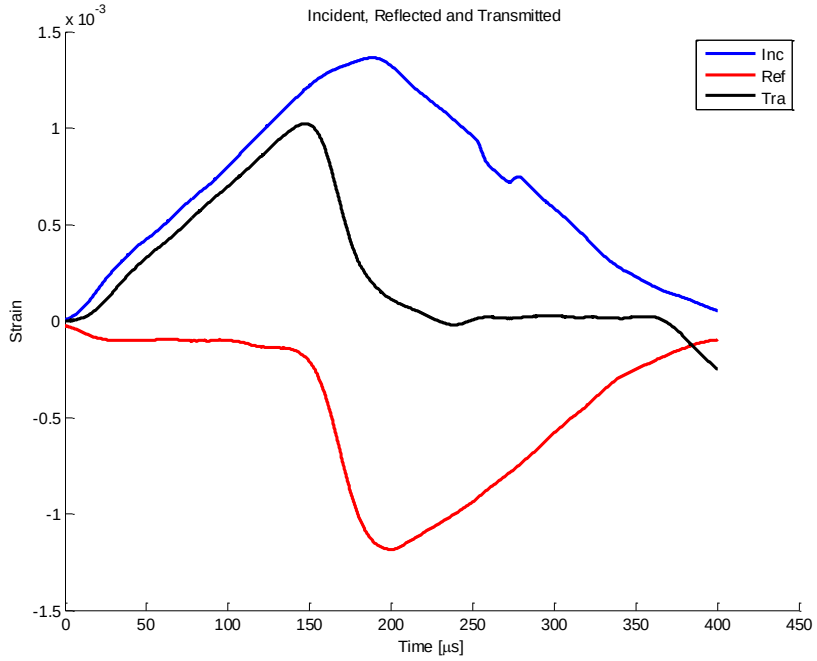

Figure A-66 Experiment 17 Incident Reflected and Transmitted Pulse

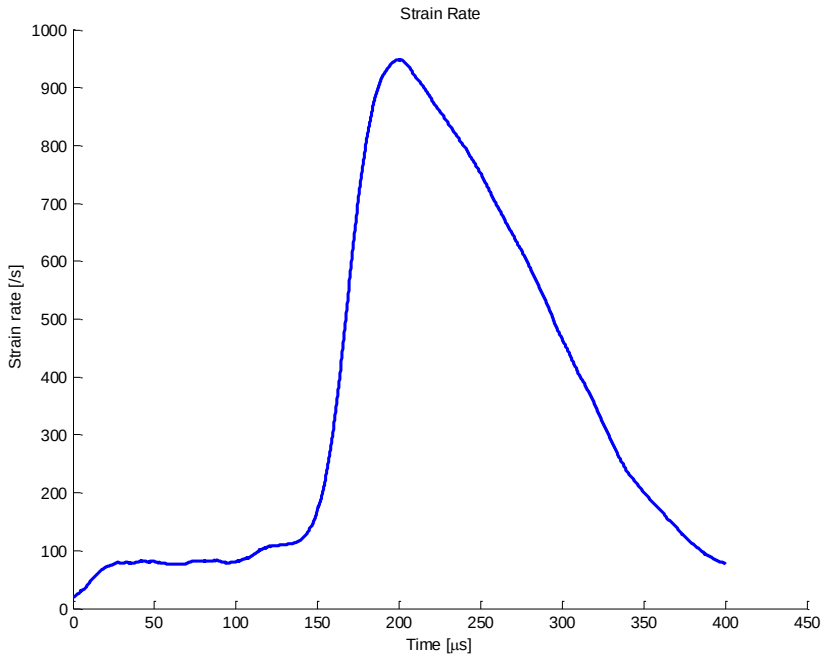

Figure A-67 Experiment 17 Strain Rate History

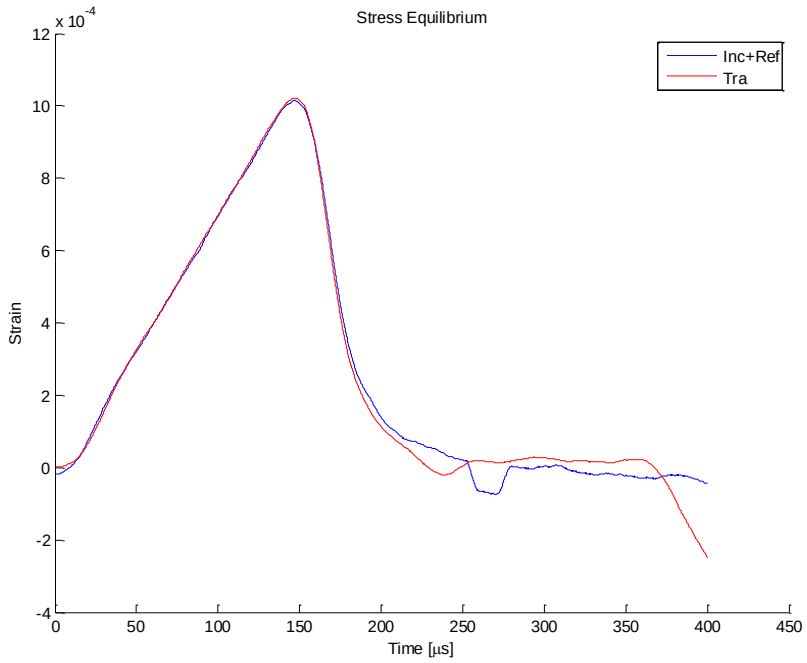

Figure A-68 Experiment 17 Stress Equilibrium

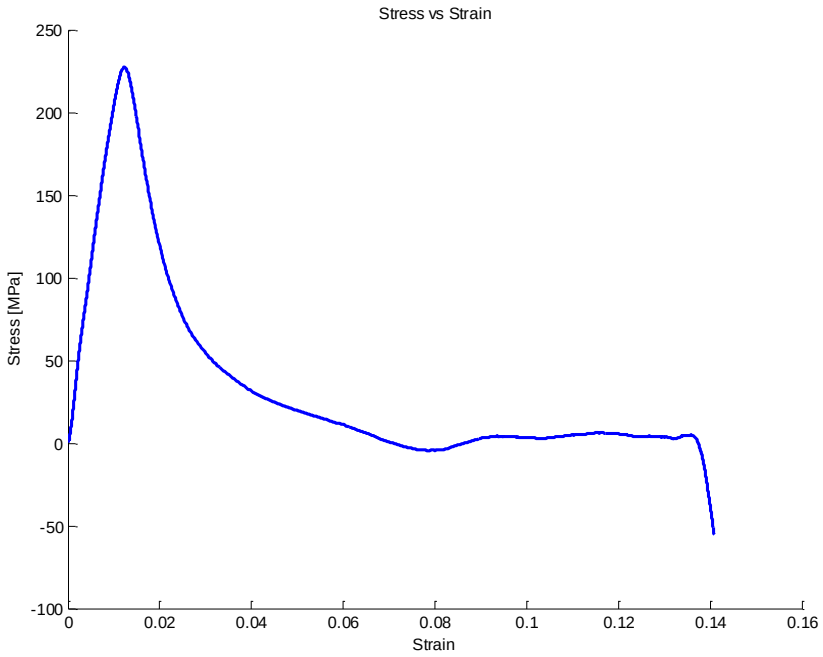

Figure A-69 Experiment 18 Stress Strain Curve

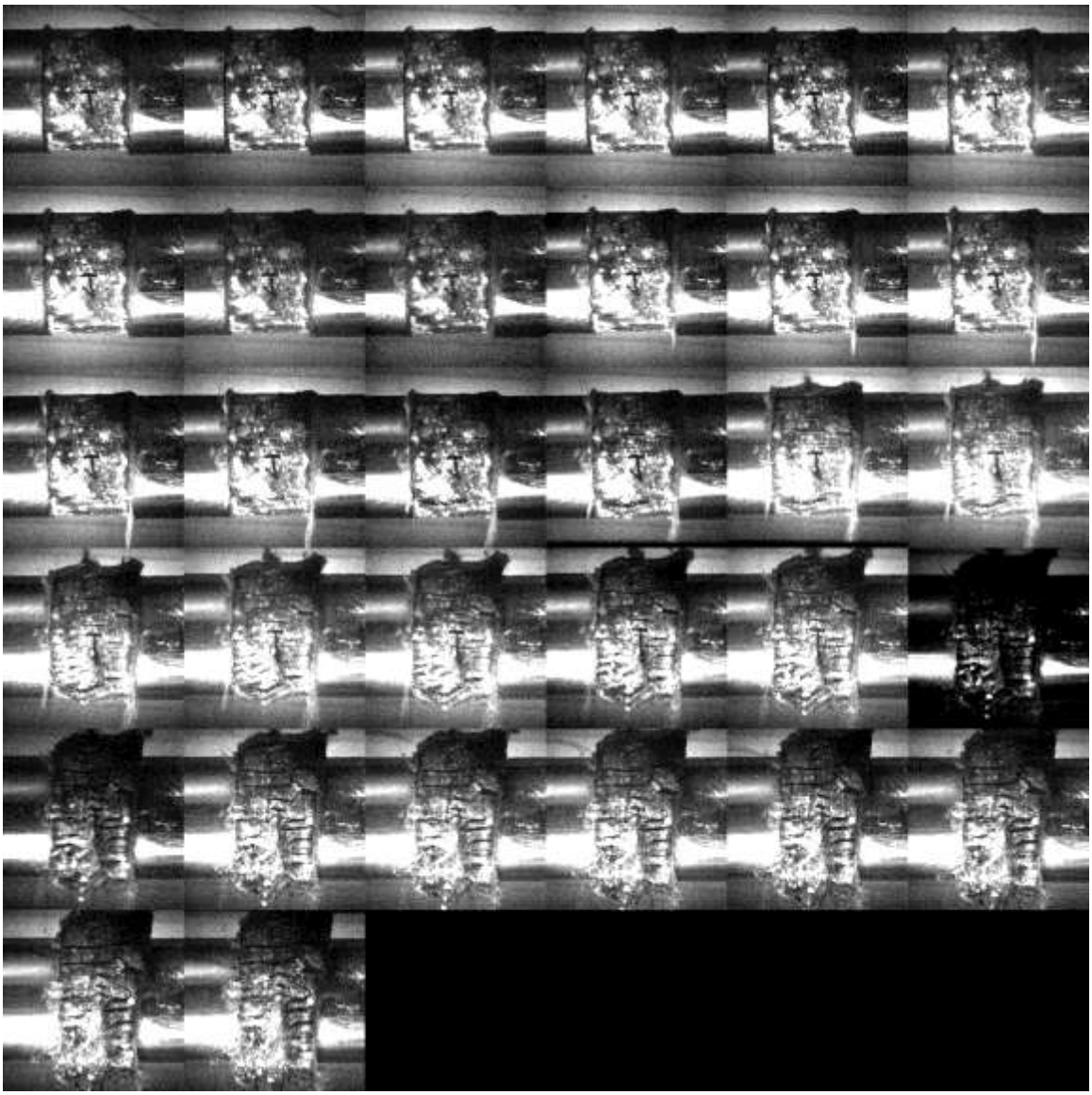

Figure A-70 Experiment 17 High Speed Images at Frame Rate 84654 fps

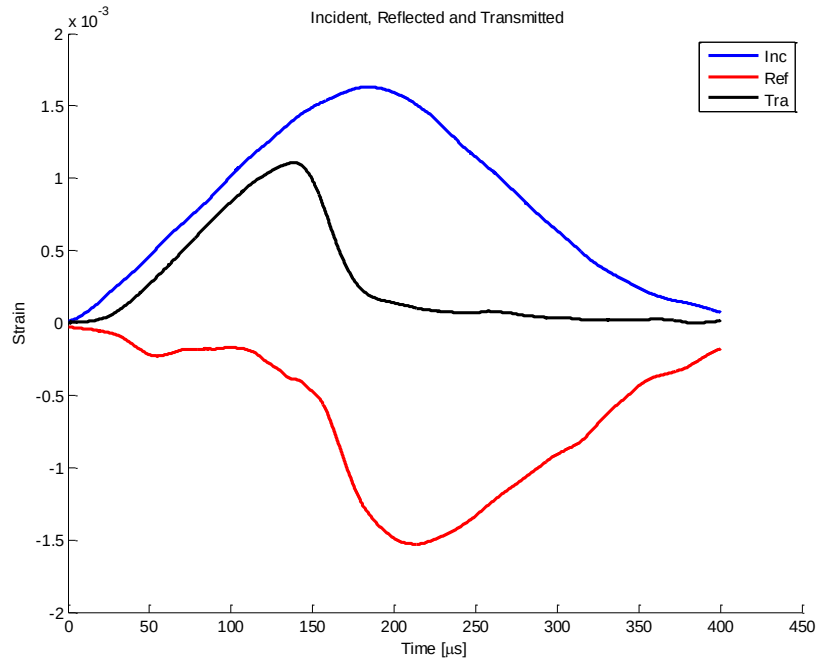

Figure A-71 Experiment 18 Incident Reflected and Transmitted Pulse

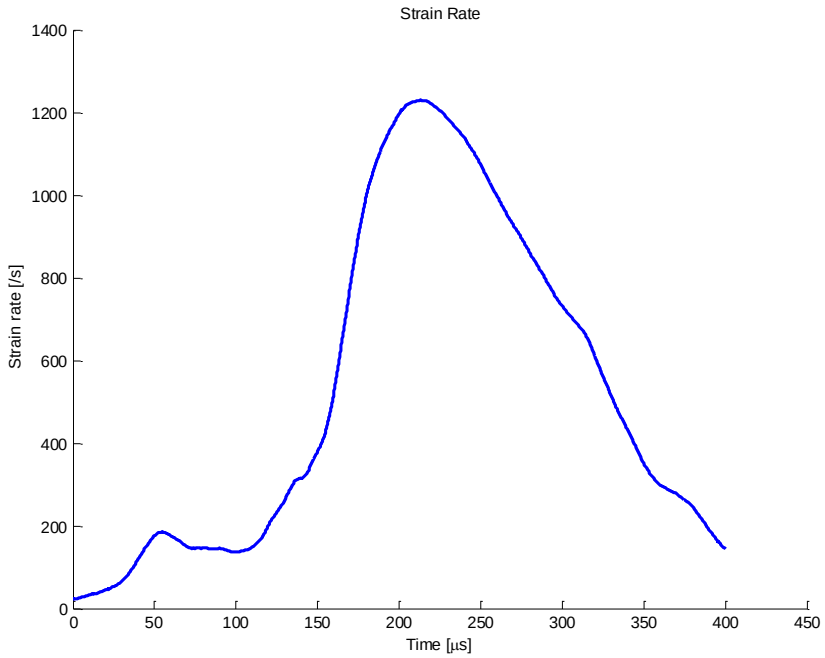

Figure A-72 Experiment 18 Strain Rate History

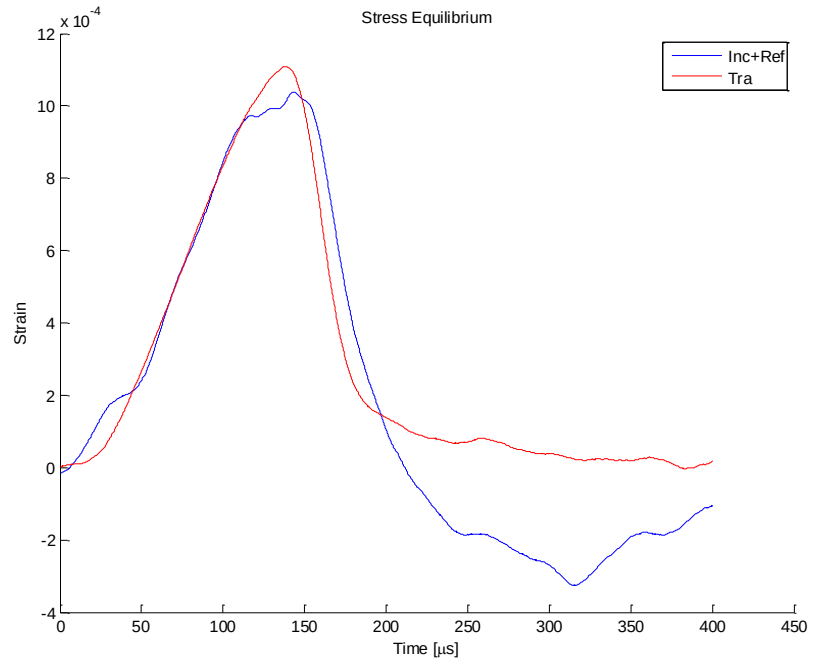

Figure A-73 Experiment 18 Stress Equilibrium

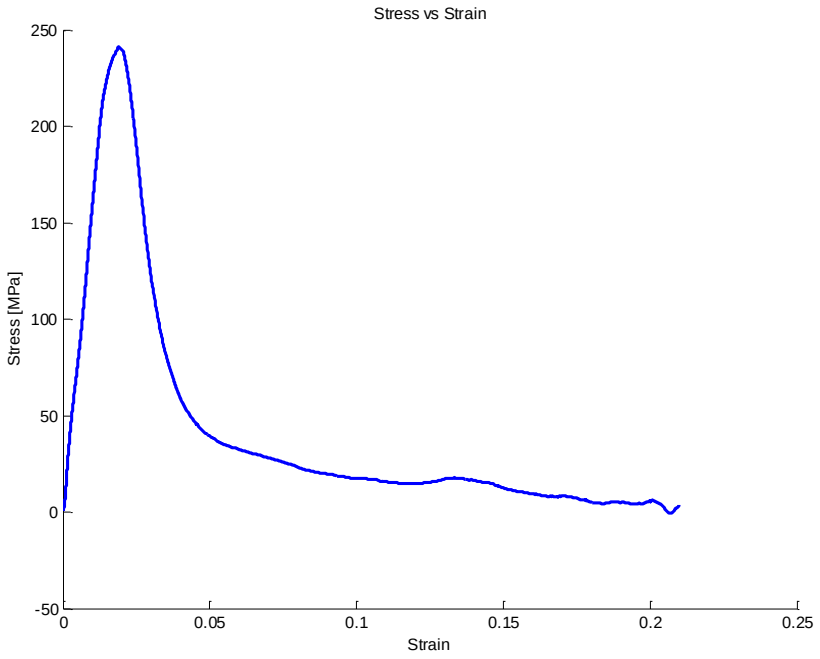

Figure A-74 Experiment 18 Stress Strain Curve

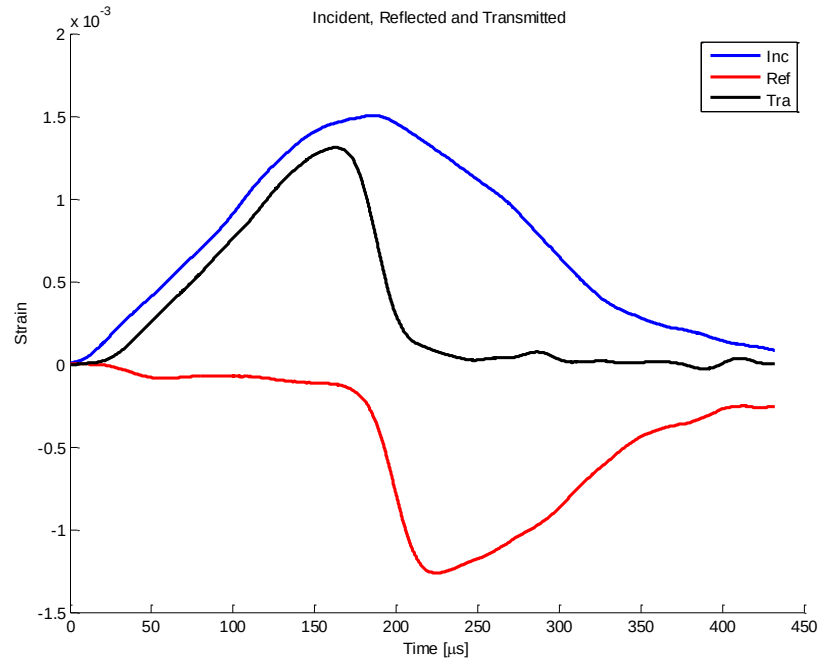

Figure A-75 Experiment 19 Incident Reflected and Transmitted Pulse

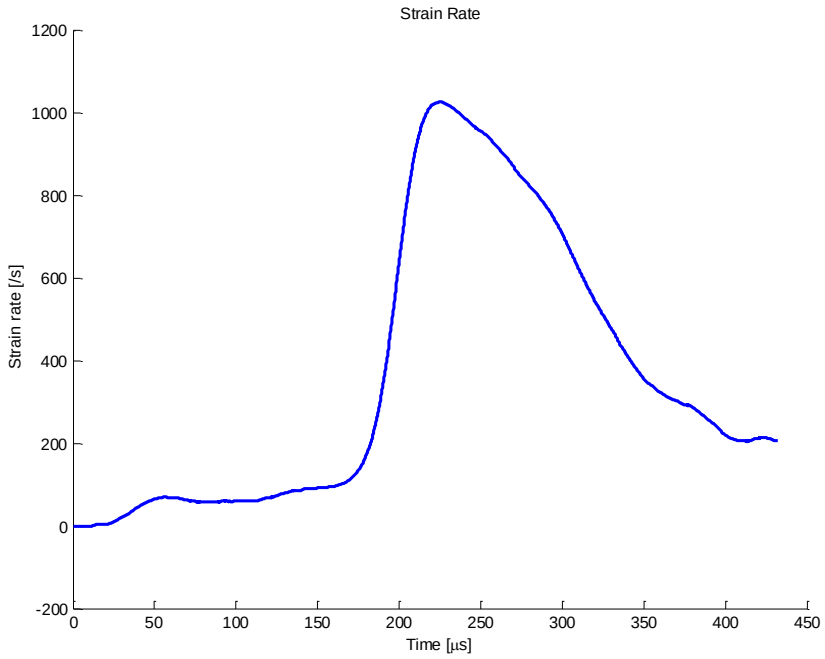

Figure A-76 Experiment 19 Strain Rate History

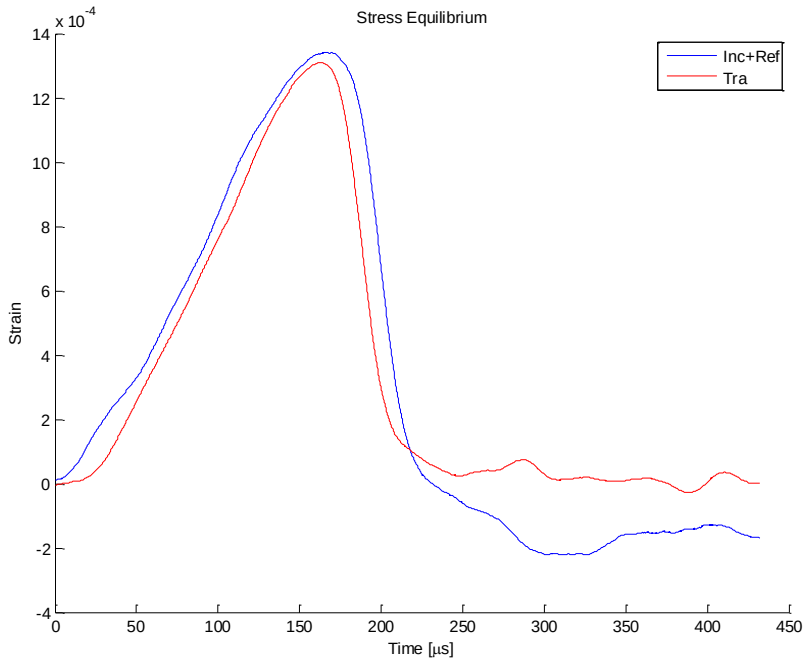

Figure A-77 Experiment 19 Stress Equilibrium

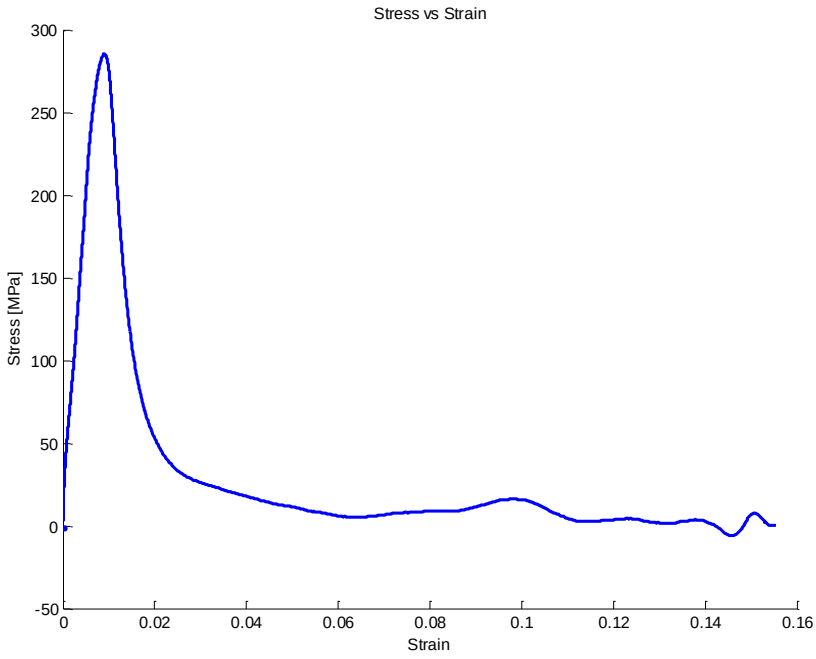

Figure A-78 Experiment 19 Stress Strain Curve

A2: Dynamic Uniaxial Compressive Experiments on Small New Cor Tuf

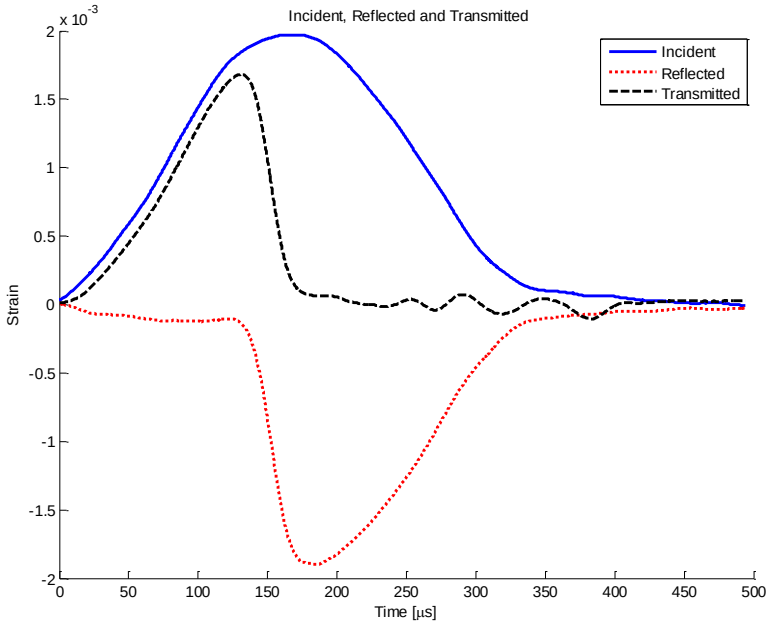

Figure A-79 Experiment 1 Incident Reflected and Transmitted Pulse

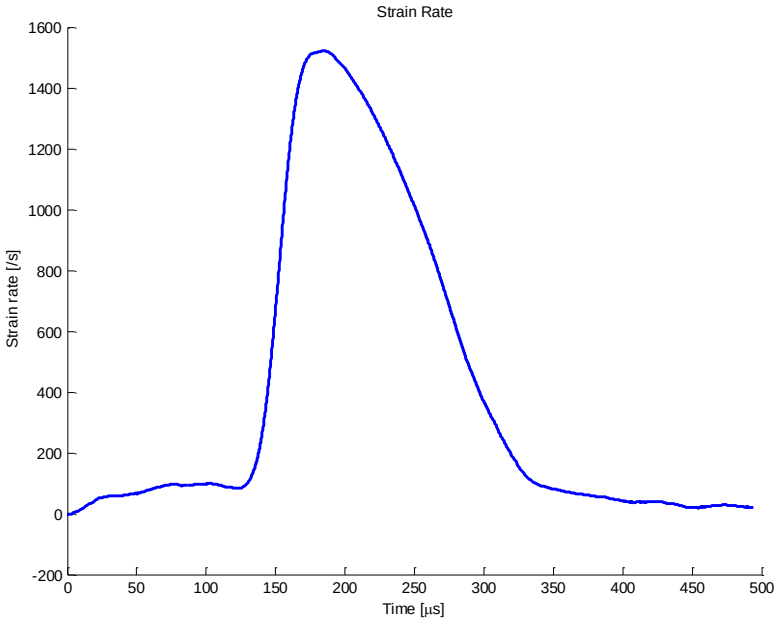

Figure A-80 Experiment 1 Strain Rate History

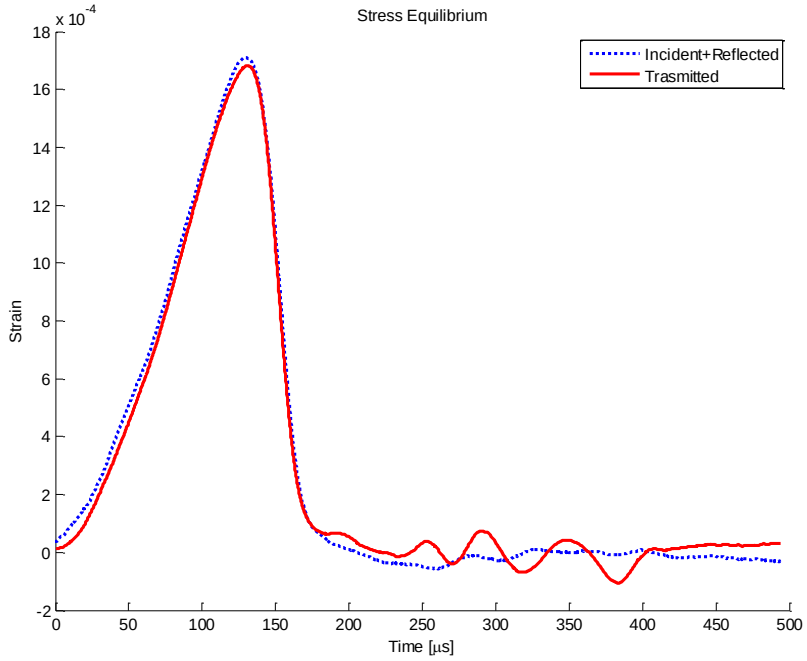

Figure A-81 Experiment 1 Stress Equilibrium

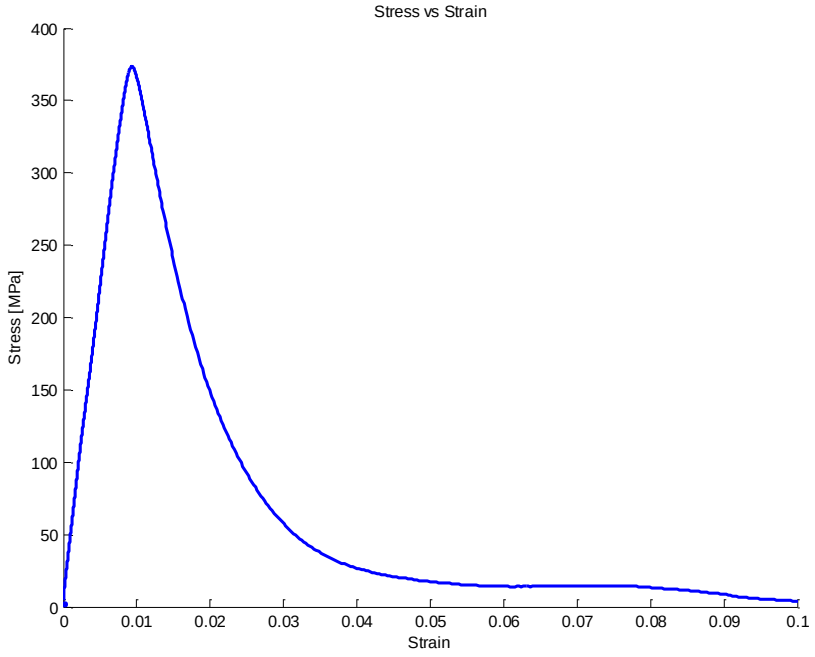

Figure A-82 Experiment 1 Stress Strain Curve

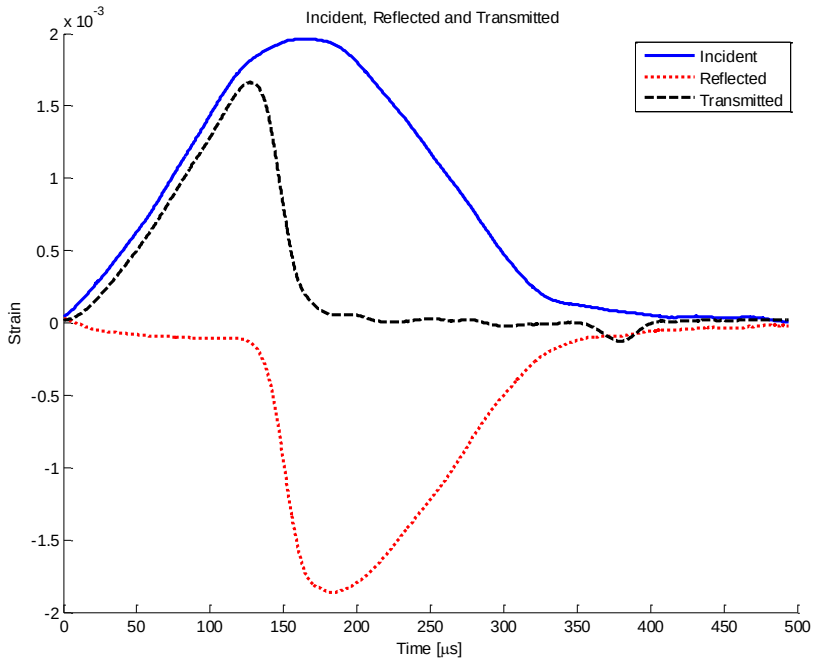

Figure A-83 Experiment 2 Incident Reflected and Transmitted Pulse

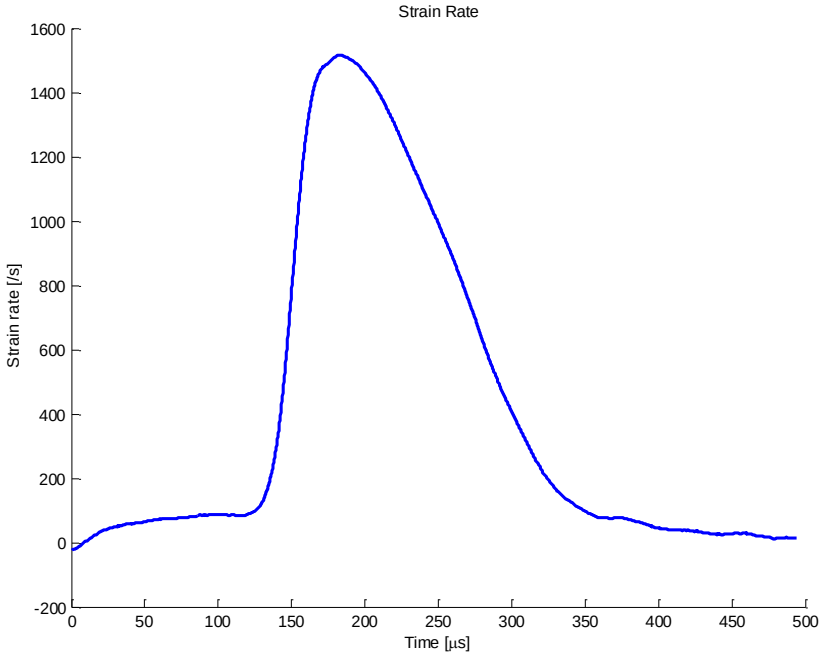

Figure A-84 Experiment 2 Strain Rate History

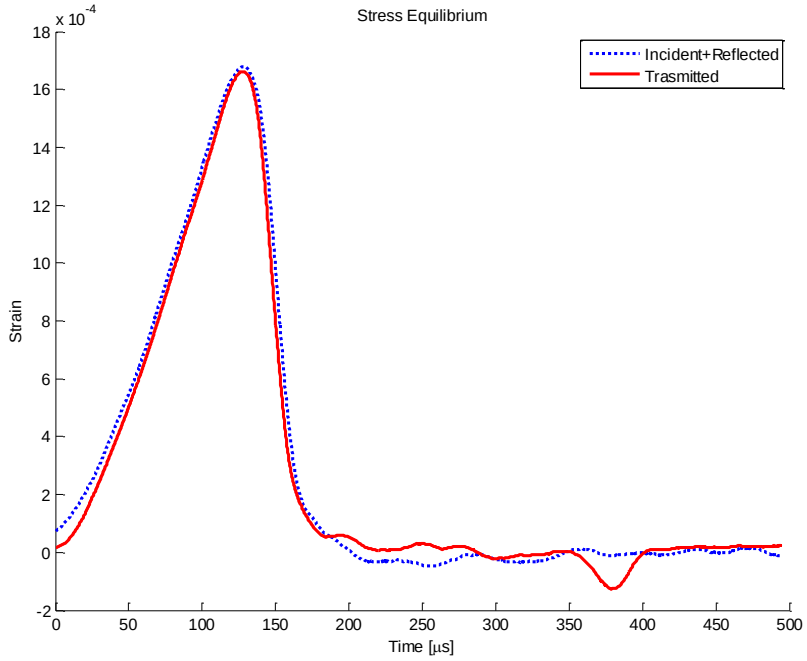

Figure A-85 Experiment 2 Stress Equilibrium

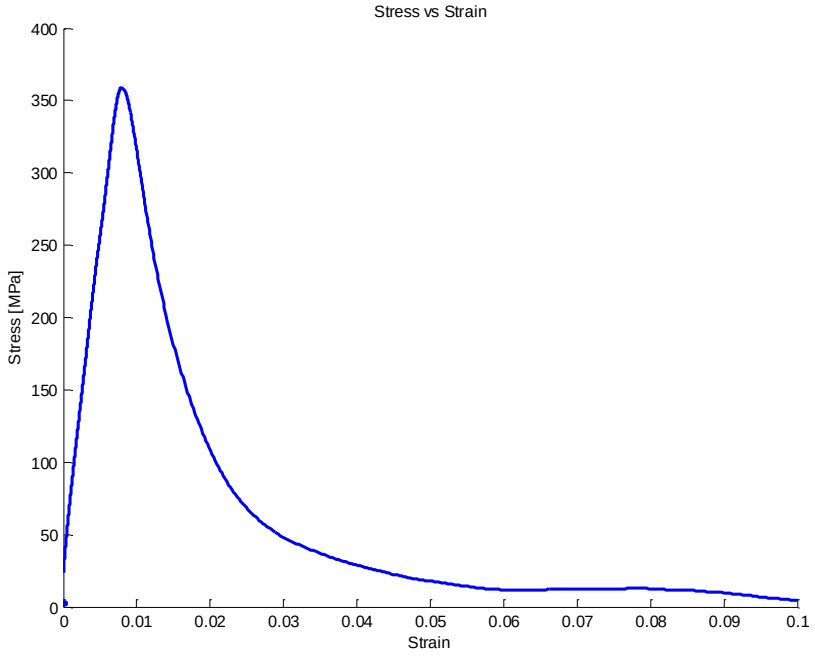

Figure A-86 Experiment 2 Stress Strain Curve

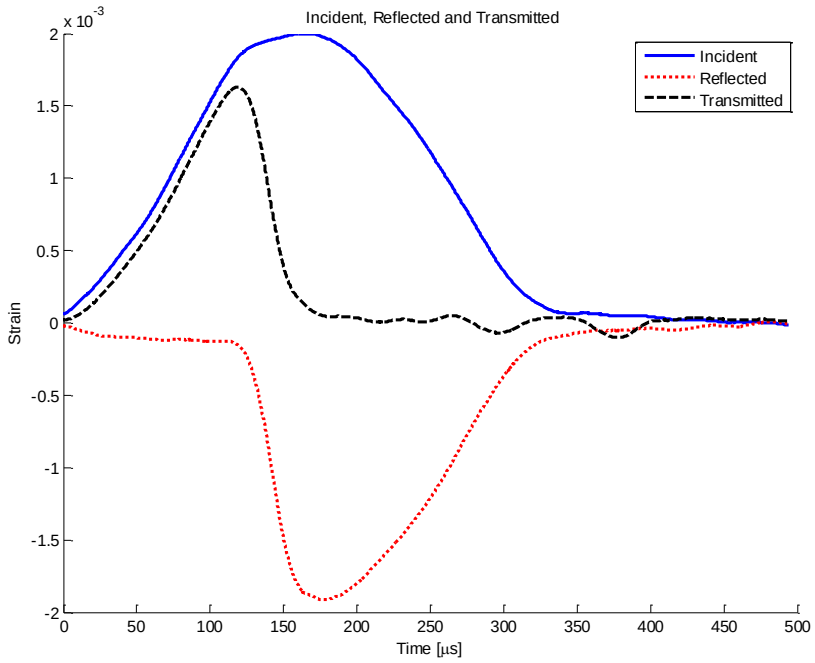

Figure A-87 Experiment 3 Incident Reflected and Transmitted Pulse

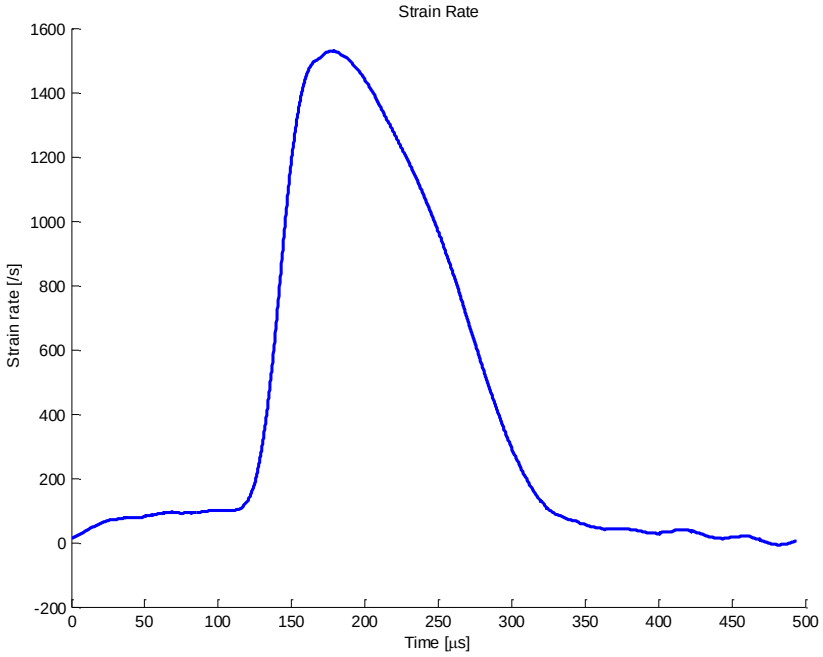

Figure A-88 Experiment 3 Strain Rate History

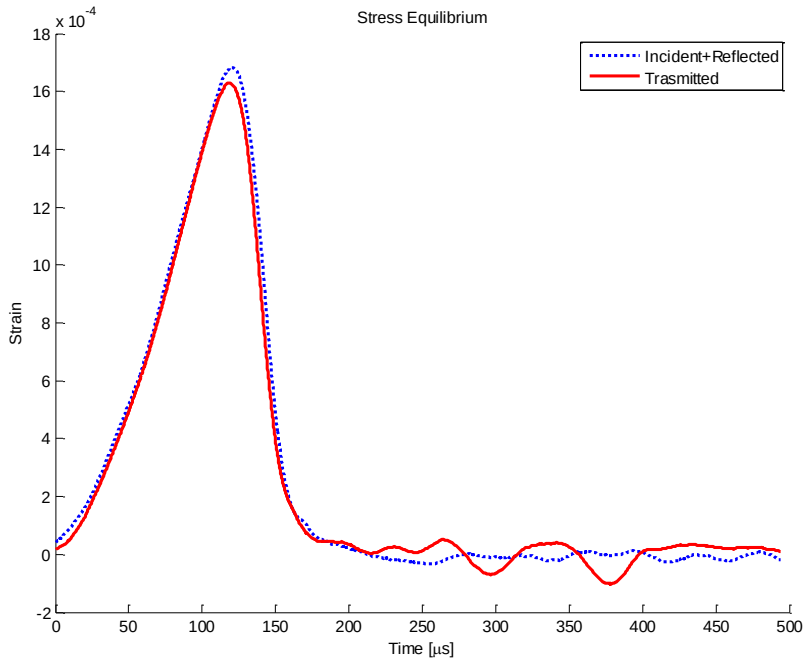

Figure A-89 Experiment 3 Stress Equilibrium

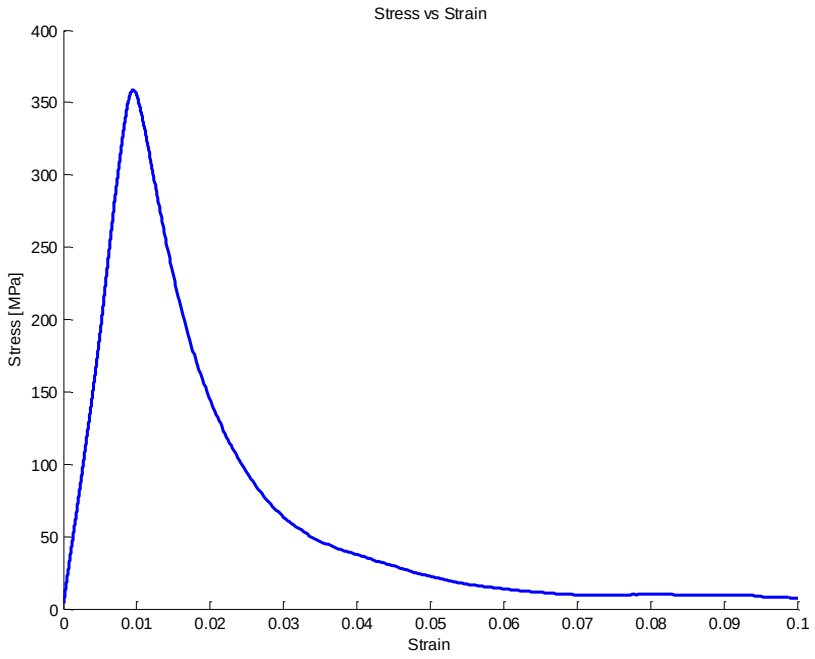

Figure A-90 Experiment 3 Stress Strain Curve

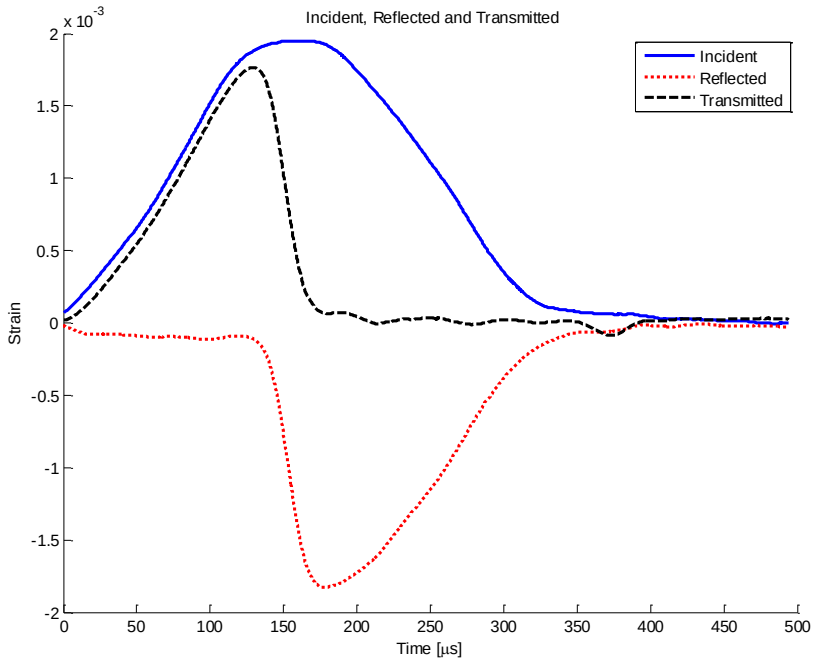

Figure A-91 Experiment 4 Incident Reflected and Transmitted Pulse

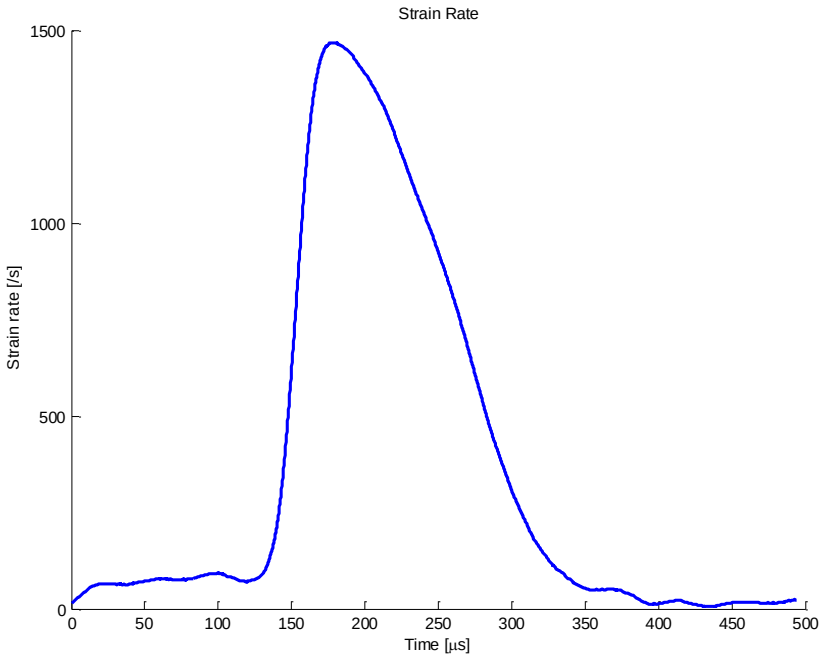

Figure A-92 Experiment 4 Strain Rate History

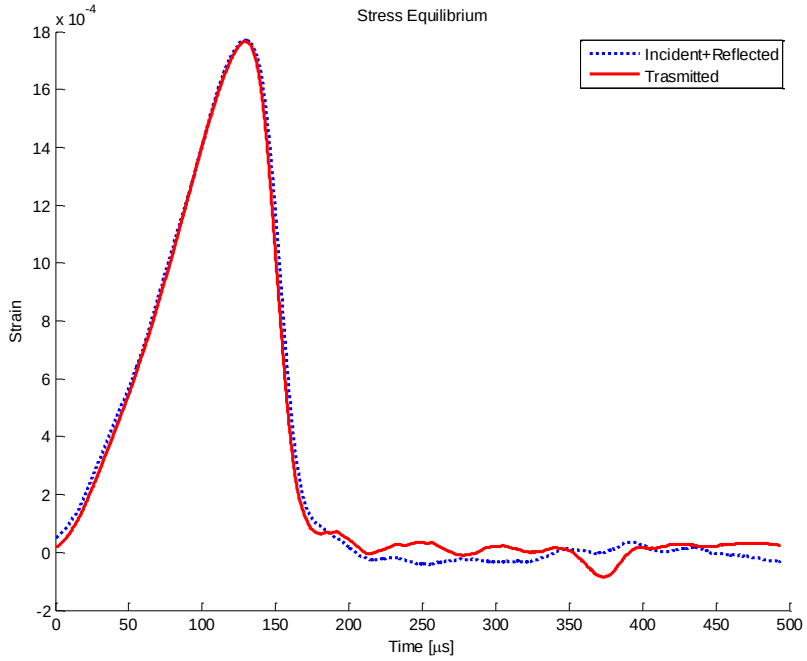

Figure A-93 Experiment 4 Stress Equilibrium

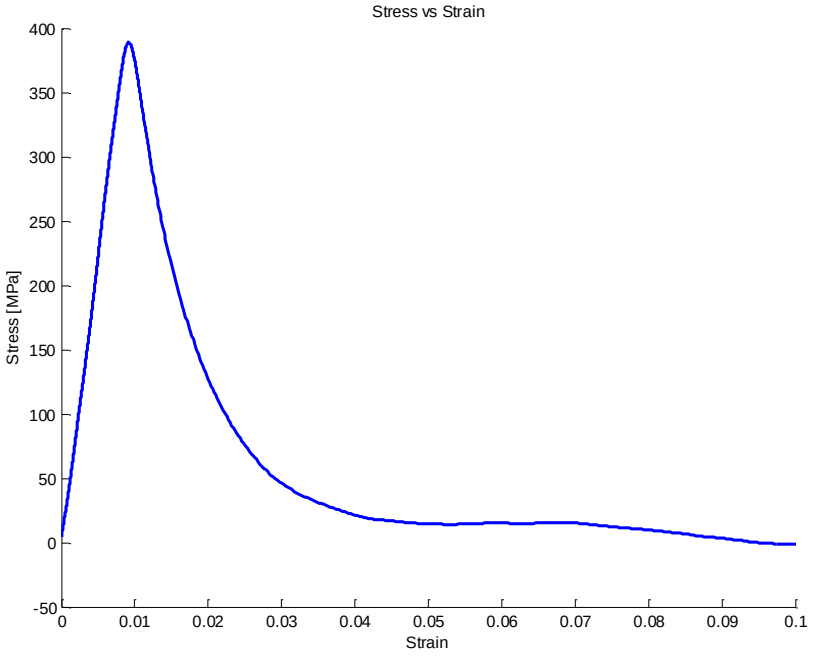

Figure A-94 Experiment 4 Stress Strain Curve

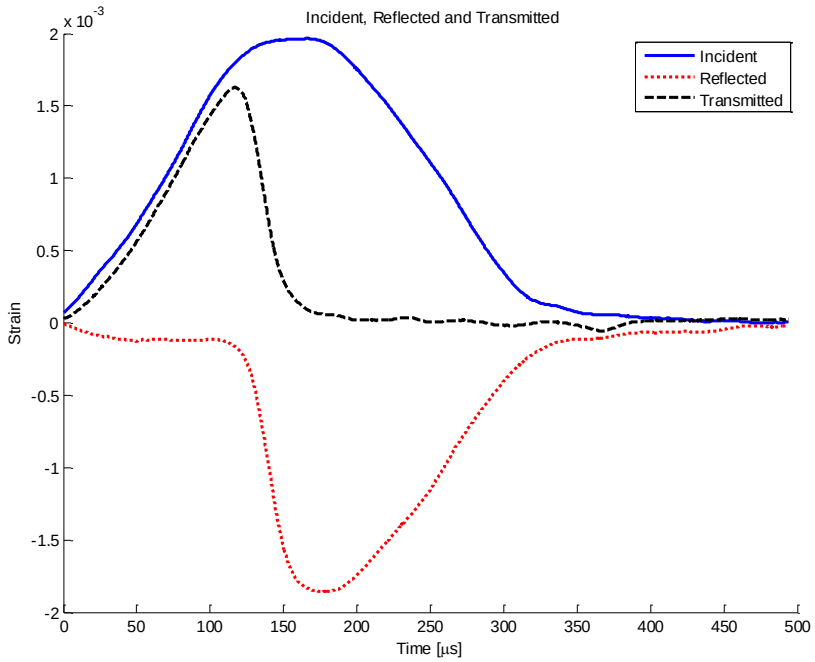

Figure A-95 Experiment 5 Incident Reflected and Transmitted Pulse

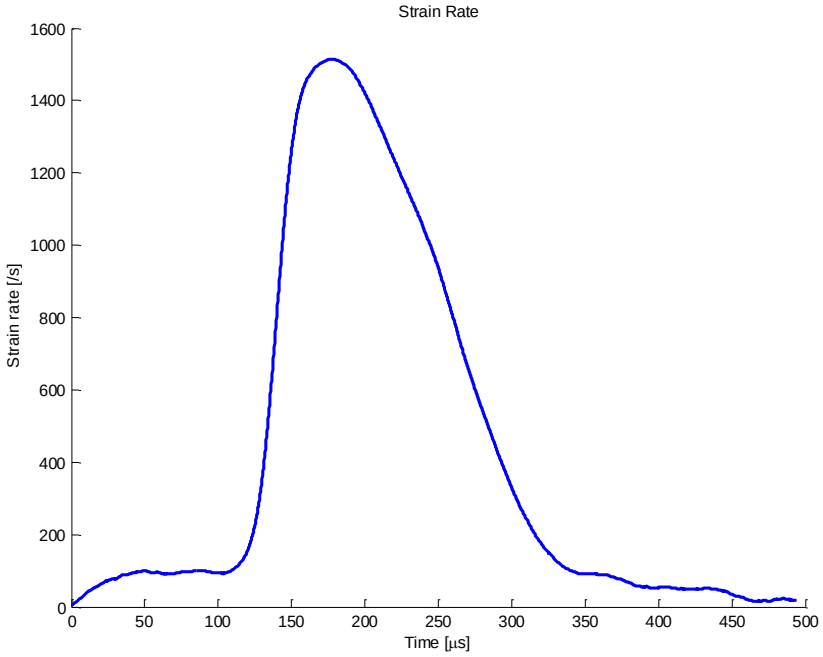

Figure A-96 Experiment 5 Strain Rate History

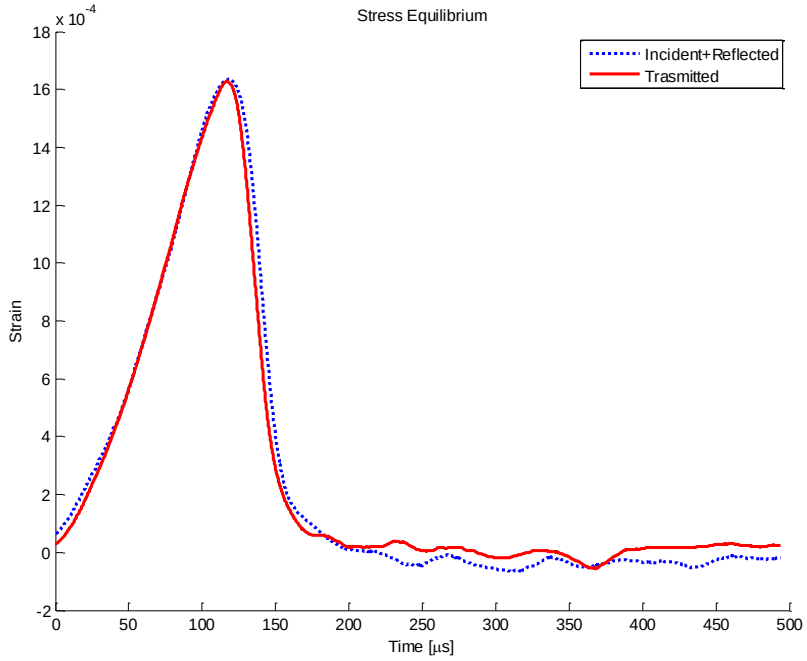

Figure A-97 Experiment 5 Stress Equilibrium

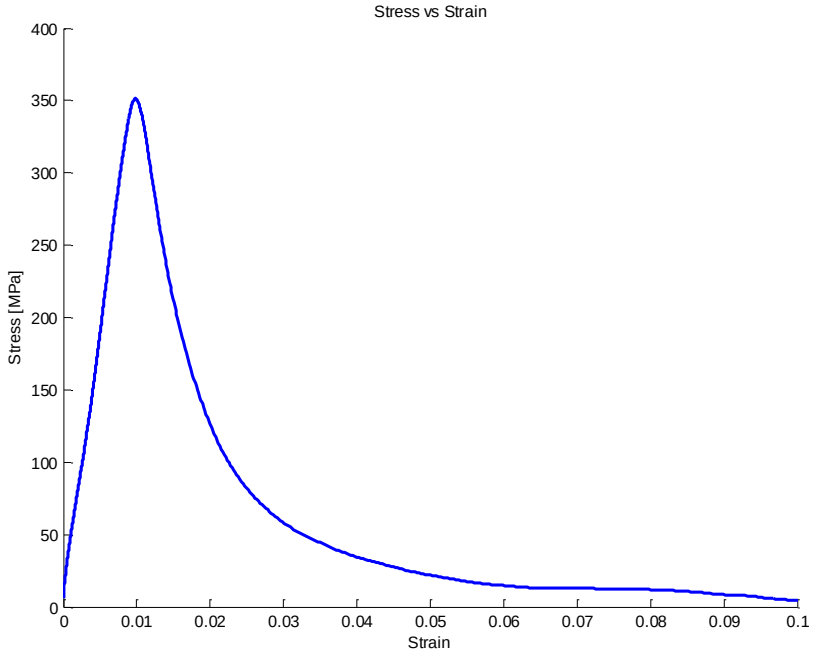

Figure A-98 Experiment 5 Stress Strain Curve

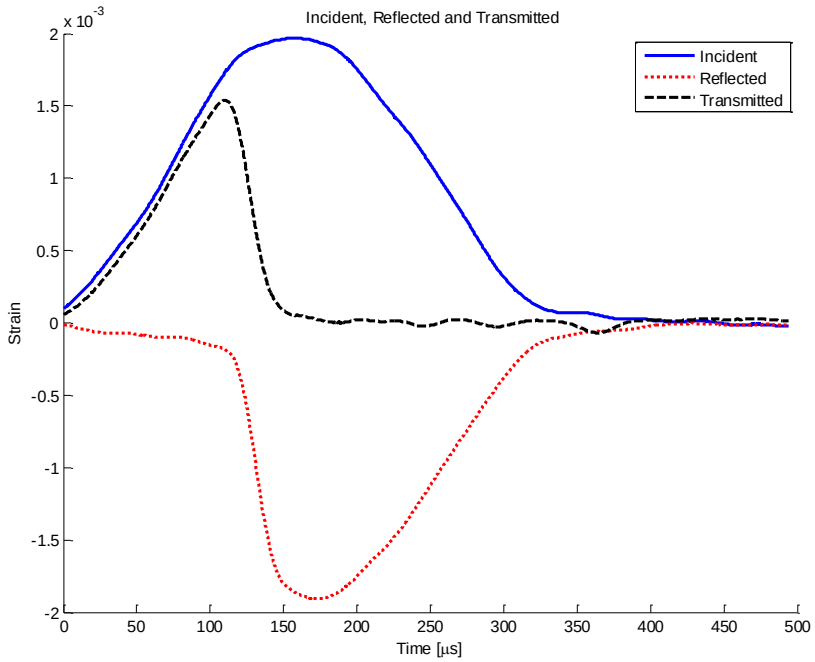

Figure A-99 Experiment 6 Incident Reflected and Transmitted Pulse

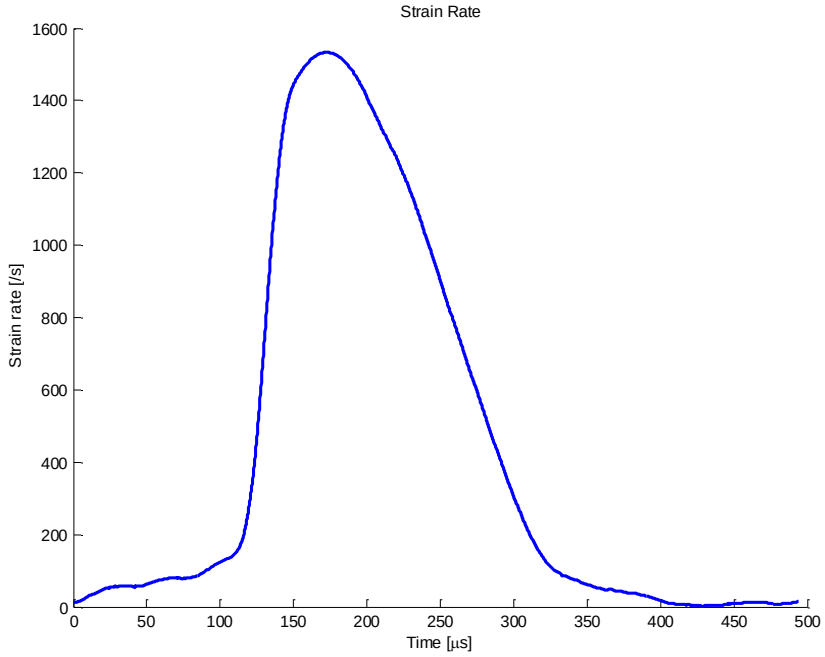

Figure A-100 Experiment 6 Strain Rate History

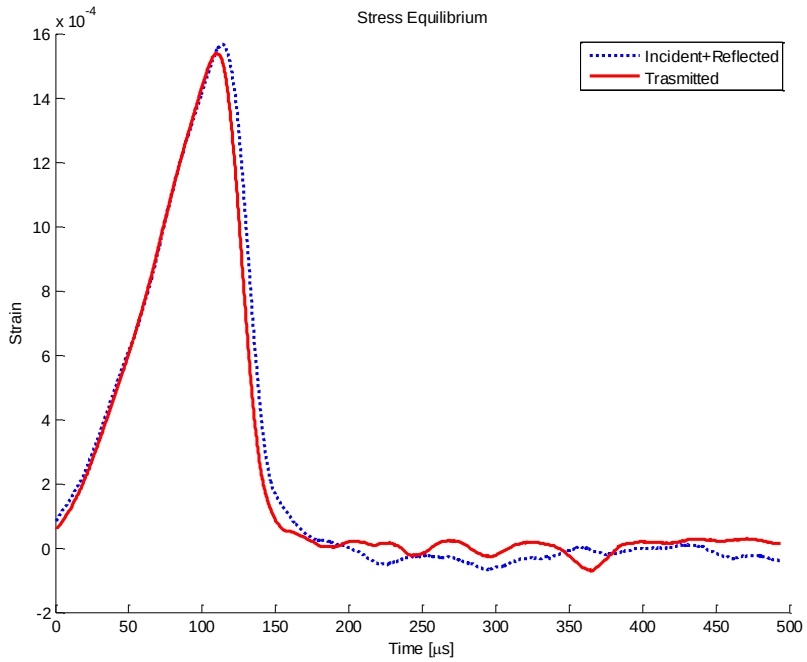

Figure A-101 Experiment 6 Stress Equilibrium

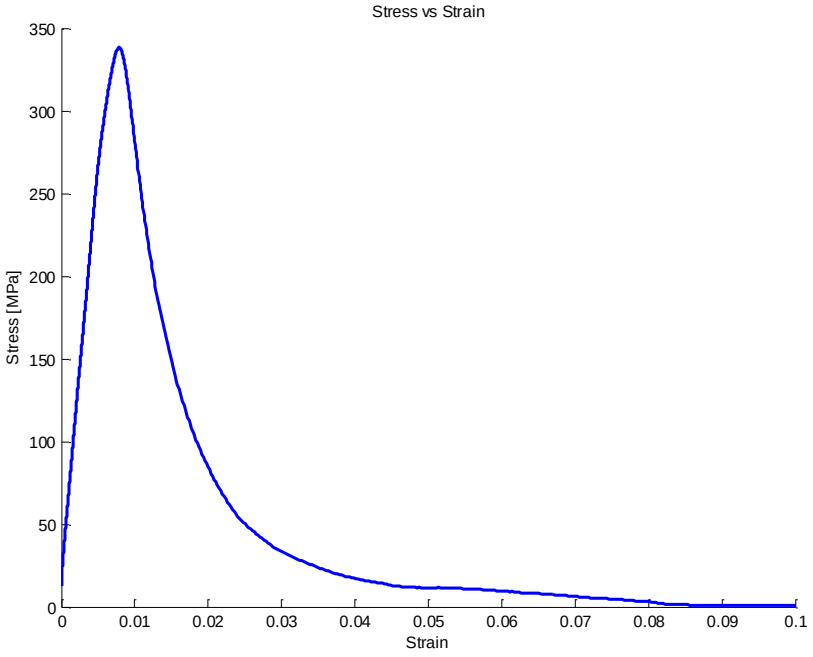

Figure A-102 Experiment 6 Stress Strain Curve

A3: Dynamic Uniaxial Compressive Experiments on Big Old Cor Tuf

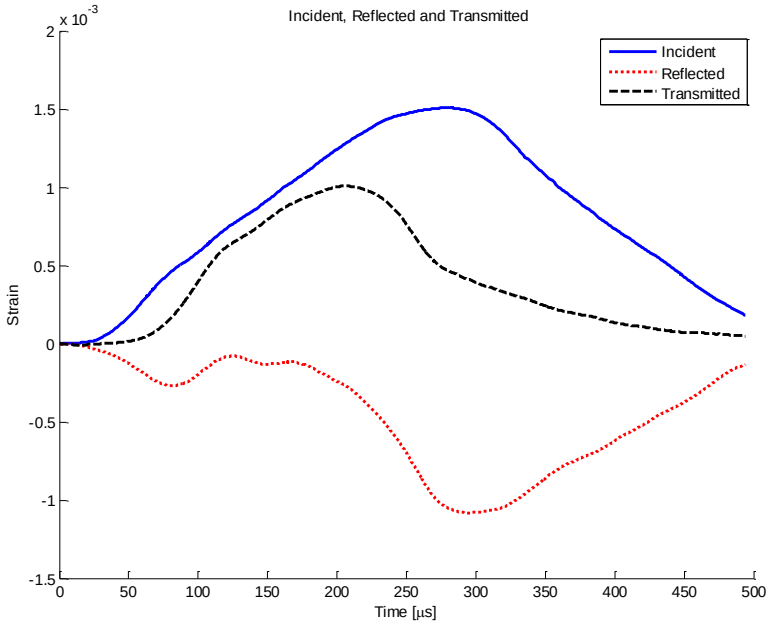

Figure A-103 Experiment 1 Incident Reflected and Transmitted Pulse

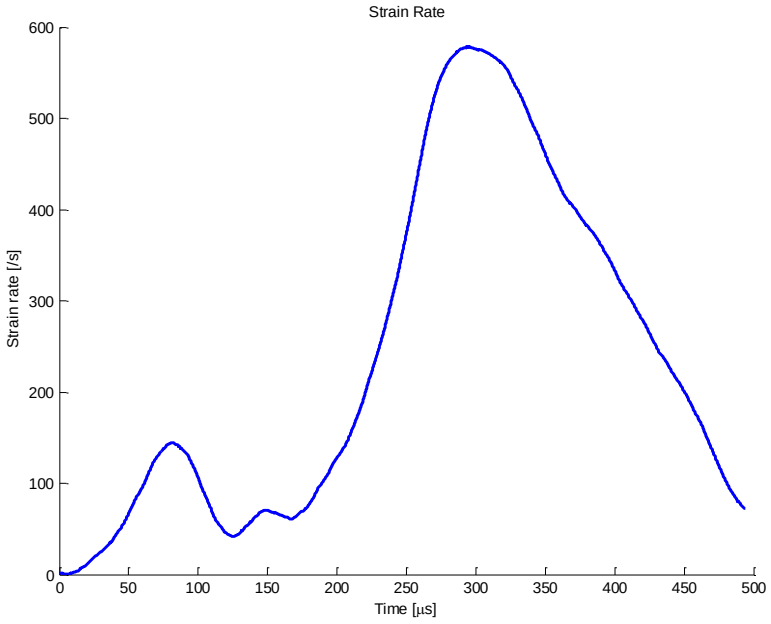

Figure A-104 Experiment 1 Strain Rate History

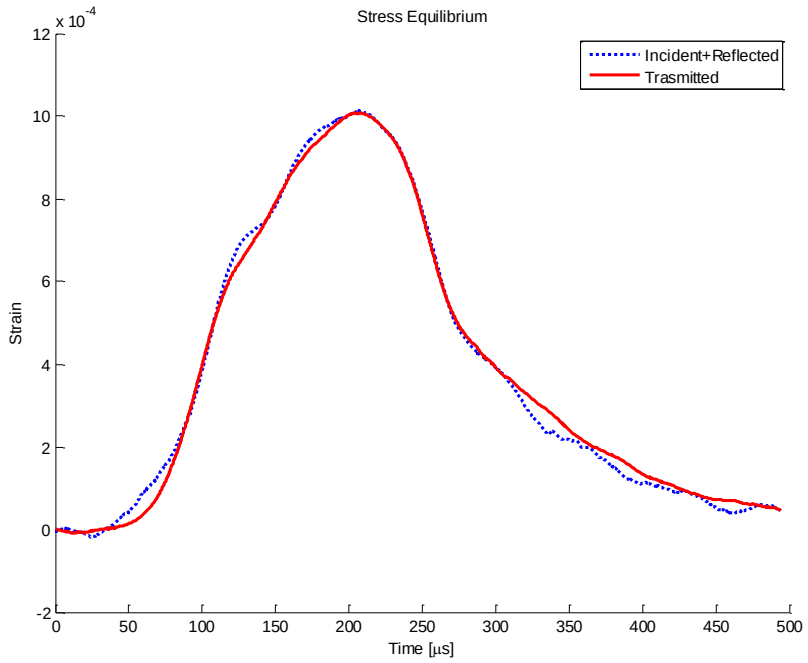

Figure A-105 Experiment 1 Stress Equilibrium

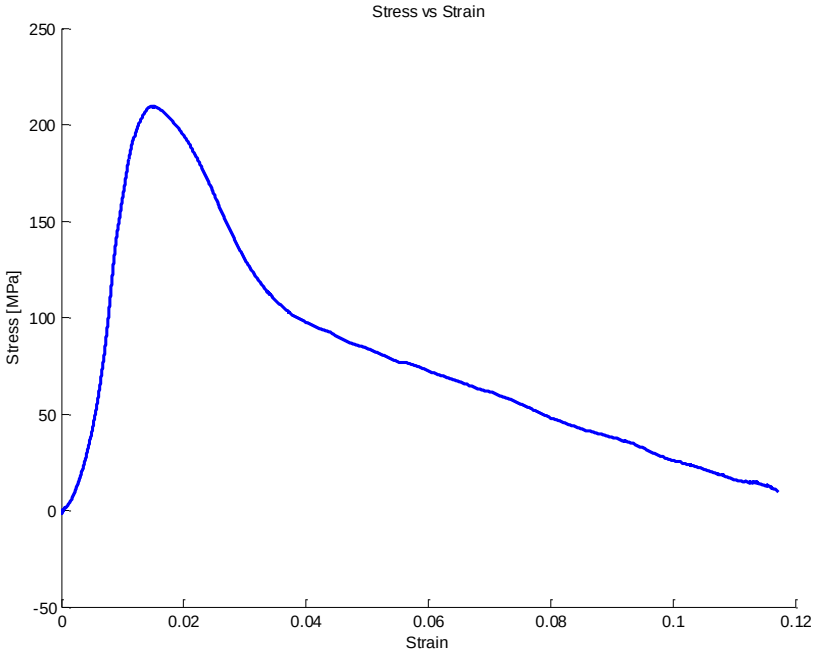

Figure A-106 Experiment 1 Stress Strain Curve

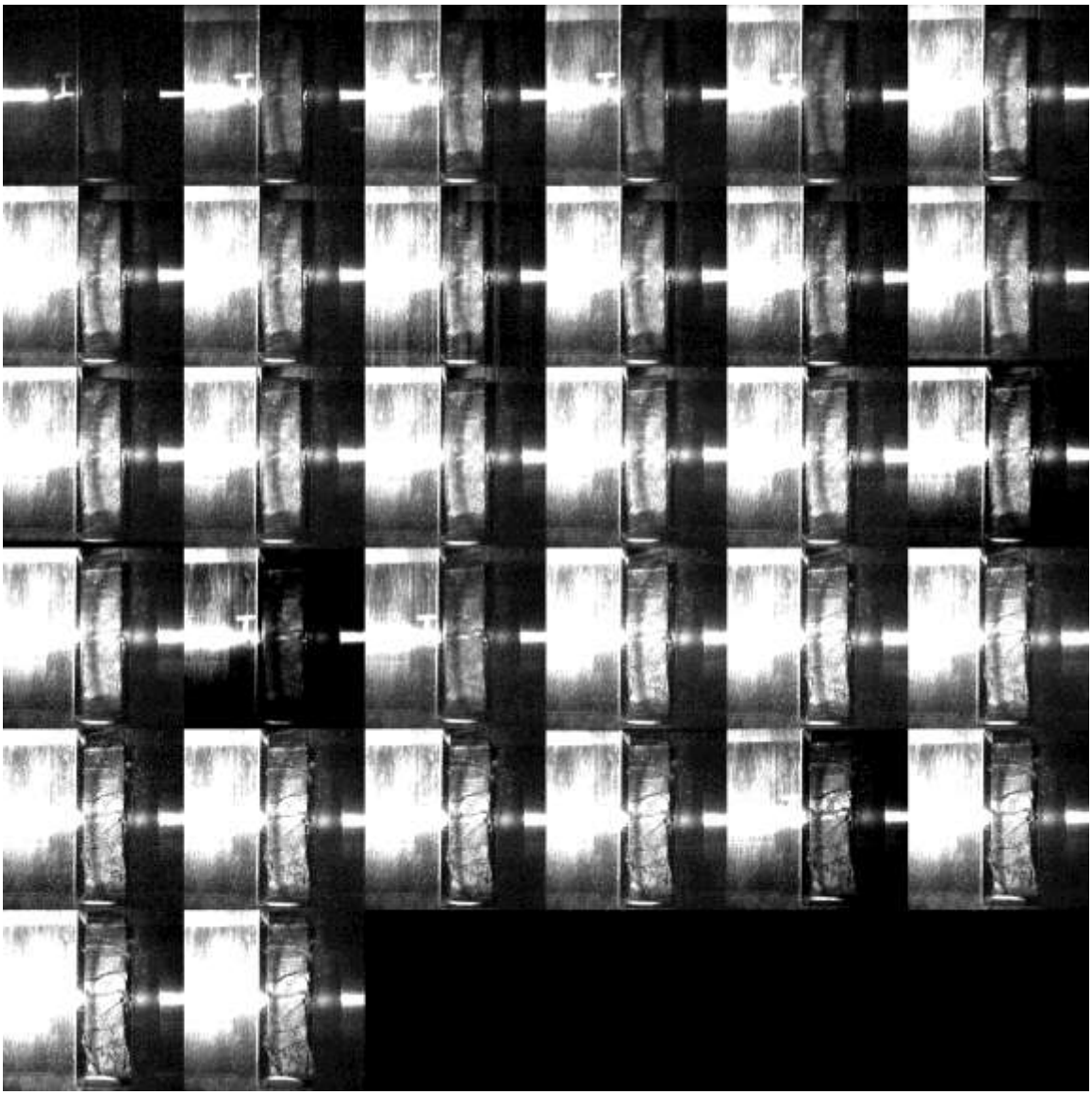

Figure A-107 Experiment 1 High Speed Images at Frame Rate 62257 fps

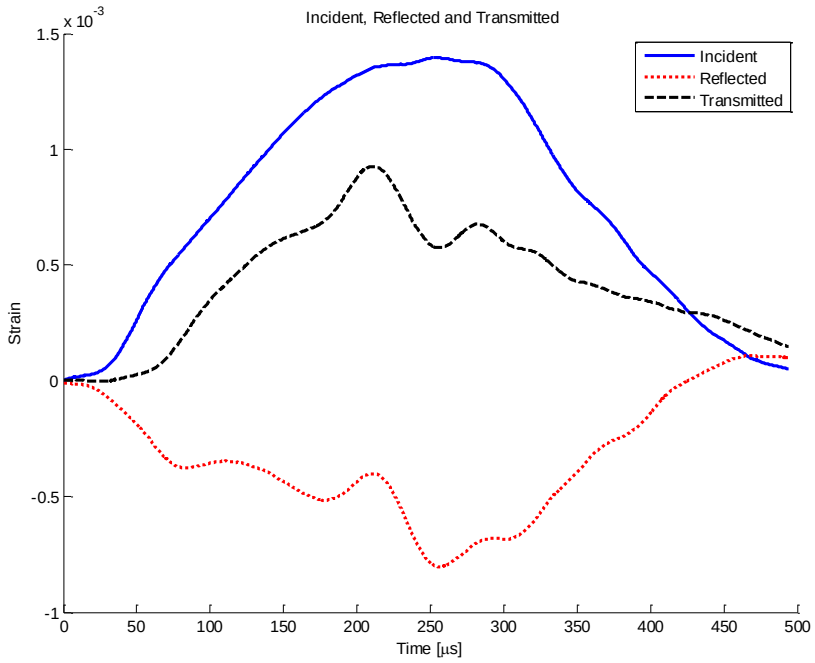

Figure A-108 Experiment 2 Incident Reflected and Transmitted Pulse

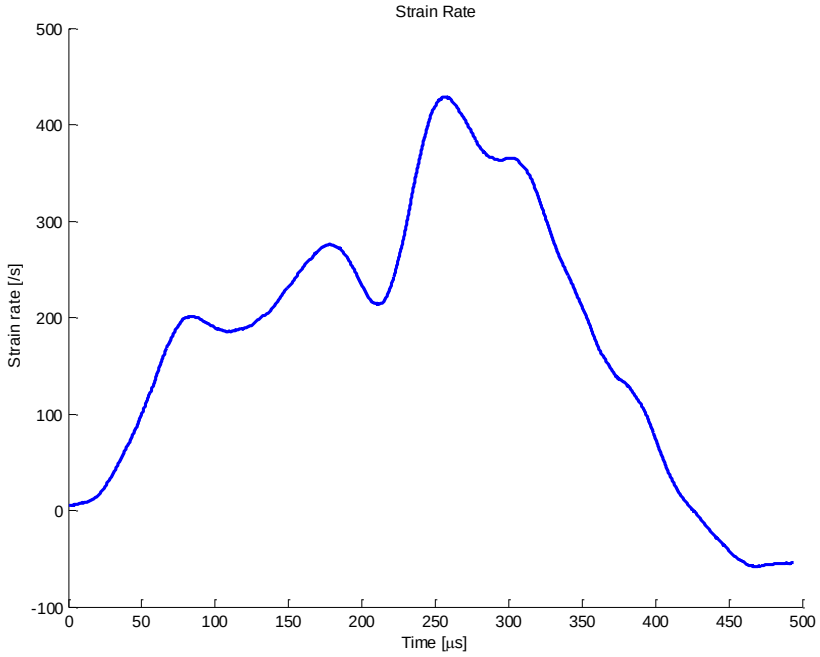

Figure A-109 Experiment 2 Strain Rate History

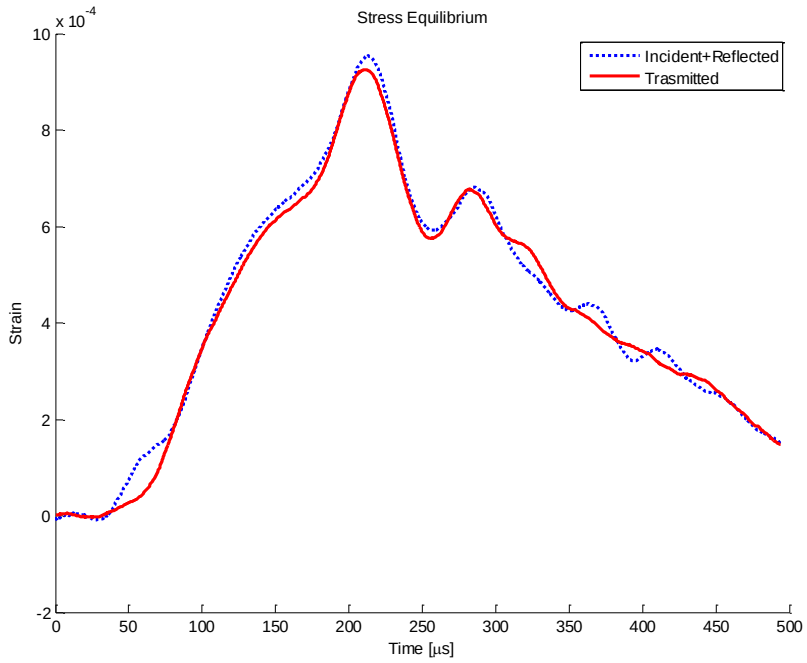

Figure A-110 Experiment 2 Stress Equilibrium

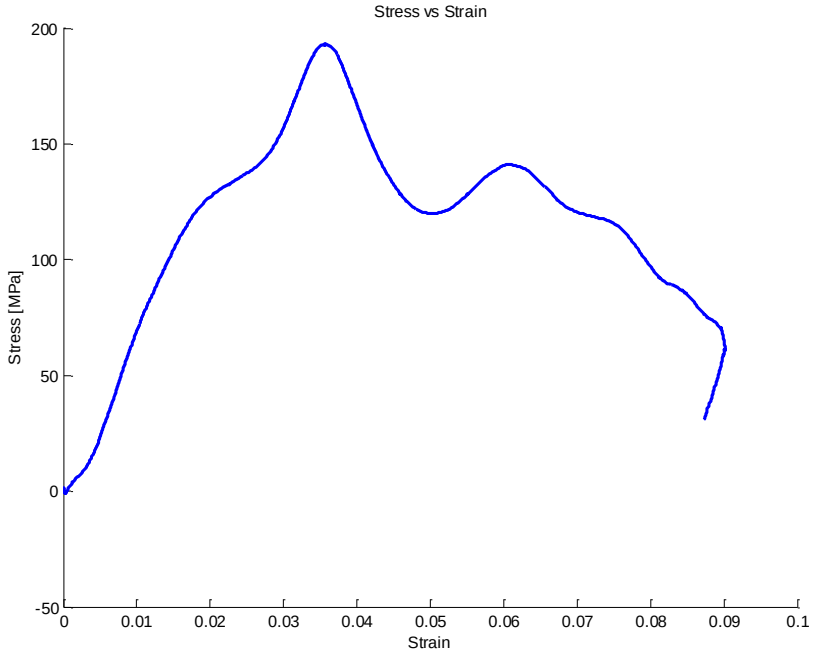

Figure A-111 Experiment 2 Stress Strain Curve

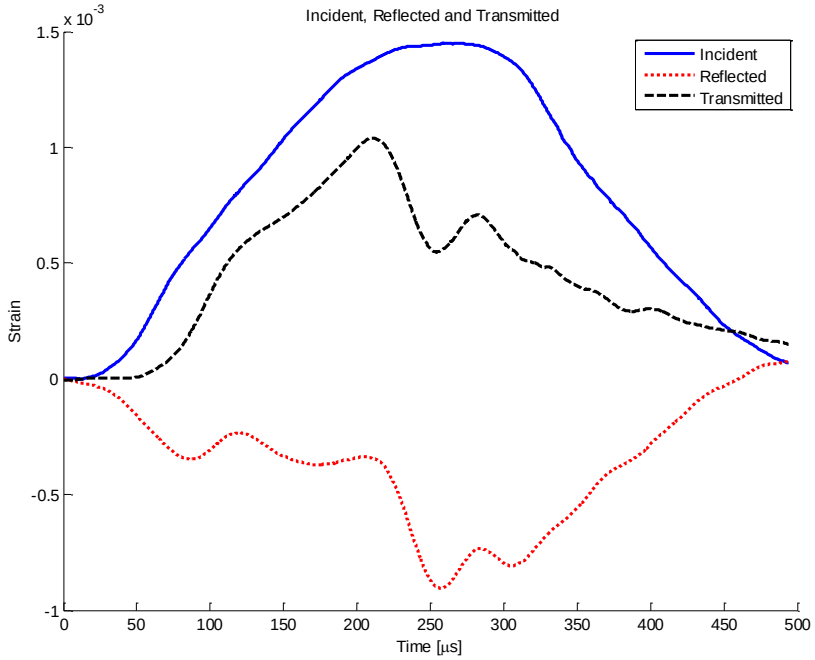

Figure A-112 Experiment 3 Incident Reflected and Transmitted Pulse

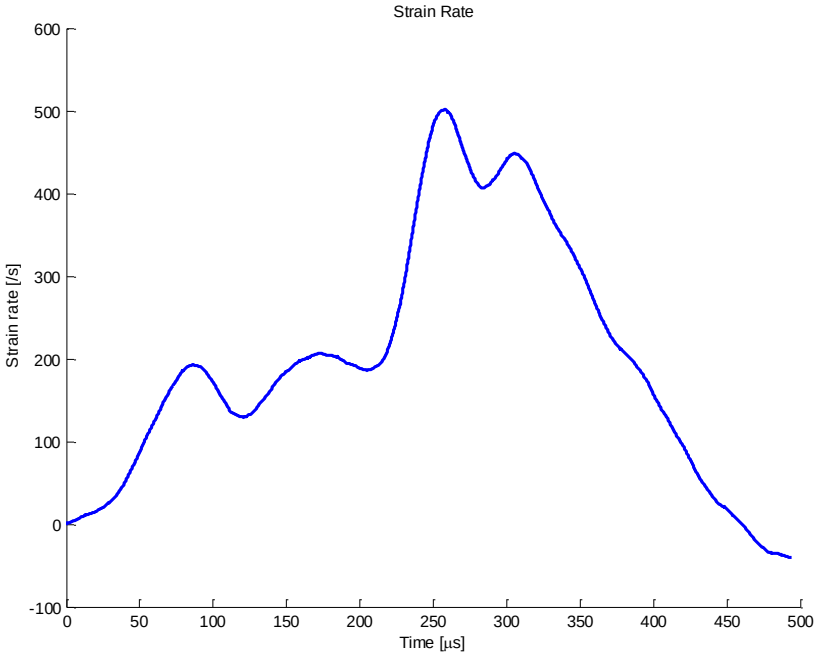

Figure A-113 Experiment 3 Strain Rate History

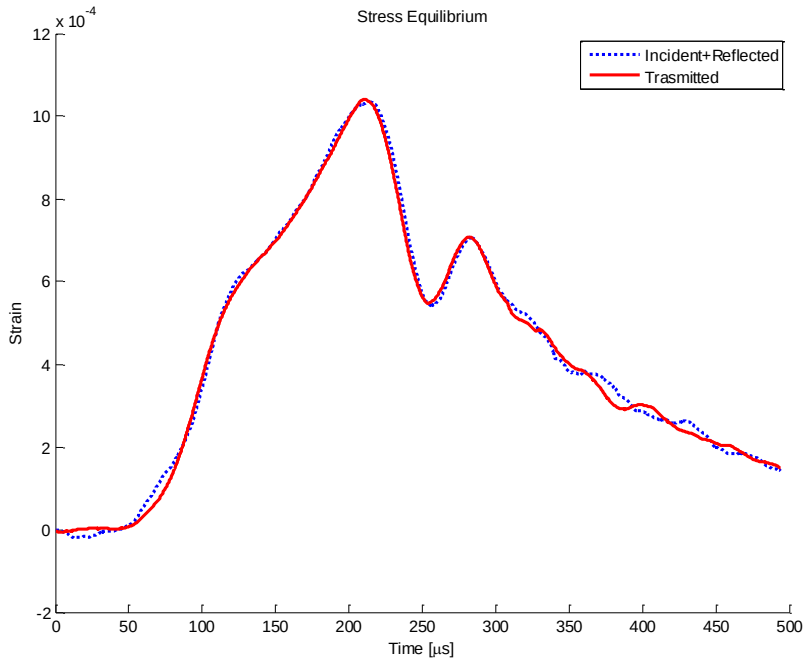

Figure A-114 Experiment 3 Stress Equilibrium

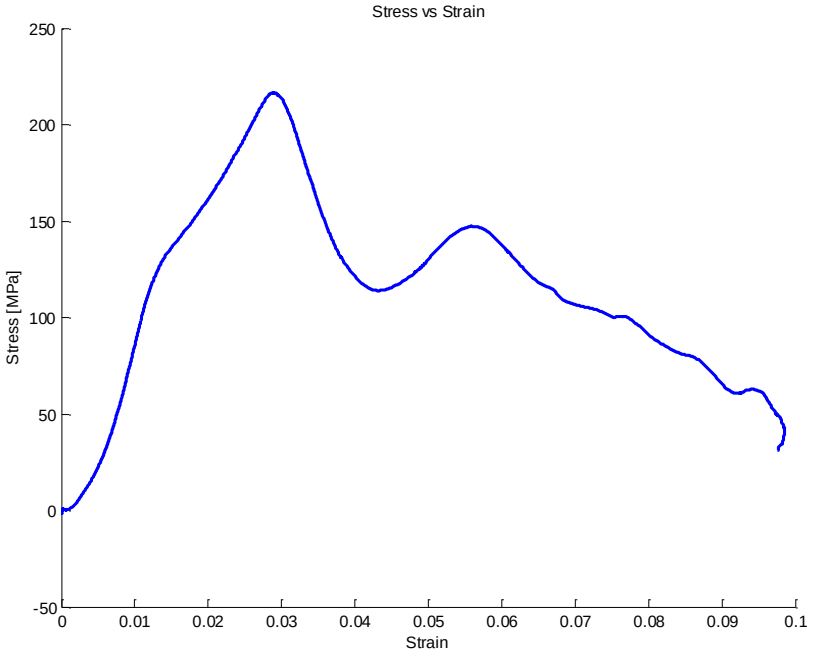

Figure A-115 Experiment 3 Stress Strain Curve

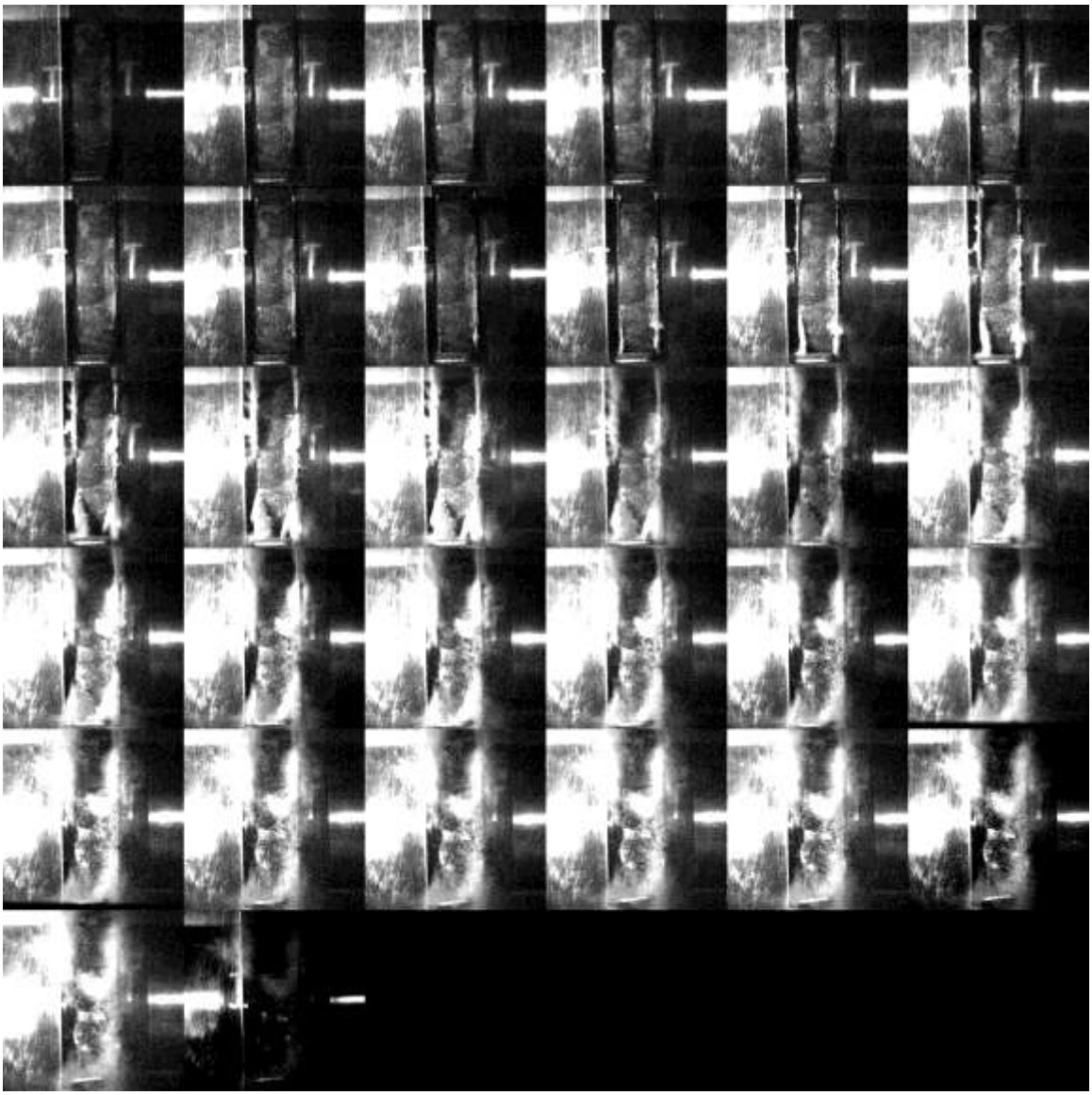

Figure A-116 Experiment 3 High Speed Images at Frame Rate 64516 fps

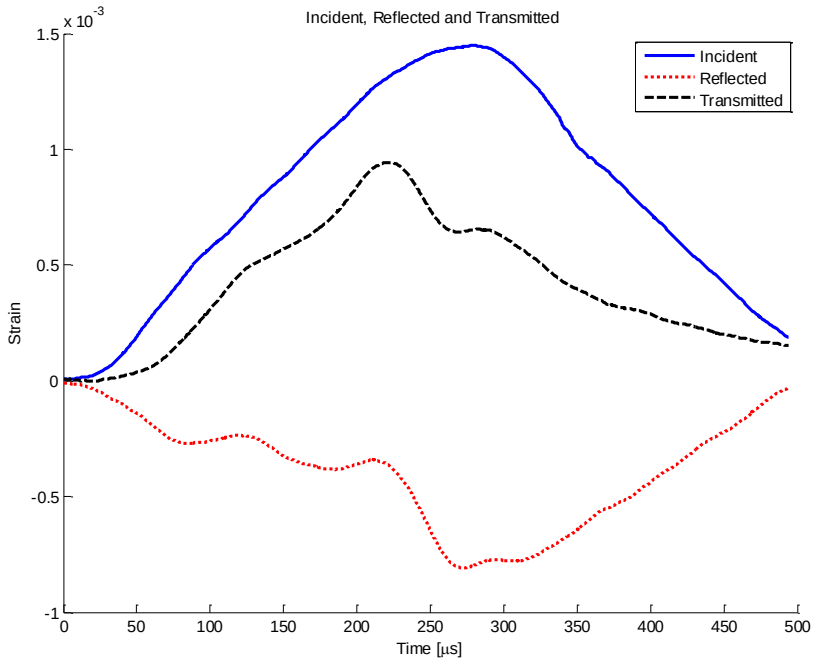

Figure A-117 Experiment 4 Incident Relfected and Transmitted Pulse

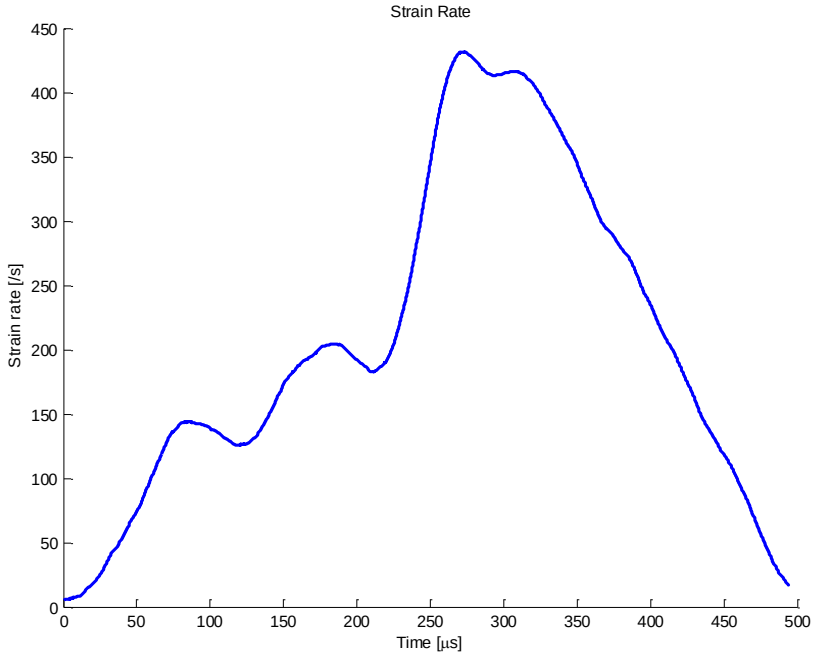

Figure A-118 Experiment 4 Strain Rate History

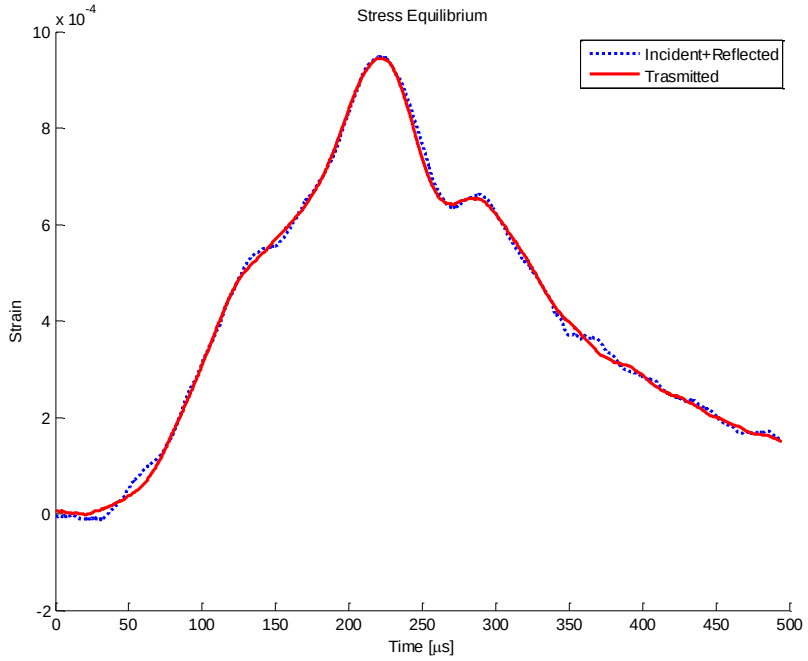

Figure A-119 Experiment 4 Stress Equilibrium

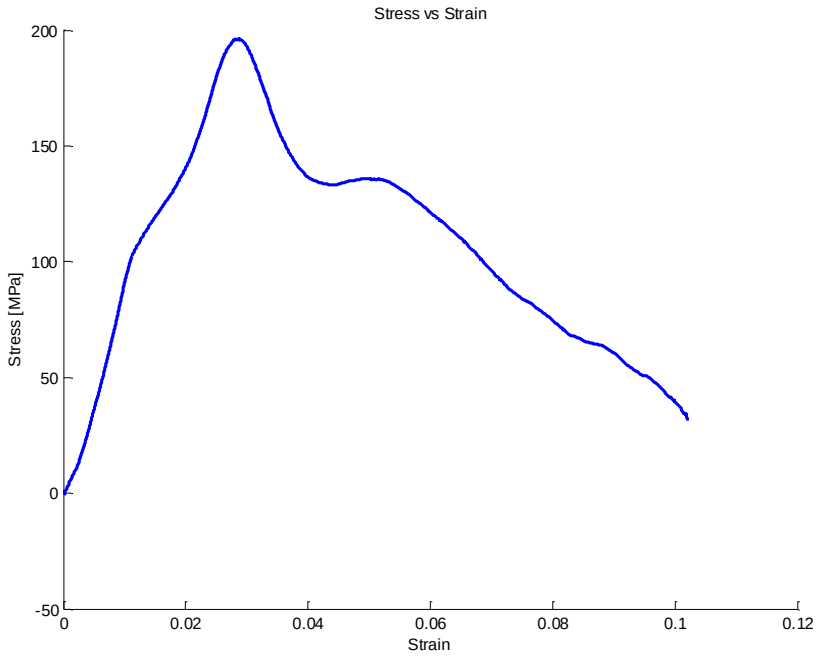

Figure A-120 Experiment 4 Stress Strain Curve

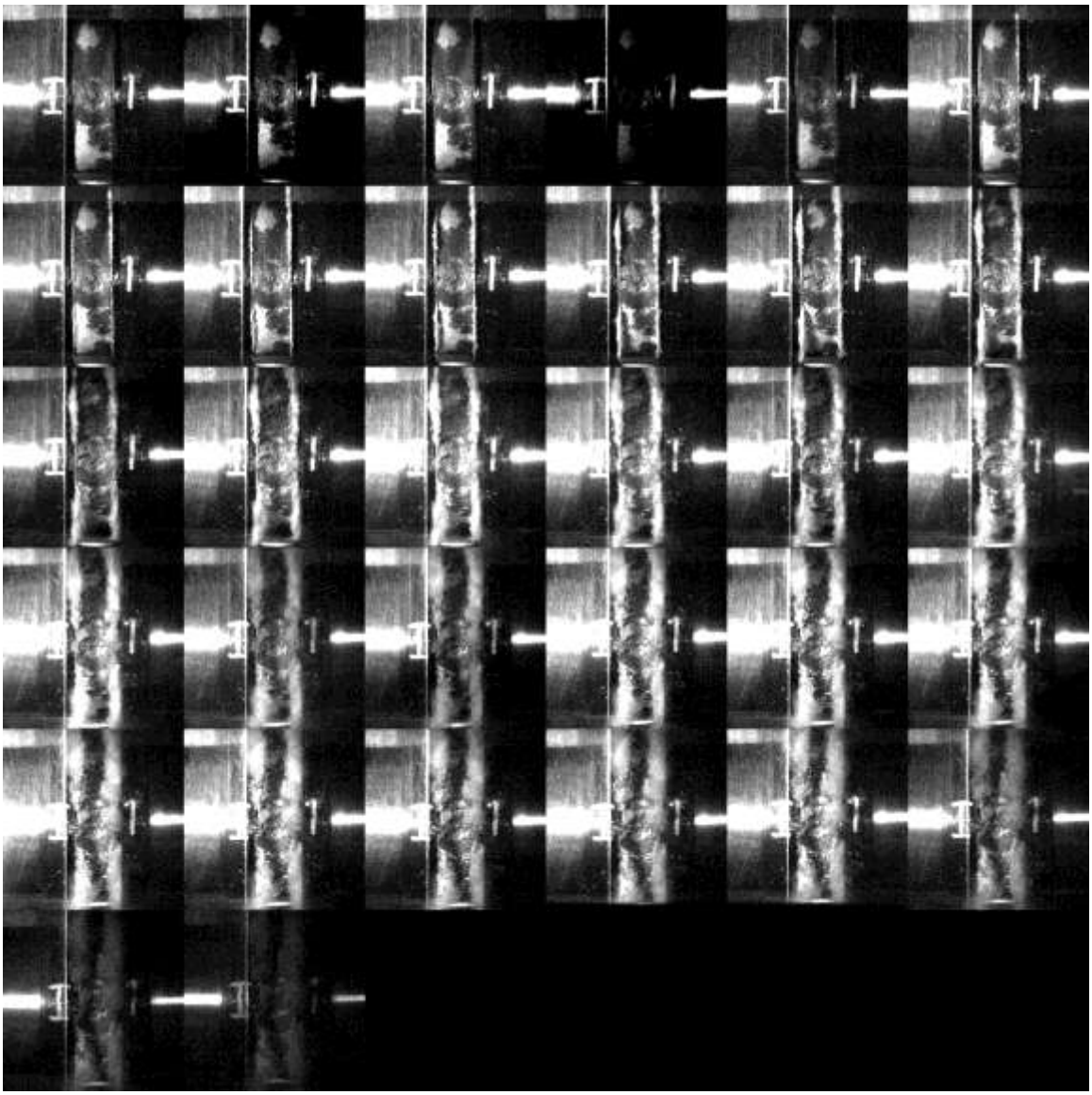

Figure A-121 Experiment 4 High Speed Images at Frame Rate 64646 fps

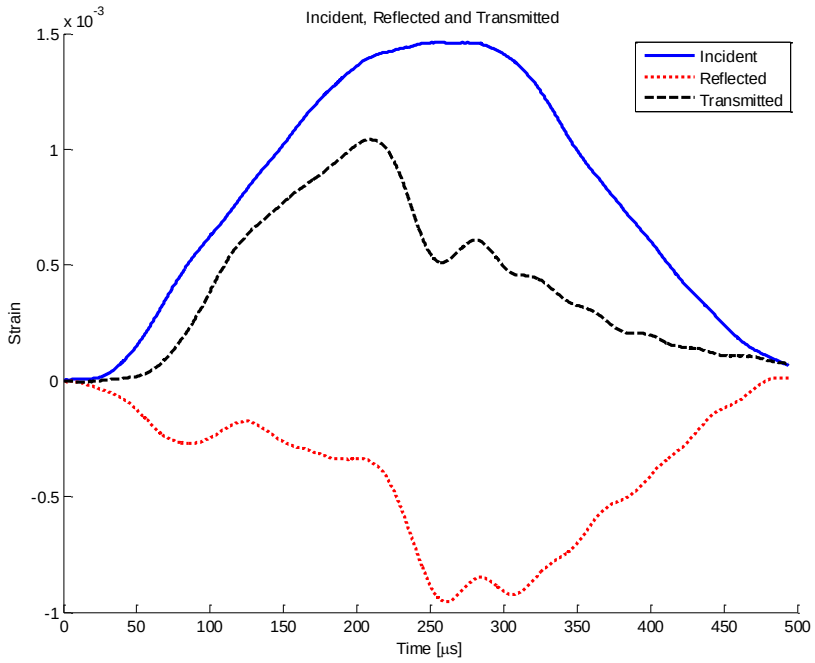

Figure A-122 Experiment 5 Incident Reflected and Transmitted Pulse

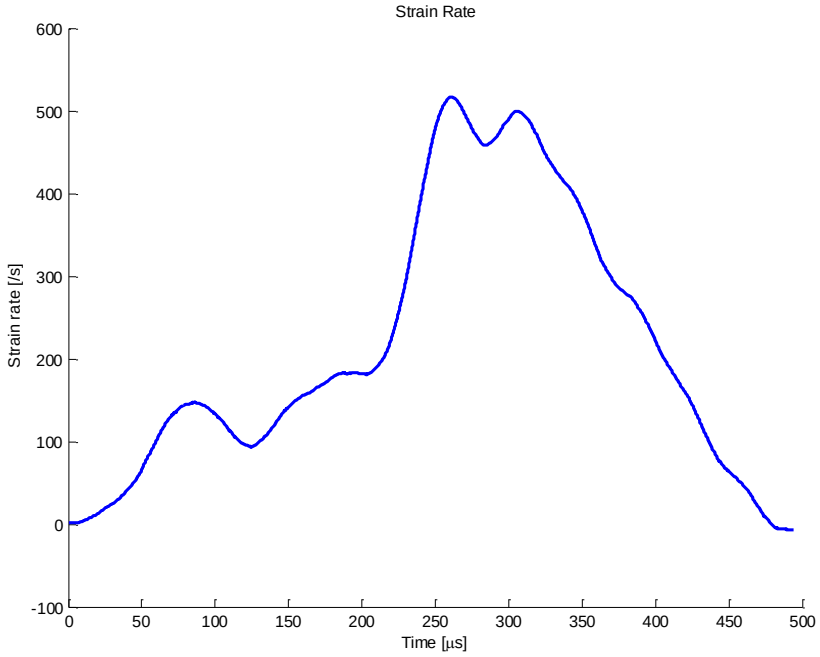

Figure A-123 Experiment 5 Strain Rate History

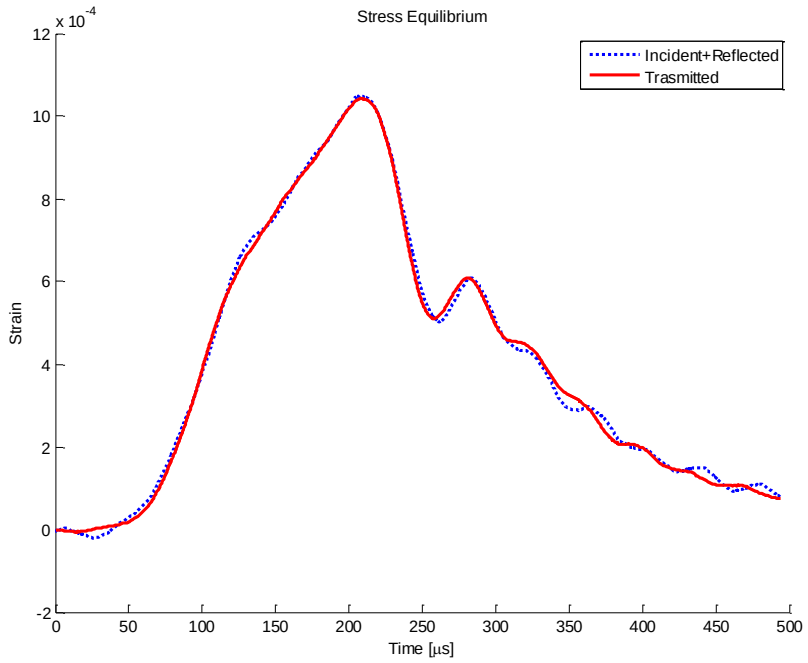

Figure A-124 Experiment 5 Stress Equilibrium

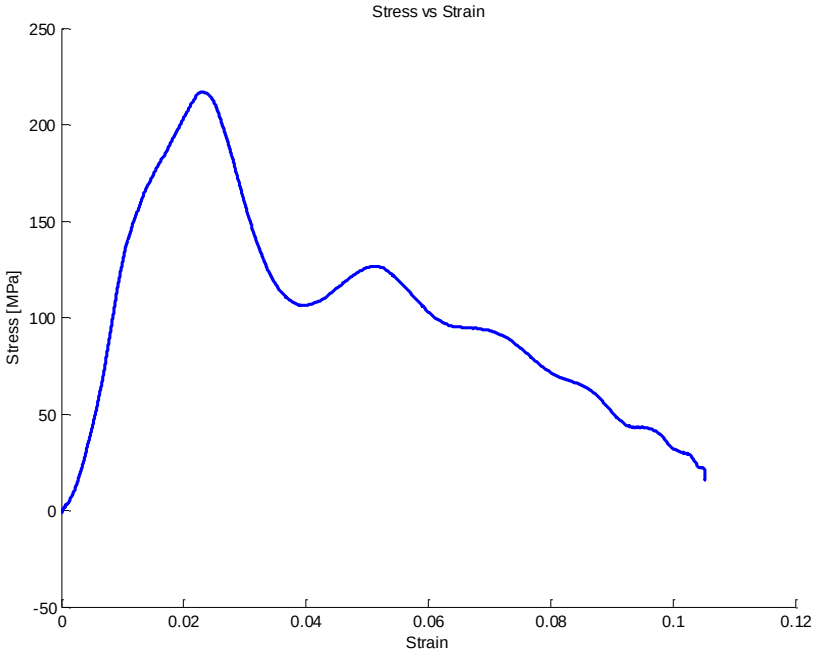

Figure A-125 Experiment 5 Stress Strain Curve

A4: Dynamic Uniaxial Compressive Experiments on Big New Cor Tuf

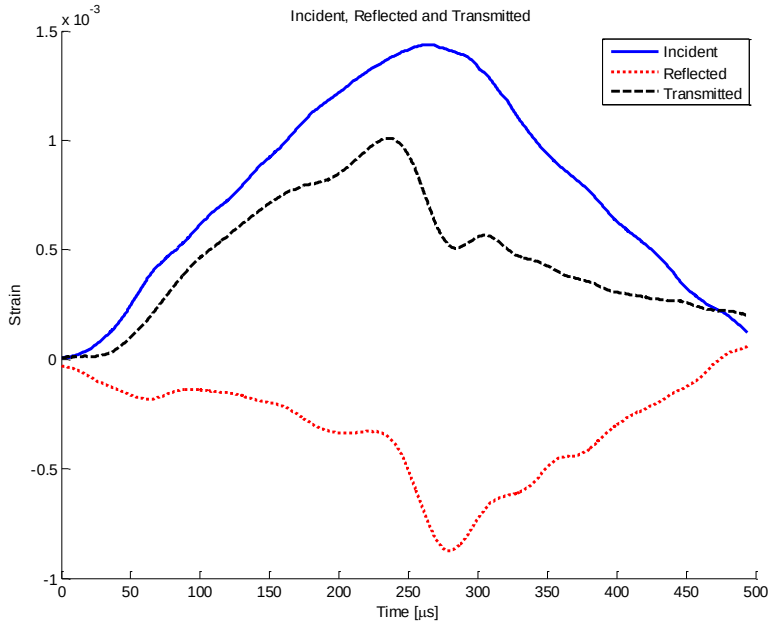

Figure A-126 Experiment 1 Incident Reflected and Transmitted Pulse

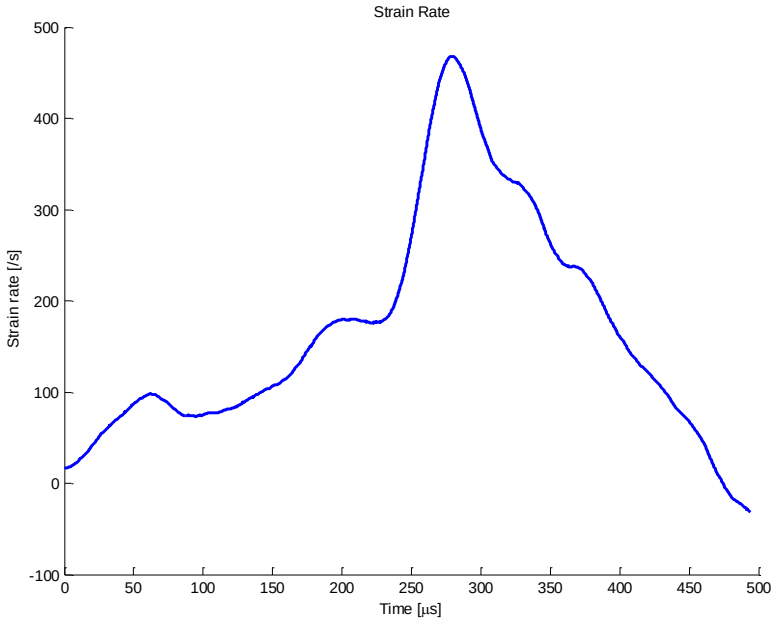

Figure A-127 Experiment 1 Strain Rate History

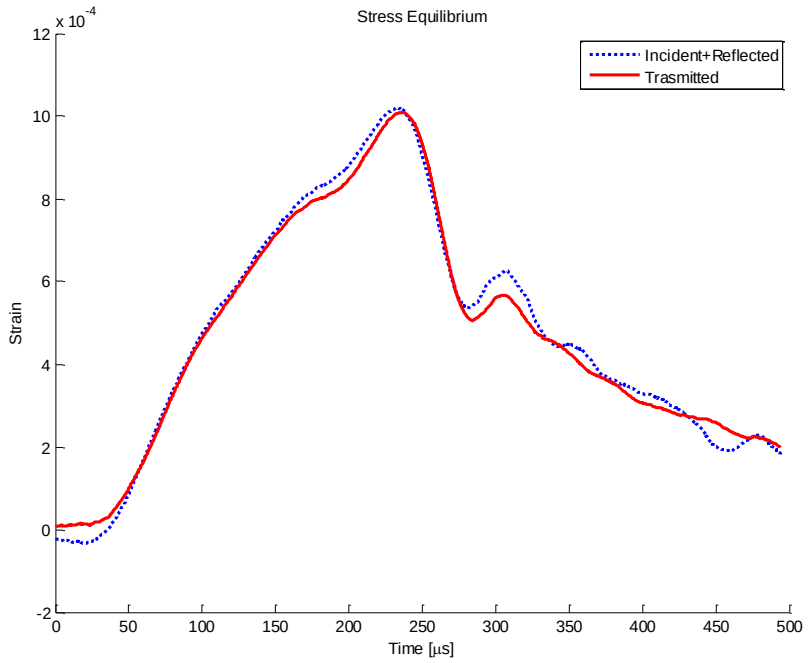

Figure A-128 Experiment 1 Stress Equilibrium

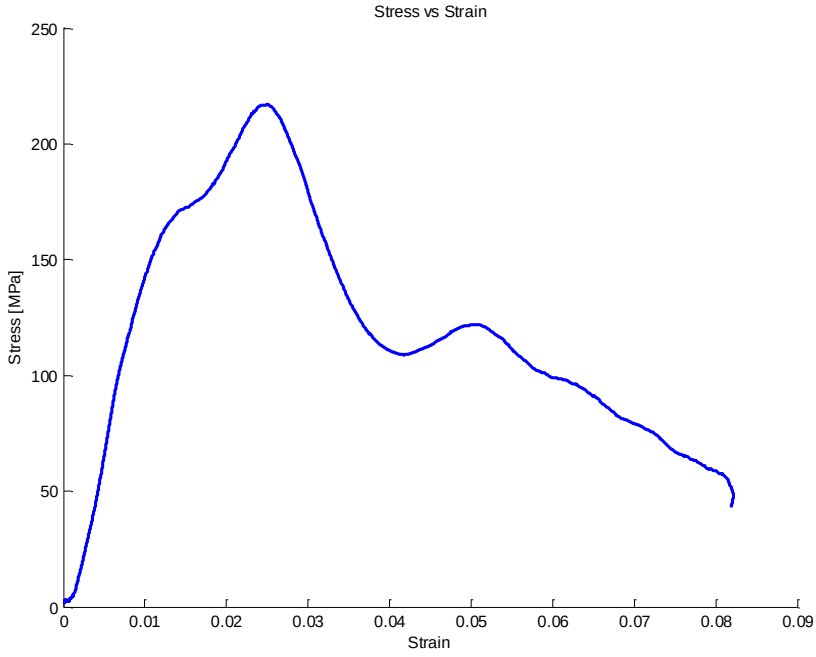

Figure A-129 Experiment 1 Stress Strain Curve

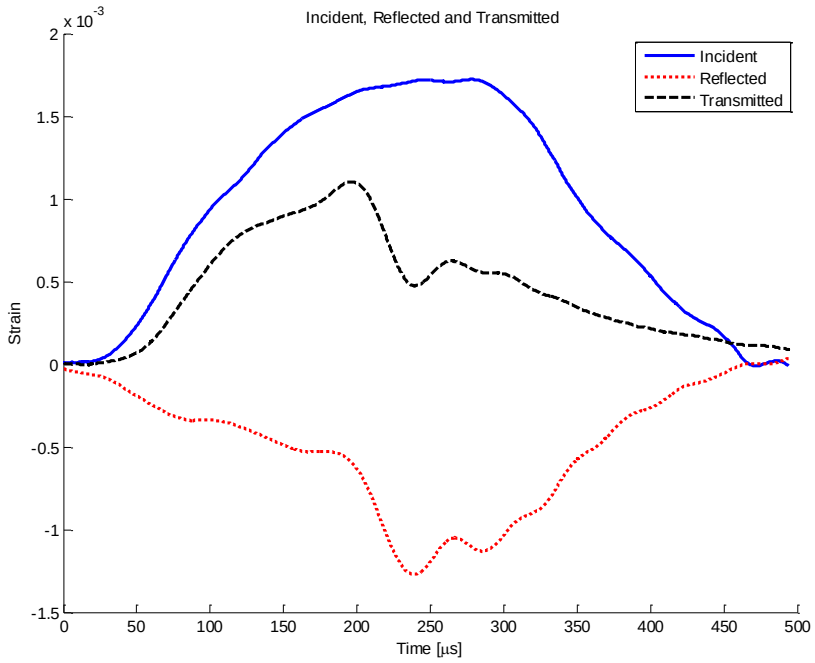

Figure A-130 Experiment 2 Incident Reflected and Transmitted Pulse

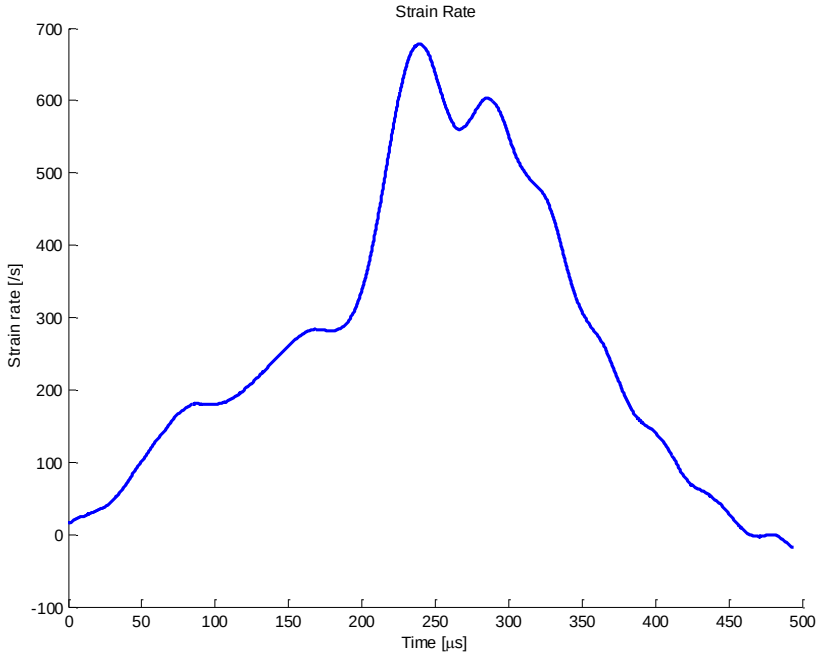

Figure A-131 Experiment 2 Strain Rate History

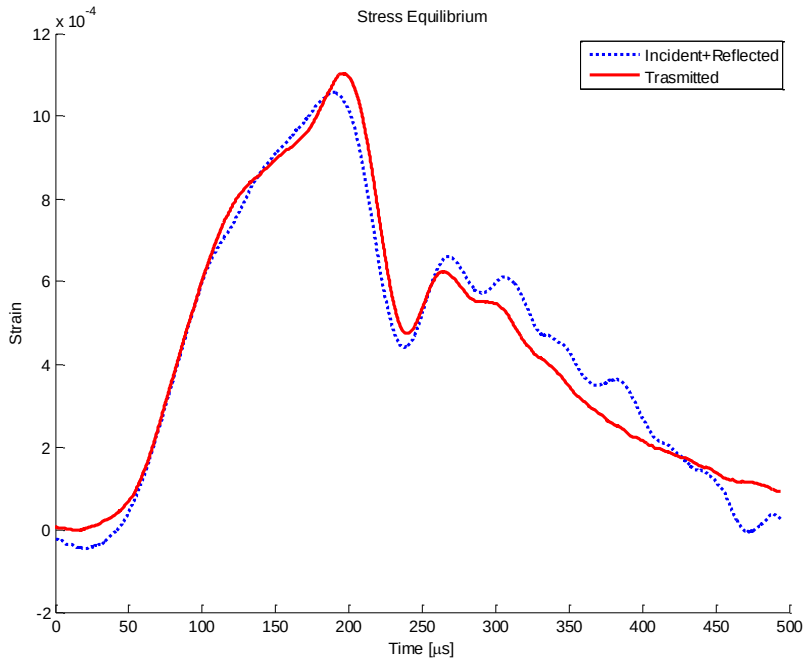

Figure A-132 Experiment 2 Stress Equilibrium

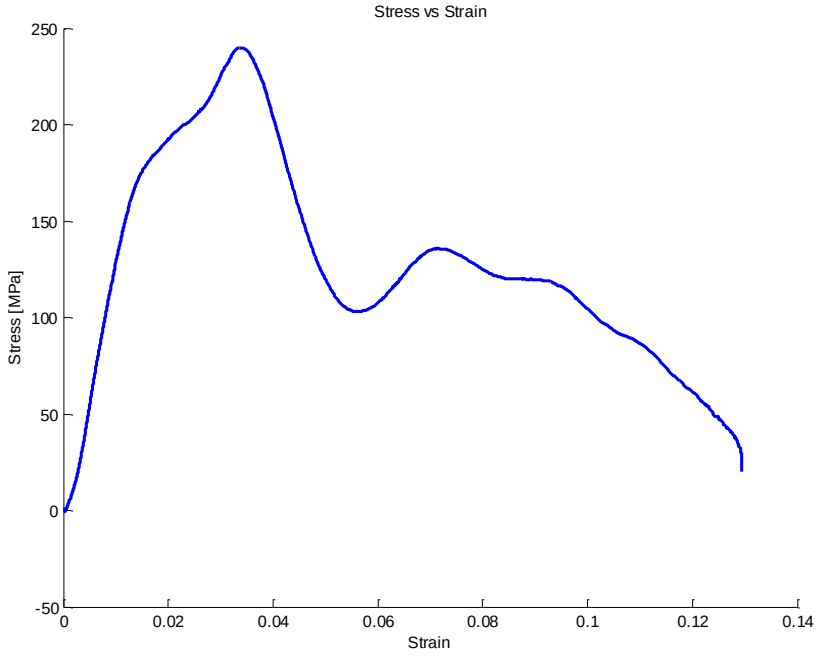

Figure A-133 Experiment 2 Stress Strain Curve

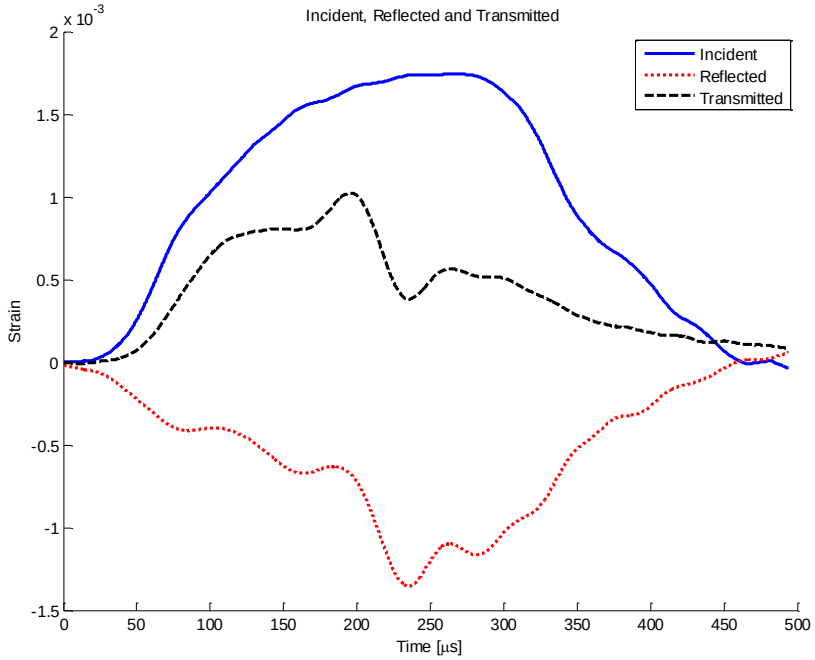

Figure A-134 Experiment 3 Incident Reflected and Transmitted Pulse

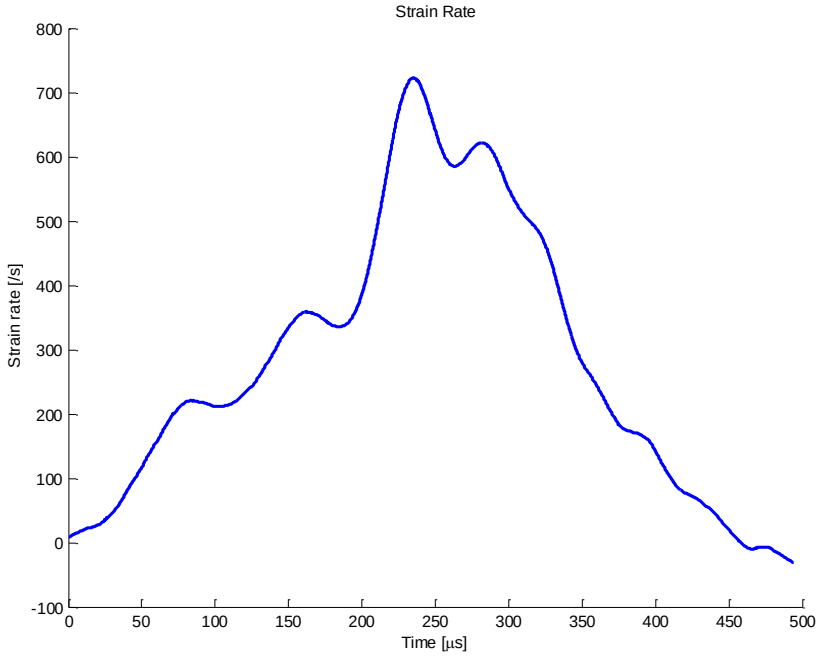

Figure A-135 Experiment 3 Strain Rate History

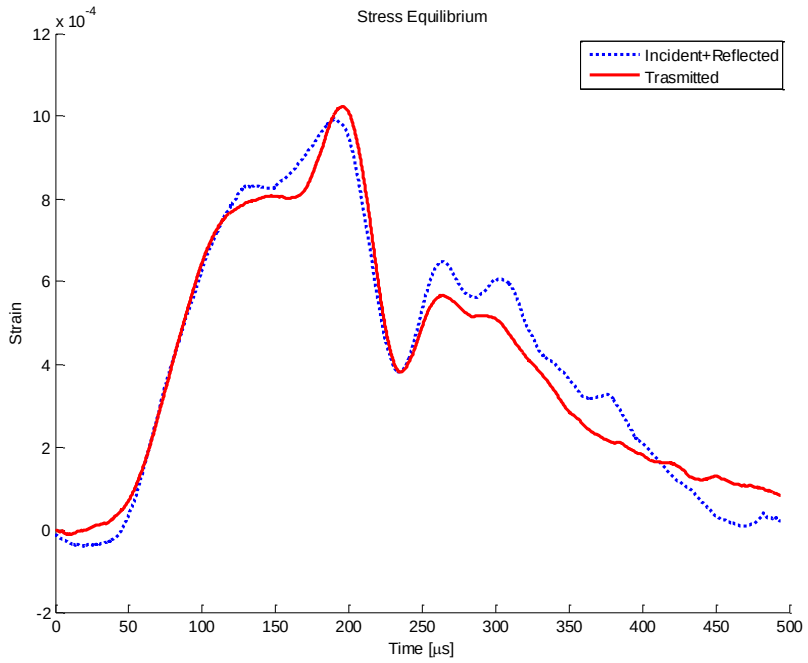

Figure A-136 Experiment 3 Stress Equilibrium

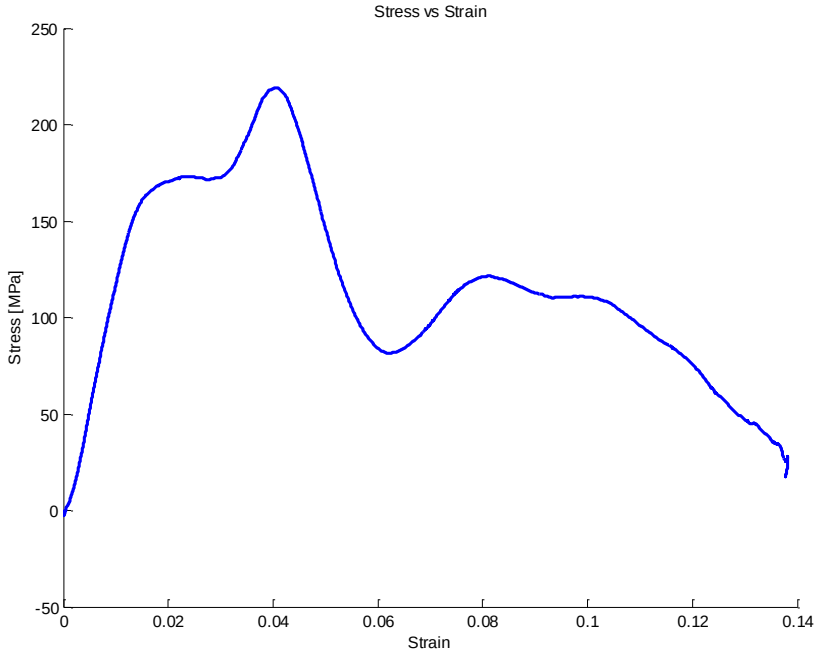

Figure A-137 Experiment 3 Stress Strain Curve

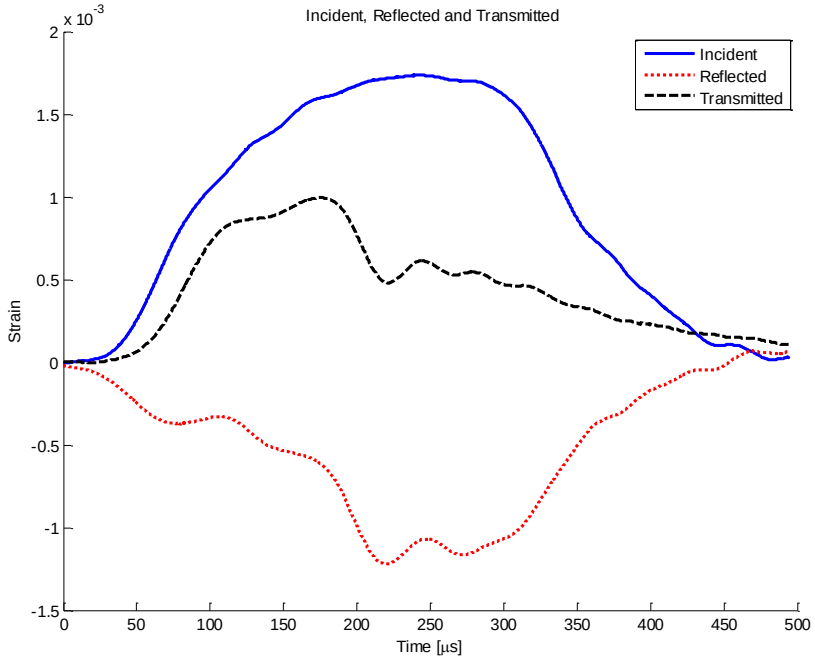

Figure A-138 Experiment 4 Incident Reflected and Transmitted Pulse

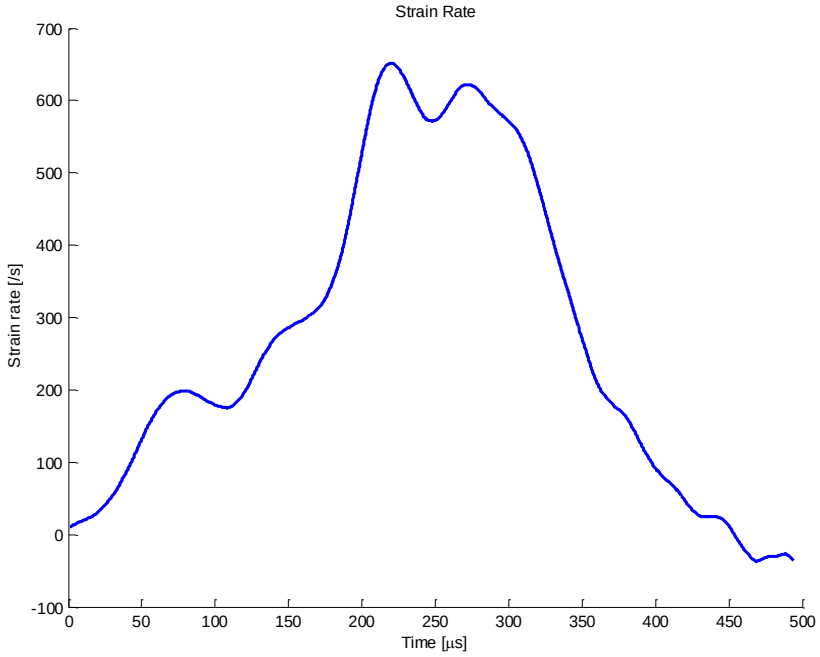

Figure A-139 Experiment 4 Strain Rate History

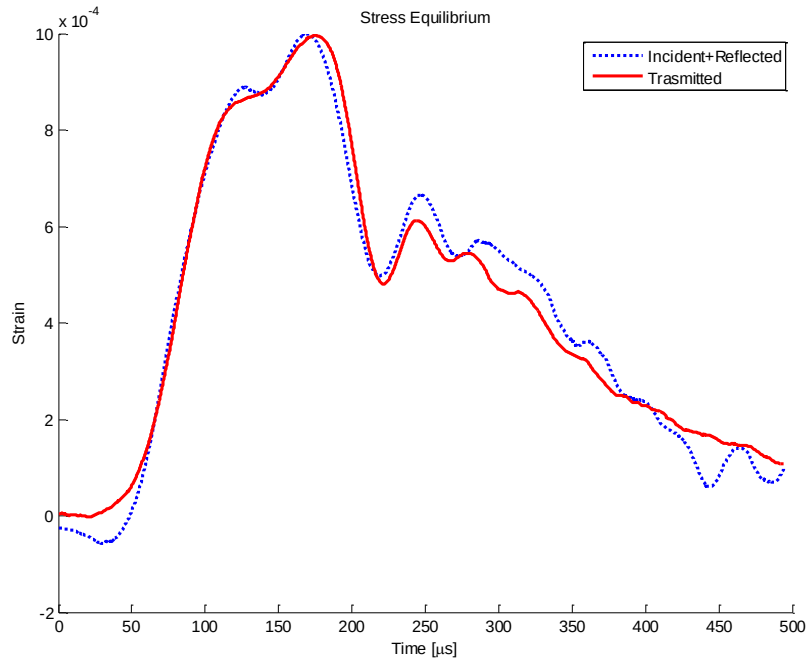

Figure A-140 Experiment 4 Stress Equilibrium

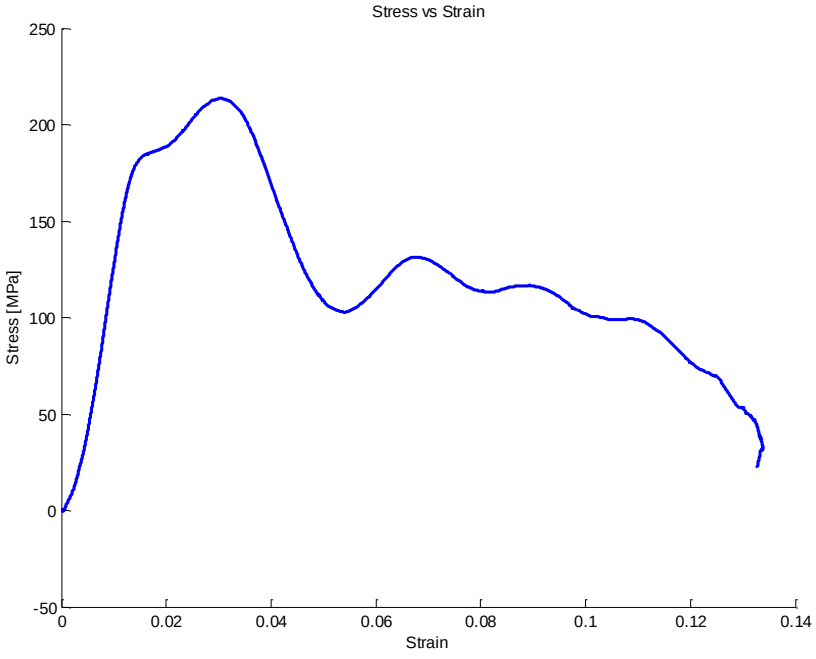

Figure A-141 Experiment 4 Stress Strain Curve

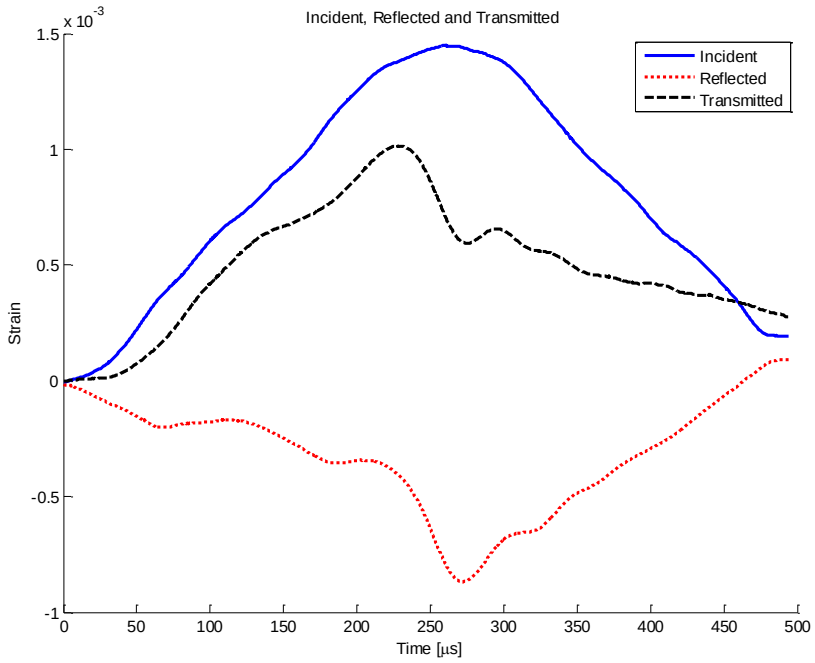

Figure A-142 Experiment 5 Incident Reflected and Transmitted Pulse

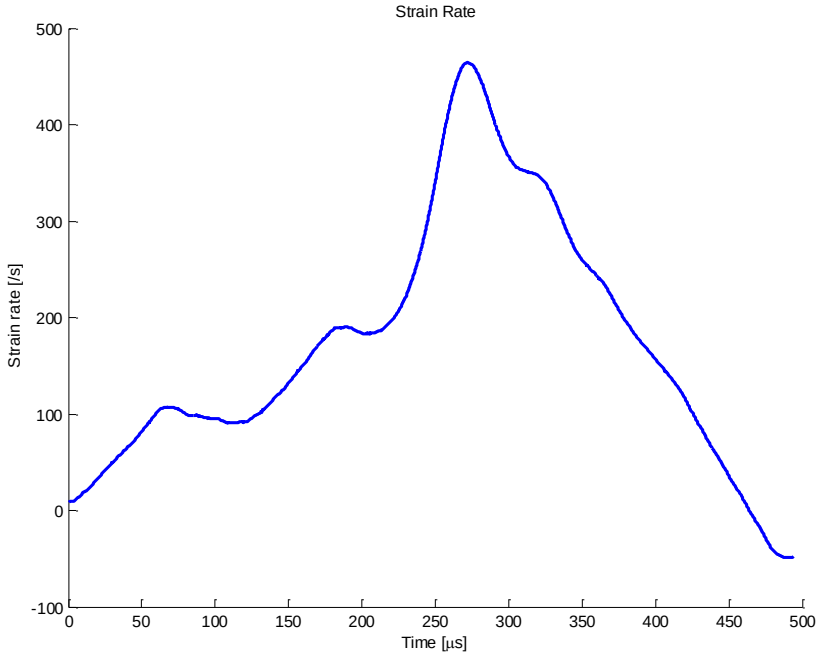

Figure A-143 Experiment 5 Strain Rate History

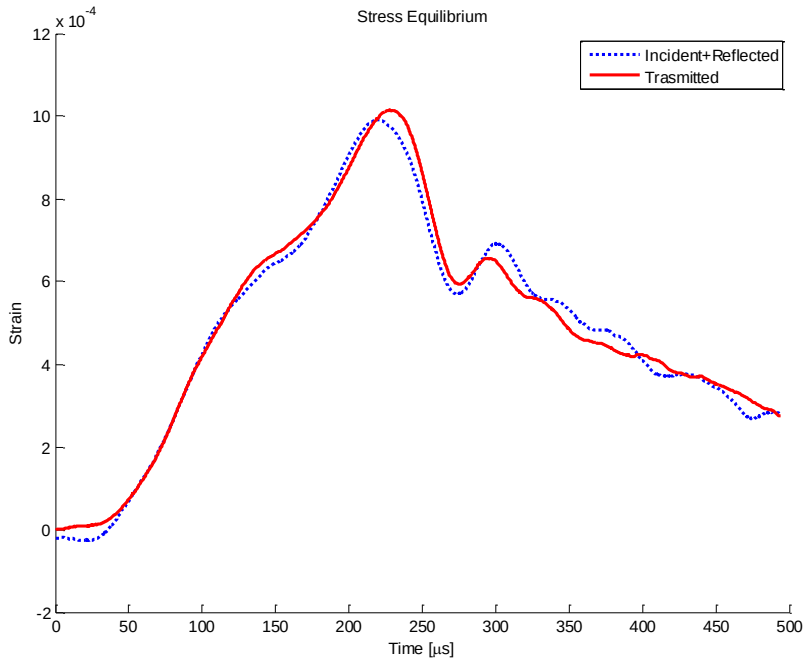

Figure A-144 Experiment 5 Stress Equilibrium

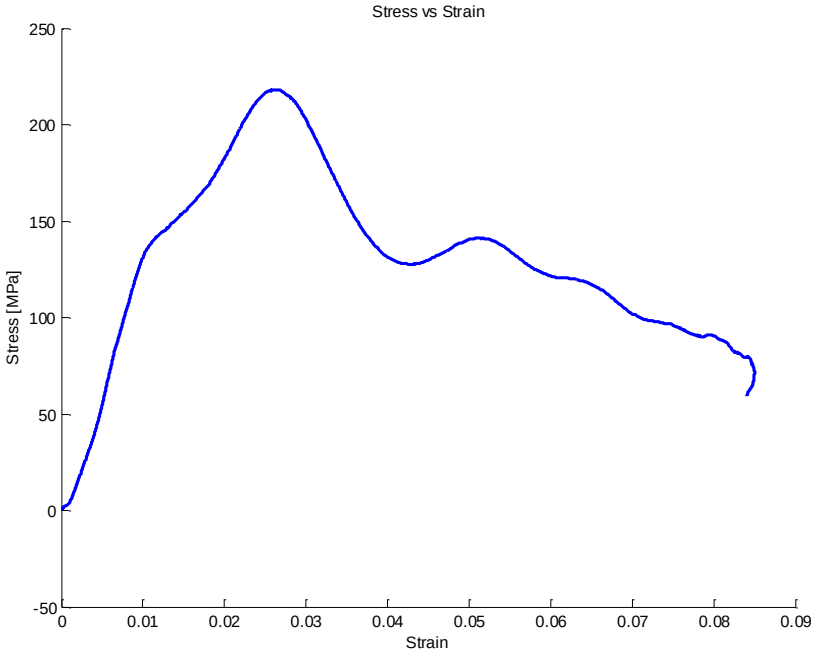

Figure A-145 Experiment 5 Stress Strain Curve

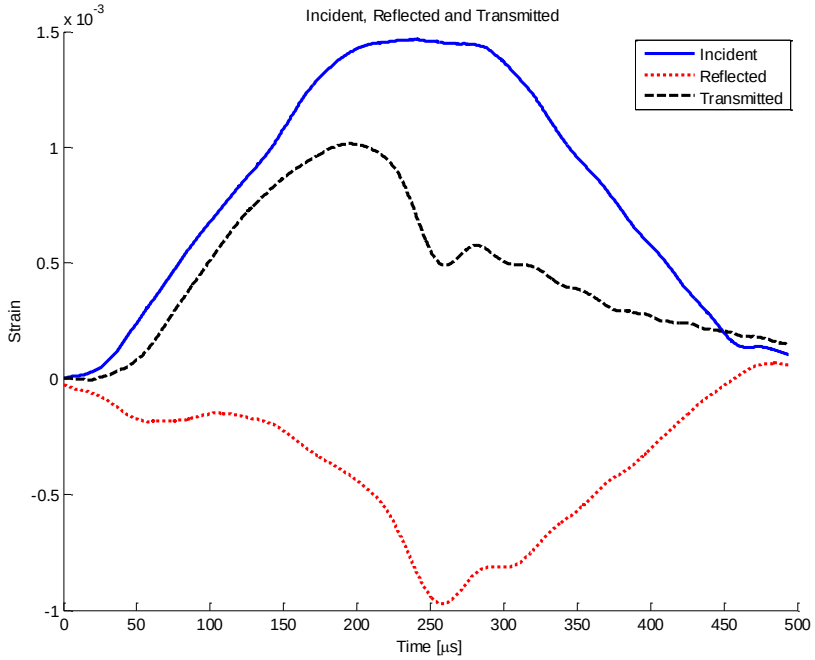

Figure A-146 Experiment 6 Incident Reflected and Transmitted Pulse

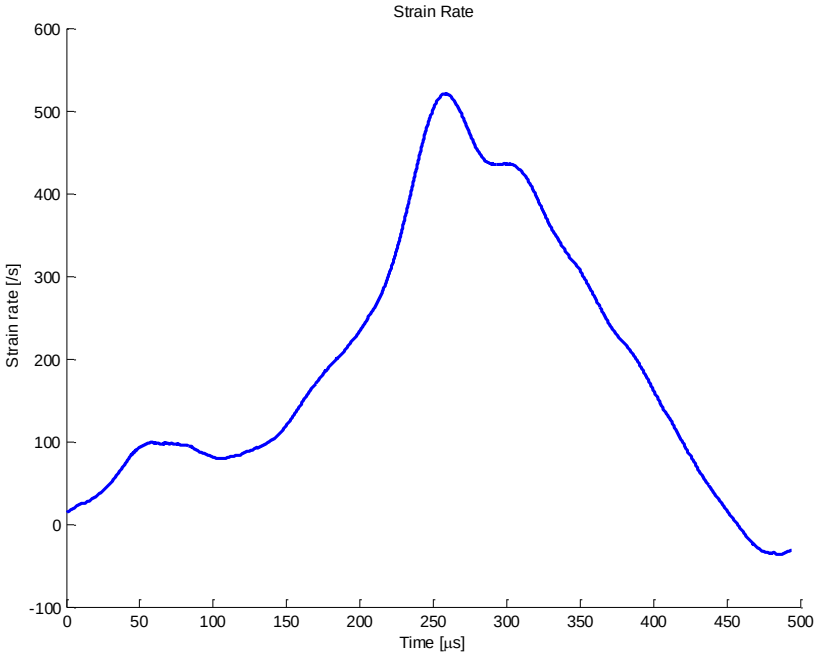

Figure A-147 Experiment 6 Strain Rate History

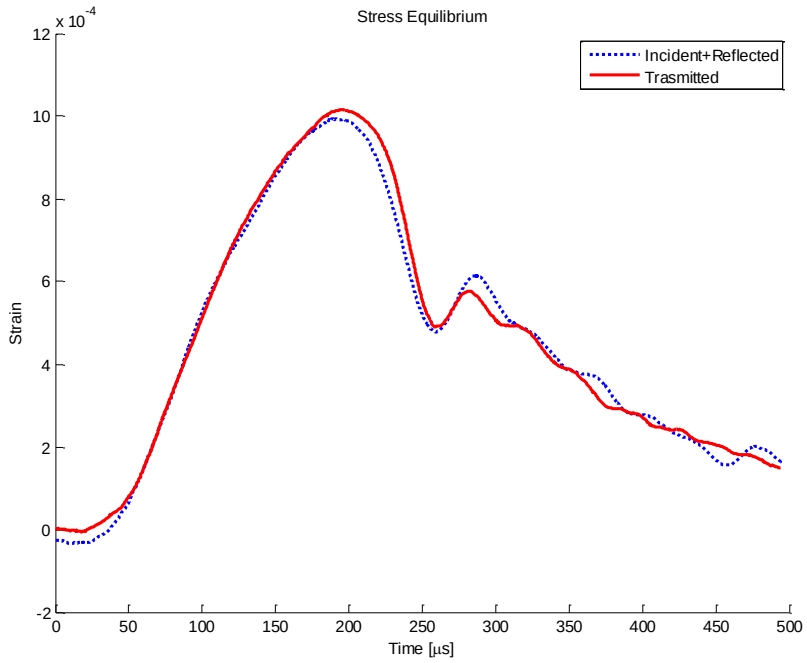

Figure A-148 Experiment 6 Stress Equilibrium

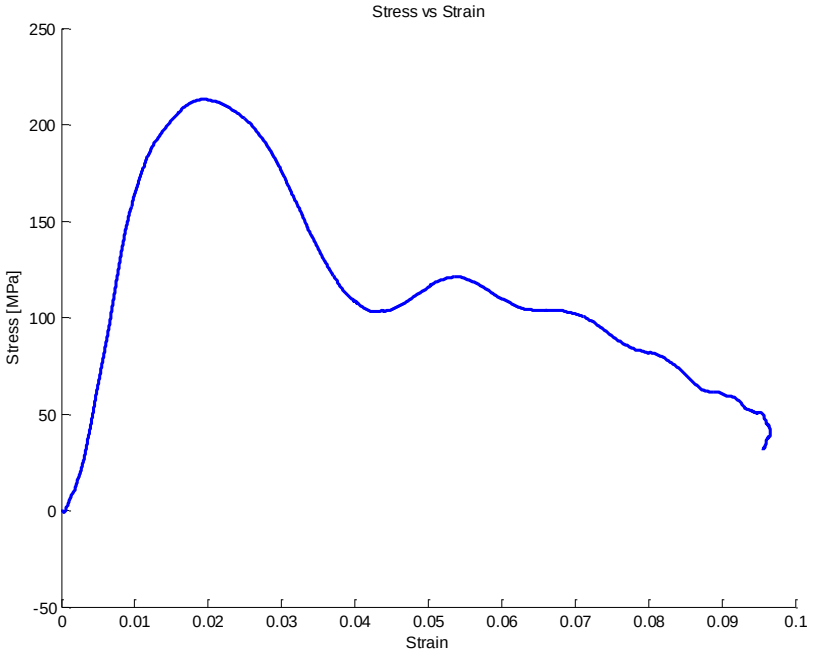

Figure A-149 Experiment 6 Stress Strain Curve

VITA

VITA

Boon Him Lim was born in Penang, Malaysia at 1989. Boon Him earned his Bachelor's Degree in Aeronautics and Astronautics Engineering with distinction from Purdue University at December 2011. He also earned numerous honors including Dean's List and semester honors from 2009-2011. In Spring 2011, Boon Him decided to pursue his Master of Science in Aeronautics and Astronautics Engineering under guidance of Professor Chen. Boon Him plan to continue to work on his PhD at Purdue University under guidance of Professor Chen.